GROWTH MECHANISMS, AND MECHANICAL AND THERMAL PROPERTIES OF JUNCTIONS IN 3D CARBON NANOTUBE-GRAPHENE NANO-ARCHITECTURES

Jianbing Niu, B.S.

Dissertation Prepared for the Degree of

DOCTOR OF PHILOSOPHY

UNIVERSITY OF NORTH TEXAS

December 2014

APPROVED:

Zhenhai Xia, Major Professor
Wonbong Choi, Committee Member
Jincheng Du, Committee Member
Sundeep Mukherjee, Committee Member
Zhiqiang Wang, Committee Member
Nigel Shepherd, Chair of the Department of Materials Science and Engineering
Costas Tsatsoulis, Dean of the College of Engineering
Mark Wardell, Dean of the Toulouse Graduate School

Niu, Jianbing. Growth mechanisms, and mechanical and thermal properties of junctions in 3D carbon nanotube-graphene nano-architectures. Doctor of Philosophy (Materials Science and Engineering), December 2014, 143 pp., 61 figures, chapter references.

Junctions are the key component for 3D carbon nanotube (CNT)-graphene seamless hybrid nanostructures. Growth mechanism of junctions of vertical CNTs growing from graphene in the presence of iron catalysts was simulated via quantum mechanical molecular dynamics (QM/MD) methods. CNTs growth from graphene with iron catalysts is based on a ‘‘base-growth’’ mechanism, and the junctions were the mixture of C-C and Fe-C covalent bonds. Pure C-C bonded junctions could be obtained by moving the catalyst during CNT growth or etching and annealing after growth. The growth process of 3D CNT-graphene junctions on copper templates with nanoholes was simulated with molecular dynamic (MD) simulation. There are two mechanisms of junction formation: (i) CNT growth over the holes that are smaller than 3 nm, and (ii) CNT growth inside the holes that are larger than 3 nm. The growth process of multi-layer filleted CNT-graphene junctions on the Al_2O_3 template was also simulated with MD simulation. A simple analytical model is developed to explain that the fillet takes the particular angle (135°). MD calculations show that 135° filleted junction has the largest fracture strength and thermal conductivity at room temperature compared to junctions with 90°,120°, 150°, and 180° fillets.

The tensile strengths of the as-grown C–C junctions, as well as the junctions embedded with metal nanoparticles (catalysts), were determined by a QM/MD method. Metal catalysts remaining in the junctions significantly reduce the fracture strength and fracture energy. Moreover, the thermal conductivities of the junctions were also calculated by MD method. Metal catalysts remaining in the junctions considerably lower the thermal conductivity of the 3D junctions.

ACKNOWLEDGEMENTS

First of all, I would like to thank my advisor -- Dr. Zhenhai Xia. His scientific insights and professional guidance make a huge contribution to this dissertation. Dr. Xia is a creative and honest scientist, and I am deeply impressed by his passion on academic research and teaching. Working with Dr. Xia for more than 5 years, I do have a good time with fresh and meaningful work in both UNT and UA. He demonstrates me a strong sprit to challenge new scientific areas and to troublesome problems, which inspires me not only on my doctoral work but also the whole life. Herein, I heartily appreciate Dr. Zhenhai Xia for his edification, support and patience on my doctorial span.

I would like to thank my committee members -- Dr. Wonbong Choi, Dr. Jincheng Du, Dr. Sundeep Mukherjee, and Dr. Zhiqiang Wang. From qualifier, proposal to defense, they give me very helpful advices and great encouragement. I would like to thank the department faculty and staff for their support and guidance.

I would like to thank my colleagues in Dr. Xia's group, Shihao Hu, Lili Li, Mingtao Li, Zhijun Ma, Craig Smith, Thanyawalai Sujidkul, Yiyang Wan, Jie Wen, Quan Xu, Lipeng Zhang and Zhenghang Zhao. And thank my friends Hui Che, Lu Deng, Niraj Gupta, Siwei Shi, Wei Sun, Han Wu and Ye Xiang. They always help me and make my life enjoyable. Finally, thank my dear family.

TABLE OF CONTENTS

Page

LIST OF FIGURES

Page

CHAPTER 1

INTRODUCTION

1.1 Motivation and Background

Carbon nanotubes (CNTs) and graphene are attractive nanomaterials in both scientific research and industrial fields due to their unique structures and properties. They are both carbon allotropes with similar carbon arrangements; therefore, studies of assembling and design of these two materials are reasonable and meaningful for practical applications. They could work as reinforcements modifying inferior properties of classical materials such as ceramics, metals, polymers, and glass [1-8]. Moreover, hybrid of CNTs and graphene can retain their advantages in maximum. For instance, structures composed of graphene sheets and parallel single-wall or multi-wall CNTs [9-13] were reported to possess huge application prospects.

Both of them are anisotropy in structures and properties. For example, graphene is composed with sp^2 bonds in in-plan direction and atoms interact with van der Waals force [14] in out-of-plan direction, with properties more attractive in in-plan direction than that in out-of-plan direction. In order to make full use of the unique properties of CNT and graphene, a novel nanostructure - 3D CNT graphene nano architecture- has been proposed. The new structure is composed by parallel graphene layers and vertical CNTs, which are connected with C-C covalent bonds, as shown in **Fig. 1.1** [15]. In all three directions, covalent C-C sp^2 bonds — the strongest chemical bonds known in nature [24] — control the stress and energy transportations, improve the mechanical, thermal, and electrical properties in the out-of-plan direction, and maintain properties in the in-plan direction.

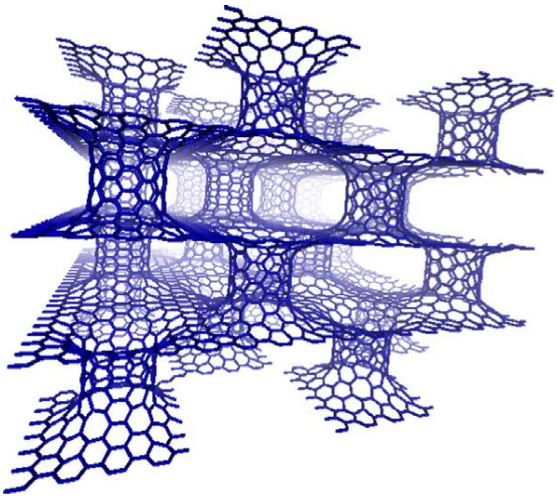

Fig. 1.1 The novel 3D CNT-graphene nano architecture.[15]

Theoretical research has been performed to investigate the mechanical, thermal, and electrical properties [15, 16, 17] of the 3D nanostructures and a few experimental strategies have also been designed to synthesize the 3D nanostructures [14, 18, 19] in laboratory. However, since the CNTs grow fast with over 10 μm long nanotubes in seconds [20] and experimental measurement accuracy is limited, it is very difficult to observe the junction formation and detailed structures of junctions. Even though growth theories of CNTs and graphene have been discovered [21, 22, 23], the growth mechanism and the comprehensive structure of 3D nano architectures remain unclear. Thereby, theoretical research on the growth mechanisms of 3D CNT-graphene nano architectures is necessary, and it could provide fundamental support, original knowledge, and useful process guidelines for laboratorial and industrial fabrication developments.

1.2 Contributions of Dissertation

In this dissertation, I mainly investigate the junction growth mechanisms, and mechanical and thermal properties of junctions in 3D CNT-graphene nano-architectures with quantum

mechanical molecular dynamic (QM/MD) simulations and classical molecular dynamic (MD) simulations.

(1) The vertical CNT growth on a graphene substrate with iron nanoparticles as catalyst was simulated *via* the QM/MD method. Our simulation indicated that the CNT growth was characterized by several stages: in the early stage, short polyyne chains appeared and brunched on the surface of the catalyst, followed by the polygons (pentagons, hexagons and heptagons) growth, and the CNT cage formation and growth in a "base-growth" mode. The junction between CNT and graphene are formed with a mixture of C-C and Fe-C bonds. The catalyst has a strong tendency to move with the growing CNT cage, which facilitated the C-C bonded junction formation. Our simulation pointed out two avenues to produce C-C covalently bonded junctions for the 3D nanostructures. Seamlessly C-C bonded junctions could be produced by: (i) lifting up the catalysts during CNT growth by transforming the CNT growth from "base-growth mode" to "tip-growth mode" with force, and (ii) etching and annealing after the CNT growth to remove iron nanoparticles, leading to the release of carbon dangling bonds at graphene edge from strong Fe-C bonds to form C-C bonds even at relatively low temperature.

(2) Growth processes of 3D CNT-graphene junction on Cu templates were simulated via classical MD simulations. There are two growing mechanisms depending on the size of template holes: i) CNT growth over small hole, and ii) CNT growth inside large hole. Line and point defects were found in the grown CNT, graphene, and junctions. Pentagons and heptagons play an important role in the junction growth especially at the transition region of CNT and graphene. The seamless C-C junction growth mechanisms found in this study provide a theoretic foundation for growth of 3D nanostructures without any catalysts.

(3) Growth processes of filleted junctions in 3D CNT-graphene on alumina templates were simulated via classical MD simulations. Multi-layer CNT-graphene junctions with fillets were formed on the alumina template. A simple analytical model is developed to explain why the fillets take the particular angle (135°). The model predicts that there is a critical fillet angle at which the system energy reaches its minimum value. The predictions are consistent with the MD simulation and experimental observations. Our simulations show that it possible to synthesize high-quality 3D CNT-graphene nanostructures using template methods without catalysts.

(4) Tensile tests of different types of junctions in 3D nanotube – graphene nanostructures were simulated via quantum mechanical molecular dynamic method and classical molecular dynamic method. Filleted junctions with different fillet angles were tested. The 135° filled junction has the strongest fracture strength compared with 120° filleted junctions, 150° filleted junctions , and 180° filleted junctions, proving the preference of 135° fillet angles in experiments. Covalently C-C bonded junctions possess the highest fracture strength and fracture energy. The metal nanoparticles embedded in the junctions between the CNT and graphene significantly reduce the fracture strength and energy. Even when the metal particles are embedded inside junction, the C-C bonded junctions are weakened by the particles.

(5) Thermal conductivities of filleted junctions with fillet angles of 90°, 120°, 135°, 150°, and 180° were calculated with molecular dynamic simulation. Junctions with different angles show different abilities of heat transfer. Junctions with 135° fillet angles have the highest thermal conductivity compared with other junctions. The fillet could have effect on junction thermal dissipation. Thermal conductivities of junctions with iron nanoparticles were also calculated with MD. Compared to pure C-C junction, the junctions with Fe particle embedded have much lower

thermal conductivity, proving that metal catalyst left in junctions could considerably affect the thermal performance.

1.3 References

[1] G.L. Hwang, K.C. Hwang, J. Mater. Chem. 11 (2001) 1722.

[2] J. Liu, H. Yan, K. Jiang, Ceram. Int. 39 (2013) 6215.

[3] Z. Spitalsky, D. Tasis, K. Papagelis, C. Galiotis, Prog. Polym. Sci. 35 (2010) 357.

[4] H. Kim, A.A. Abdala, C.W. Macosko, Macromolecules 43 (2010) 6515.

[5] T. Laha,Y. Liu, A. Agarwal, J. Nanosci. Nanotechnol. 7 (2007) 1.

[6] J. Wang, Z. Li, G. Fan, H. Pan, Z. Chen, D. Zhang, Scripta Mater.66 (2012) 594.

[7] H. Porwal, P. Tatarko, S. Grasso, C. Hu, A. R. Boccaccini, I. Dlouhỳ, M.J. Reece, Sci. Technol. Adv. Mater. 14 (2013) 055007.

[8] B.T.T. Chu, G. Tobias, C.G. Salzmann, B. Ballesteros, N. Grobert, R.I. Todd, M.L.H. Green, J. Mater. Chem. 18 (2008) 5344.

[9] D. Yu, L. Dai, J. Phys. Chem. Lett. 1 (2010) 467.

[10] F. Tristán-López, A. Morelos-Gómez et al., ACS Nano, 7 (2013) 10788.

[11]N. Jung, S. Kwon, D. Lee, D.M. Yoon, Y.M. Park, A. Benayad, J.Y. Choi, J.S. Park, Adv. Mater. 25 (2013) 6854.

[12] V.C. Tung, L. Chen, M.J. Allen, J.K. Wassei, K. Nelson, R.B. Kaner, Y. Yang, *Nano Lett.*, 9 (2009) 1949.

[13] Z. Sui, Q. Meng, X. Zhang, R. Ma, B. Cao. J. Mater. Chem.22 (2012) 8767.

[14] F. Du, D. Yu, L. Dai, S. Ganguli, V. Varshney, A.K. Roy, Chem. Mater. 23 (2011) 4810.

[15] S. Sihn, V. Varshney, A.K. Roy, B.L. Farmer. CARBON 50 (2012) 603.

[16] F. D. Novaes, R. Rurali, P. Ordejón. Acs nano 4 (2010) 7596.

[17] L. Xu, N. Wei, Y. Zheng, Z. Fan, H. Wang, J. Zheng, J. Mater. Chem. 22 (2012) 1435.

[18] Y. Zhu, L. Li, C. Zhang, G. Casillas, Z. Sun, Z. Yan, et al. Nature Commu. 3 (2012) 1.

[19] Z. Yan, L. Ma, Y. Zhu, I. Lahiri, Z. Liu, M.G. Hahm, et al., ACS Nano 7 (2013) 58.

[20] H. Yoshida, S. Takeda, T. Uchiyama, H. Kohno, Y. Homma, Nano Lett 8 (2008) 2082.

[21] A. Maiti, C.J. Brabec, C. Roland, J. Bernholc. Phys. Rev. B 52 (1995) 14850.

[22] V.I. Artyukhov, Y. Liu, B.I. Yakobson, , PNAS 109 (2012) 15136.

[23] H. Chen, W. Zhu, Z. Zhang, PRL 104 (2010) 186101.

[24] M.S. Dresselhaus, G. Dresselhaus, J.C. Charlier, E. Hernandez. Phil. Trans. R. Soc. Lond. A 362 (2004) 2065.

CHAPTER 2

LITERATURE REVIEW

The 3D CNT-graphene nano-architecture is a novel derivant of CNTs and graphene. In order to understand its growth mechanisms, growth mechanisms of CNT and graphene will be reviewed in the beginning of this chapter.

2.1 Growth Mechanisms of Carbon Nanotubes

Carbon nanotubes were discovered by Sumio Iijima in 1991[1], opening a new avenue for material designs and fabrications. It is a new carbon allotrope in the form of cylinder composed by helical carbon atoms, in which sp^2 hybridized bonds generated between adjacent C atoms. CNTs are generally synthesized via chemical vapor deposition (CVD), plasma enhanced chemical vapor deposition (PECVD), and fluidized bed chemical vapor deposition (FBCVD). Growth mechanisms have been proposed to accompany the CNT growth.

2.1.1 Vapor-Liquid-Solid (VLS) Mechanism

Vapor-liquid-solid (VLS) mechanism is firstly proposed by Wagner and Ellis [3] as early as 1964 to describe the single crystal growth. Y. Saito et al. [4, 5] utilized this idea to carbon nano materials. J.Gavillet et al. [2] gave a detailed expression of this VLS mechanism for CNT root growth with aid of metal particle catalysts. He proposed that there are 3 stages as followed:

Stage 1: Metal nanoparticle melts and dissolves carbon atoms (**Fig. 2.1** (a)). At high furnace temperatures, metal particles become liquid state from solid state, which is the “L”. At the same time, carbon sources will decompose to produce C vapor and H vapor. C vapor can be dissolved by the liquid metal particles and hydrogens return to injected vapor [6]. This is the

“V”. Liquid metal particles will be saturated by carbon atoms with continuing source gas feeding.

Stage 2: Struggle between graphene layer growth and nucleation of CNTs (**Fig. 2.1** (b) and (c)). When the furnace temperature goes down to 1500k, solubility of metal will decrease and carbon atoms will segregate out from metal particles. As the temperature drops, metal particles become solid state from liquid state and more carbon atoms segregate out. Herein, J.Gavillet et al. [2] utilized the crystal growth process [7] to illustrate equilibrium states of graphene shells or CNTs. When carbon atoms arrange according to the Frank–van der Merwe process [8], graphene shells will form just like layer-by-layer crystal structure growth. When carbon atoms segregate according to Volmer-Weber [9] or the Stranski-Krastanov processes [10], nucleation of CNTs will occur. After all, carbon structures are determined by kinetic equilibrium states at different experimental conditions.

Stage 3: Carbon nanotubes growth (**Fig. 2.1** (d-f)). Metal particles still dissolve active carbon atoms, and for saturation equilibrium some C atoms segregate out of metal catalysts to participate in the CNT growth (**Fig. 2.1** (d)). Different styles of CNTs exist in experiments. As shown in **Fig. 2.1**(e) and (f), CNTs may extrude out of amorphous carbon structures or graphene layers because in the initial stage amorphous carbon and graphene layers nucleate but CNT does not. A new nuclei of CNT emerges between metal particles and these structures. The CNT grows longer and comes out of their surroundings with continuous carbon feeding. This mechanism is similar with the idea of growth mechanism of multi-wall CNTs [11].

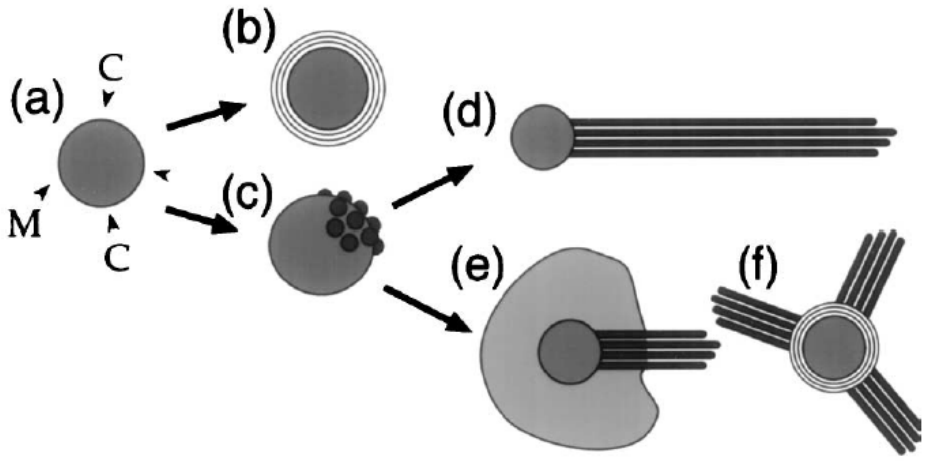

Fig 2.1 Three stages of VLS mechanisms of root growth CNT. [2]

2.1.2 CNT Root-Growth and Tip-Growth

As observed in experiments, in some cases catalysts sit on the base of newly grown CNT [13], where sometimes they are on the tip of the CNTs [14]. S.B. Sinnott et al. [12] concluded that the multi-wall CNTs can grow according to root-growth mode and tip-growth mode (Fig. 2.2). Herein, interactions between the metal catalyst and support substrate determine the growth mode. Root-growth mode: When metal particles bond substrate strongly, carbon cages segregate out from top surface of metal catalysts after the metal is saturated by carbon atoms, and CNT forms from carbon cages with long-time carbon source feeding and heating. Metal particles are left on the substrate beneath CNT due to tight bonding. Tip-growth mode: metal particles attach to the substrate loosely. The precipitation of carbon structure can break the weak bonds between metal catalyst and substrate. The CNT grows longer between substrate and catalyst particles and lifts particles up. Until particles completely separate from the substrate, it can be found sitting on the top of the CNT. Vladimir I. Merkulov et al. [14] and Kumar M. [16] made similar conclusions on the CNTs and carbon nanofibers growth.

It is obvious that the nanoparticle status is an essential factor to effect CNTs growth; therefore, modification of deposition method and selection of substrate and catalyst material are necessary for controllable CNTs growth.

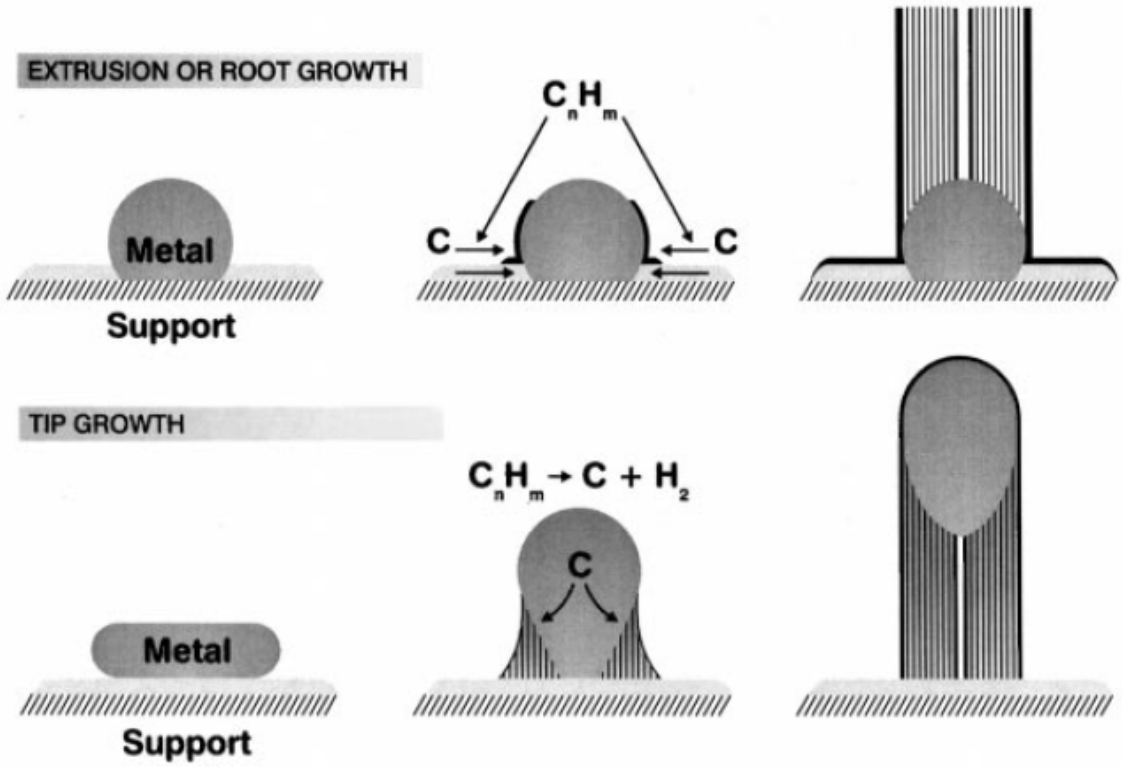

Fig. 2.2 Schematics of CNT root-growth and tip-growth. [12]

2.2 Growth Mechanism of Graphene

Graphene, with similar atom bonding as CNTs, is believed to be a novel electrical material due to its super electron conductivities and carrier motilities. Massless Dirac fermions behavior, electric field effect, and Hall effect was revealed by Novoselov, K. S. et al. [19, 20], providing graphene huge applications such as transistors and circuit electrodes[25, 26], optical electronics[23], and photovoltaic cells [24]. Until now, the avenues to grow graphene are mainly chemical exfoliate [27, 32, 33, 34], decomposition of graphite oxide [28-31], chemical vapor

deposition method (CVD) upon metal substrate [21, 22, 35-41], and epitaxial grow via vacuum annealing of single crystal silicon carbide [16, 17, 18]. Mechanisms of graphene growth highly depend on growth method and substrate materials utilized in experiments.

2.2.1 Growth Mechanism of Graphene Growth on Nickel and Copper Film Catalysts

A range of metals has been employed as catalyst in the CVD process to grow graphene layers, including Ru, Ir, Co, Re, Ni, Pt, Pd, and Cu [43-53]. Except Cu, obtained graphene is multi layers on metal films. When utilizing Cu film, high quality single layer graphene was fabricated in large scale [55, 56].

X. Li et al. [54] found graphene growth mechanisms on Cu and Ni through ^{12}C ^{13}C isotopic labeling of methane. In the synthesis process, carbon source $^{12}CH_4$ was injected into the furnace first, and then $^{13}CH_4$ was injected. When the graphene layers grow on Ni catalyst, ^{12}C and ^{13}C atoms in graphene are disturbed in disorder, while the graphene layers grow on Cu catalyst, ^{12}C exits in early grown part and ^{13}C in latter grown part. They believe that C solubility difference of Ni and Cu leads to this phenomena:

For Ni, the C solubility is high. Like CNT growth, C atoms are dissolved into Ni film catalyst first, and then C atoms segregate out of Ni surface as the metal film reaches solubility limit. Thus, in this case, both ^{12}C and ^{13}C are dissolved in Ni film until it is saturated. Along with temperature decreasing and Ni solubility getting lower, both types of C atoms segregate and form graphene with randomly distributed ^{12}C and ^{13}C atoms. Since there is persistent C atoms segregations, nuclei of graphene is in a large quantity leading to over lapped graphene layers (**Fig. 2.3** (a)).

For Cu, C solubility is extremely low. As $^{12}CH_4$ is injected into the furnace, just few ^{12}C atoms are dissolved in the Cu film catalyst after decomposition, and most ^{12}C are absorbed onto the Cu surface generating carbon structures. Then the $^{13}CH_4$ feed into the system and ^{13}C atoms are produced. Due to low C solubility, the ^{12}C structures cannot hold more C atoms and newly introduced ^{13}C atoms attach onto fringe of ^{12}C structures. Therefore, the C atoms arrangement in graphene is consistent with ^{12}C and ^{13}C introduction sequence (**Fig. 2.3** (b)).

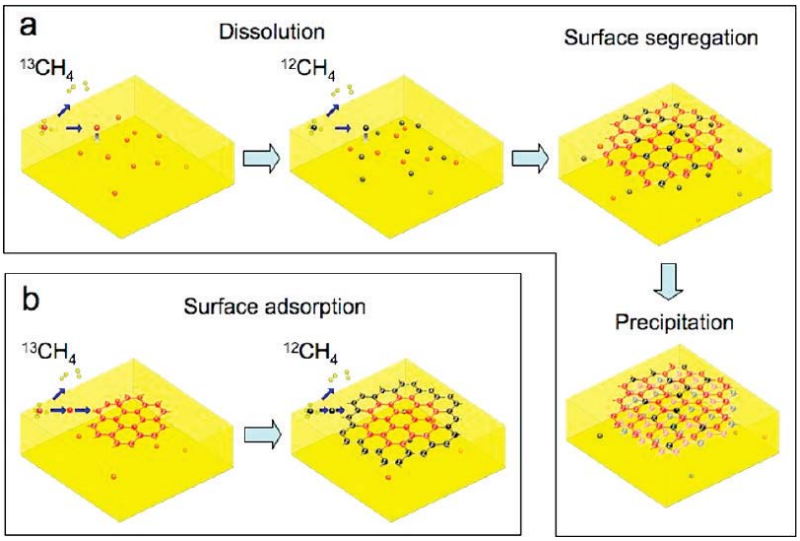

Fig. 2.3 Schematics of graphene growth on Ni and Cu film with ^{12}C ^{13}C isotopic labeling of methane as carbon source. (a) Over lapped graphene grows on Ni film with ^{12}C and ^{13}C arranged randomly. (b) Single layer graphene grows on Cu film with ^{12}C and ^{13}C arranged sequentially. [54]

For graphene growth on top of Cu film, Mattevi et al. [57] described the detailed growth mechanisms with 3 steps. Step 1: Cu film was placed properly, and copper oxide cannot be avoided on its surface. (**Fig. 2.4** (a)) The copper oxide is reduced to Cu in the H_2 gas at high temperature environment. Cu atoms on the surface will rearrange to equilibrium state. Step 2: Introduced methane decomposes into C gas and H gas, and C atoms nucleate on local areas of

Cu. With continuous heating and carbon source feeding, nuclei grow larger (**Fig. 2.4** (b)). Step 3: Small graphene flakes connect to each other to form a whole piece of graphene layer (**Fig. 2.4** (c)).

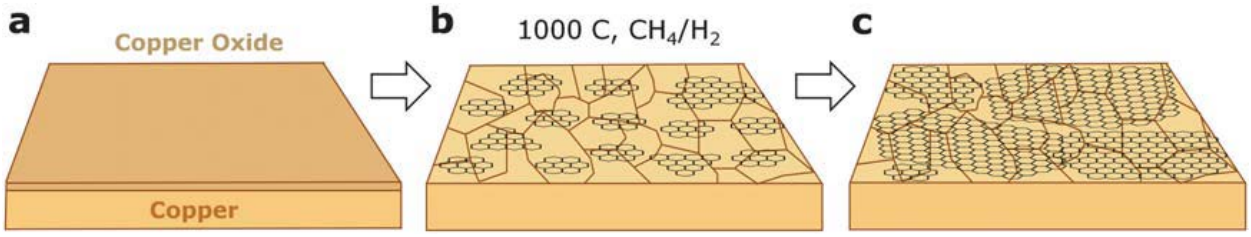

Fig. 2.4 Schematics of single layer graphene on Cu film with CH4 as carbon precursor. (a) Cu film is placed properly. (b) Nucleation of graphene and small flakes. (c) A whole piece of graphene. [57]

2.2.2 Graphene Epitaxial Growth Mechanism on Crystal Silicon Carbide

Epitaxial growth of graphite with high vacuum can trace back to 1960s [63] and researchers modified this method to grow multi-layer graphene [64]. In this method, SiC (0001) surface is eroded and releases carbon atoms to grow multi-layer graphene. This epitaxial growth method provides huge potential for direct electronic applications [58], since the direct product is the graphene with silicon substrate, which avoid transportation of graphene from metal substrate for further applications. Terrace, fingers, single-layer graphene, bi-layer graphene, tri-layer graphene, and remained silicon are all observed by different processes. Even though there is no consensus on the detailed graphene growth mechanisms, two different proposals are reviewed.

(i) Bottom-up Growth of Epitaxial Graphene [59]

Utilizing scanning tunneling microscopy (STM), H. Huang et al. [59] believed that epitaxial multi-layer graphene grows according to the bottom-up strategy. It is observed that the

first top graphene layer can completely blanket the juncture of the first layer and the second layer graphene as well as the juncture of the second layer and the third layer graphene. Also, the second top graphene layer can completely blanket the juncture of the second layer and the third layer graphene. The first top single SiC bi-layer decomposes and releases C atoms to form a single graphene layer with high temperature annealing. Then, the second SiC bi-layer beneath newly grown graphene decomposes again to generate the second graphene layer between the first graphene and SiC substrate. The third layer graphene generates in the same way. The first graphene layer can completely blanket the juncture of first layer and second layer graphene, and so forth.

(ii) Different Decomposition Speeds of Neighboring Terraces is The Main Force of Multi- Layer Graphene Growth. [60]

Some researches [61, 62] put forward similar mechanisms for epitaxial graphene growth upon single crystal SiC substrate. M. Hupalo [60] proposes that the silicon desorption in SiC crystal masters the graphene layers growth. Single crystal SiC is in stair construction with terrace 1, terrace 2 and terrace 3. (**Fig. 2.5** (a)) These 3 terraces decompose in different speeds, with terrace 1 bigger than terrace 2 and terrace 2 bigger than terrace 3. Terrace 1 decomposes fast and leaves carbon atoms to nucleate and active the graphene growth. (**Fig. 2.5** (b)) Terrace 1 gradually chases up to terrace 2 to form a double layer of SiC and continues to decompose. They move forward together but some parts still fall behind due to speed mismatching, which causes some fingers at the fringe areas. (**Fig. 2.5** (c)) Combined terrace 1 and 2 finally chase up to terrace 3 forming a three-layer SiC step. (**Fig. 2.5** (d)) Therefore, a single graphene layer covers the original exposed terrace 1 areas, double layer graphene covers the original exposed terrace 2

areas (double layer SiC), and three layer graphene covers the original exposed terrace 3 areas (three layer SiC).

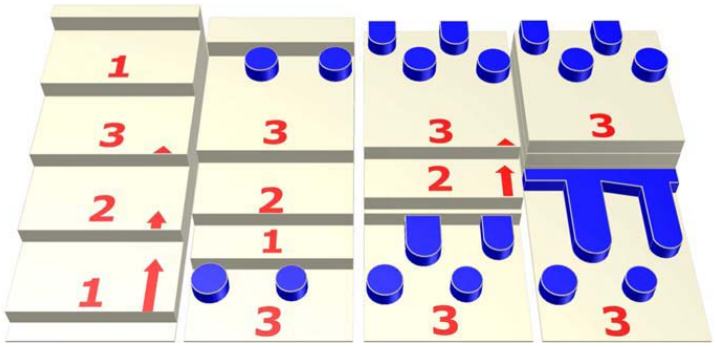

(a) (b) (c) (d)

Fig. 2.5 Schematics of epitaxial graphene using crystal sic (0001) substrate. [60]

2.3 Fabrication of 3D CNT Graphene Nano-architectures in Laboratory

A few experimental approaches have been developed to fabricate the 3D nanostructures. There are three main methods: i) assemble as-grown graphene and CNT, ii) growth vertical CNTs on pre-existent graphene and iii) growth of CNT and graphene through one-step. CNTs and graphene growth techniques have been well developed, on which growth of 3D CNT-graphene would rely. Therefore, all of the approaches are based on CVD or PECVD to produce graphene and CNT.

2.3.1 Self-Assembly of As-Grown CNT and Graphene to Prepare 3D CNT-Graphene Nanostructures

Fan et al. [65] prepared 3D CNT-graphene sandwich structures with CNT pillars grown in between the graphene layers by as-grown CNT and graphene self-assembly via CVD. Graphene oxide and CNT was prepared respectively, and then they are mixed in a specific mass

ratio and heated to 750 °C. This method was widely utilized to prepare the thin hybrid film of carbon nanotubes with graphene sheets [66-71]. During the synthesis, the graphene oxide was reduced to graphene layers and CNTs attach to them because of high surface energy of graphene oxide. This method originates from layer-by-layer (LBL) assembly techniques of hybrid polymers structures [72-74] and now it is employed to prepare the 3D carbon nanostructures. The advantage of this method is that it is flexible to combine various nanostructures such as single wall CNTs, multi-wall CNTs, graphene layers, nanoparticles, and so on, because the components are prepared separately. The shortcoming lies in that the connection configuration between CNTs and graphene layers is dubious. Chemical bonds may form during heating or physical contacts may only occur between CNT and graphene. For 3D pillared CNT-graphene structure, it is difficult to keep CNTs maintaining vertical during assembling.

Yu et al. [75] obtained 3D pillared CNT-graphene structures from as-grown CNT and as-grown graphite with plasma-enhanced chemical vapor deposition (PECVD) without specific introduction of catalysts. It is found that few-layer graphene (FLG) grew on vertical CNT as shown in **Fig. 2.6.**, and the pre-placed CNT grew bigger during the PECVD process. The Choi [81] group got the 3D structure via hot lamination at 70 °C by assembling as-grown CNT and graphene.

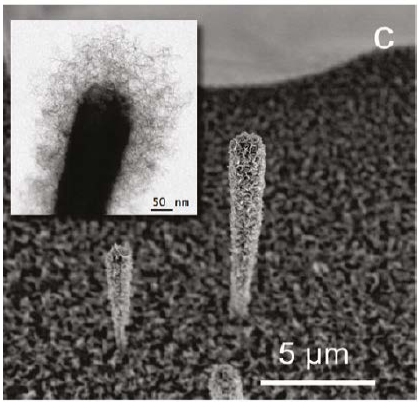

Fig. 2.6 SEM image of FLGs grown on vertically aligned CNTs; the inset is a TEM image of the tip of a CNT_FLG, where the CNT stem (dark) is clearly distinguished from FLGs (bright). [75]

2.3.2 Two-step Growth of 3D CNT-Graphene Nanostructures

This fabrication procedure contains two main steps: Step one, graphene or graphene oxide is prepared by CVD or PECVD followed by catalyst depositions; Step two, the vertical CNT grows on the catalyst and graphene by CVD. This is the most popular method to synthesize 3D CNT-graphene nanostructures, incorporation of growth process of graphene and CNTs. Comparing to the method in 2.3.1, it is much more feasible to control CNT configuration and distribution on graphene films. As shown in **Fig. 2.7**, the CNT array is in high quality grown on graphene films in Lee's work [76]. Du et al. [85], Dong et al. [77], Bae et al. [78], and Wen et al. [79] also obtained 3D CNT-graphene nanostructure with similar methodologies, respectively.

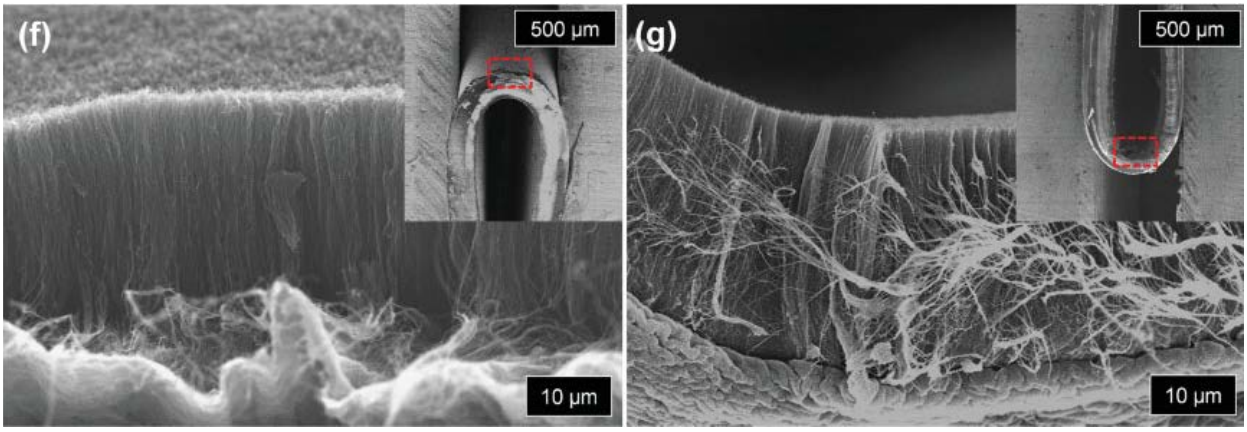

Fig. 2.7 High- and low- (inset) magnification SEM images of a carbon hybrid film on a poly (ethylene terephthalate) film bent outward (f) and inward (g). [76]

Moreover, Tour's group [80, 81, 82] developed a modified method based on the two-step growth. After deposition of catalysts (usually Fe or Co) on grown graphene layers, an Al_2O_3 film was patterned on the catalyst. It is believed that the adhesion force between Al_2O_3 film and Fe nano particle is relatively high compared to that between graphene and Fe particle. Consequently, CNTs can only grow out between graphene and Fe particles, so that Fe particles and Al_2O_3 are lifted up together by the growing CNTs. Therefore, newly grown CNTs and graphene are connected through seamless C-C covalent bonds.

This strategy is successful for fabrications of 3D nano structure and chemical bonds between vertical CNTs and graphene could be achieved; however, it is not clear that the connections between CNT-graphene layers are chemical bonds or only physical contacts. Moreover, big gaps are observed between CNT-graphene layers as shown in **Fig. 2.8**. Therefore, fabrication of covalent bonded 3D carbon nanotube-graphene nano-architectures remains a big challenge.

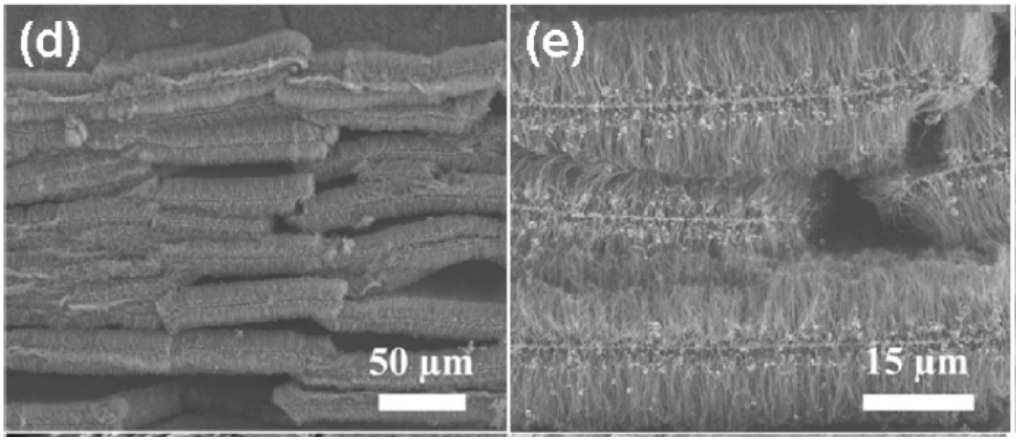

(a) (b)

Fig. 2.8 (a-b) Typical SEM images of the 3D pillared VACNT graphene architectures under different magnifications. [85]

2.3.3 One-step Growth of 3D CNT Graphene Nanostructures

Zhao et al. [83, 84] put forward a one-step growth of the 3D structures, which is an *in situ* growth process. In this method, layered double hydroxide (LDH) (for example: FeMgAl LDH) was utilized to be a catalyst precursor instead of metal particles. At high temperatures (950˚C) the FeMgAl LDH can produce nanoparticles to work as CNT growth catalysts and consistent templates for graphene growth. Therefore, the 3D CNT-graphene structure can be fabricated through one step. Kondo et al. [100] fabricated 3D nano structures in one step using two layers of film- cobalt (Co) film and titanium nitride (TiN) film- as catalysts, both of which must be optimized carefully to ensure the 3D structure growth. Similarly, Paul et al. [101] grew 3D CNT-graphene *in situ* with iron nano particle catalysts deposited on copper film.

Although the one-step growth method has not been widely employed to produce 3D nanostructure due to limited empirical data, it provides a new strategy for complex nanostructure synthesis and it is potential to solve the “big gaps” in section 2.3.2, since all the components in

structure are produced simultaneously. More investigations are needed to improve the one step methodology.

2.3.4 Electrical Properties of 3D CNT-graphene Nanostructure

3D CNT-graphene nanostructures exhibit considerable electrochemical properties due to large surface area [80], low contact resistance [86], large number of activation sites, and efficient ion pathways [78]. They have better optoelectronic and gas sensing properties than CNT and graphene [75]. Although different configurations of 3D CNT-graphene nanomaterials are produced by various methods, super capacities of the new structures have been tested in experiments [78, 81, 82, 83, 86]. Consequently, they have potential applications such as lithium-ion batteries [78], super capacitors [65], drug deliver, and energy storage [83].

It is necessary to understand the nature characteristics of this 3D structure for further fabrication designs and practical applications. However, mechanical, thermal, and detailed electrical property tests could not be carried out due to structure uniqueness and experimental limitations. Fortunately, simulation and modeling provide new avenues to property investigations, especially for mechanical and thermal property investigations, which will be discussed in next section.

Electrical transports of 3D CNT-graphene structures with various CNT and junctions were studied with the first-principles method. For large scale 3D CNT-graphene structures, alternations of CNT lengths and junction shapes can significantly change the whole structure's configurations, and further change overall properties. CNT and junction types could influence conductance of the whole 3D nano structure. When it is composed of metallic CNTs, electrical transportations are mainly controlled by junction types (graphene defects connecting to CNT),

regardless of CNT length. When the structure is composed of semiconductor CNTs, electrical transportations are mainly controlled by CNT length, regardless of junction types. [92]

2.4 Theoretical Studies on 3D Carbon Nanotube-Graphene Network Nanostructures

2.4.1 Theoretical Foundations on Junctions of 3D Carbon Nanotube-Graphene Network Nanostructures

Junctions are the key component for the 3D CNT-graphene network structures, connecting the vertical CNTs, and horizontal graphene layers. Because discrete geometric procedure [89] between vertical CNT and horizontal graphene is completely new for carbon materials, theoretical studies have been done to explore the existence foundations of the 3D junction.

Duangkamon Baowan et al. [87] believed that junctions between CNT and graphene can be achieved through graphene defects, which provide dangling bonds to connect the CNT open ends. Using the Euler's theorem, it is found that junction architectures are highly dependent on the graphene defects. It proved that for (8, 0) nanotube, #6 graphene defect (**Fig. 2.9**(a)) is the most favored configuration to form the 3D structure and for (4, 4) nanotube, #9 graphene defect (**Fig. 2.9** (b)) is the most favored configuration. The points of view are also proven by Cox et al. [89] through minimization of covalent bond energies. Pristine CNT was inserted into the graphene defect hole and the C-C bonds formed between the graphene hole and CNT and the CNT was deformed due to new bonds [90].

(a) (b)

Fig. 2.9 Defects on graphene could form junction with (a) (8,0) CNT and (b) (4,4) CNT. [87]

Li et al. [88] designed a number of junction models based on the first principles density functional theory (DFT). Different CNT and graphene nano-ribbon units were connected via covalent linkages such as peptide (-CONH-) and disulfide (-S-S-), avoiding graphene defects. In **Fig. 2.10**, the three models are cited from Li's eight junction models. Types of CNTs influence the CNT and graphene reaction. The researchers got the results that the armchair CNT and graphene junction formation is an exothermic procession and zigzag CNT and graphene junction formation is an endothermic procession. The models involve chemical elements of S, N, and O besides C, which are believed to provide potential of new electrical properties other than CNT and graphene.

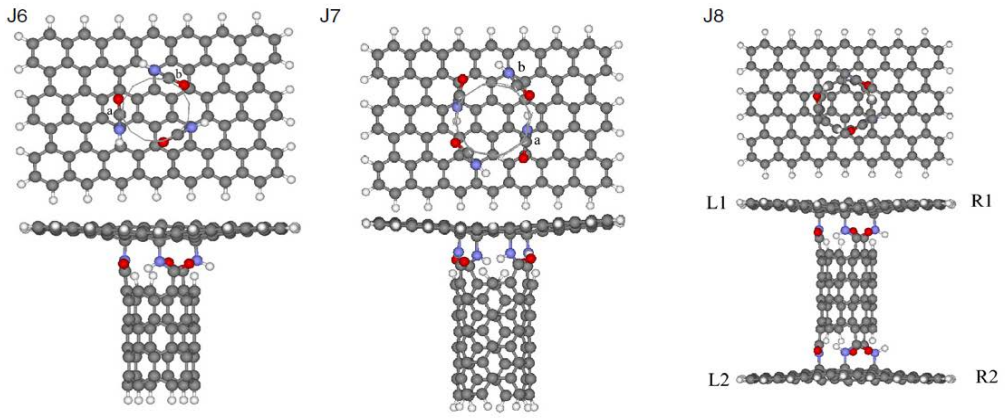

(a) (b) (c)

Fig. 2.10 Relaxed geometries of different CNT & graphene junctions. (a) Junction composed of Zigzag-graphene (N=6), CNT (6, 0) and –CONH– linkage. (b) Junction composed of Zigzag-graphene (N=6), CNT (4, 4) and –CONH– linkage. (c) Junction composed of two zigzag-graphene (N=6), CNT (6, 0) and –CONH- as linkage. [88]

As we know, CNT and graphene, components of 3Dstructure, are experimentally stable and reliable. Above studies also provide theoretical fundaments on stability of junction, so that discussions on large scale 3D carbon nanotube graphene structure are meaningful and justifiable.

2.4.2 Properties of Large Scale 3D Nanotube Architectures Investigated via Simulations

As we referred to in part 2.3, the 3D structure obtained in the laboratory is not high quality, and overall property investigations could not be done due to experimental restrictions though some electrical properties have been tested. Multi-scale simulations provide more approaches to study properties of this new structure. Some simulation work has been done on the mechanical, thermal, and electrical properties. Electrical properties obtained via modeling have been referred to in part 2.3.4.

For 3D structure, the in-plan and out-of-plan structures are distinct, making the properties anisotropic in these two directions [91, 95]. Variation of 3D nano configurations could be

achieved by changing the length of vertical CNTs and the space between CNTs. Thus, researchers look into mechanical and thermal properties with different 3D structures.

In-plan and out-of-plan mechanical properties are affected by CNT tube length and inter-CNT distance [93, 95]. It is shown that short CNT tube length produce higher in-plan Young's moduli and shear moduli; small space between CNTs produce higher out-of-plan Young's moduli and shear moduli. Graphene sheet moduli is extremely high in-plan direction, while CNT moduli in-plan is much weaker than Graphene, so that in-plan strength is weakened by involved CNTs. Reasonably, shorter CNT tube can reduce the weakness brought by CNT. In out-of-plan direction, CNT possesses high moduli but graphene is relatively weak, for which reason the out-of-plan moduli could be increased by higher CNT density-- smaller space between CNTs. Therefore, shorter CNT tube length and smaller space between CNTs could strengthen the 3D nano material in both in-plan and out-of-plan directions [95]. High Young's modulus has been tested [94, 95], providing a reliable foundation for applications in nanoscale electronics [91].

Thermal properties are also affected by CNT tube length and space between CNTs. CNT-graphene transition area could cause more phonons scattering than other areas [94]. It is possible to tailor CNT tube length and space between CNTs to obtain desired thermal properties for the 3D nano structures [94]. At the transition area of the 3Djunction, due to incongruity of structure and state densities, phonon scatterings are aggravated leading to lower thermal conductance compared to pure CNT [99]. In practical applications, heat dissipation is crucial for device performance and life span, so that thermal isotropic nano materials are needed. Loh's study shows that the vertical CNT in 3D nano structure could incorporate heat extraction in vertical direction and graphene in horizontal direction [99].

2.4.3 Applications of the 3D Carbon nanotube-graphene Nano Architectures

3D CNT-graphene nano material has plenty of nano hollow space, CNT tubes and graphene layers inter space, providing huge capability of gas storage [85, 98], adsorption, and separation [97]. Dimitrakakis et al. [98] simulated hydrogen storage potential of 3D nano structure with multi-scale theoretical methods. Lithium cation is crucial to improve the H storage since carbon atoms interact weakly with H atoms. The researchers proved that the new structure meets the requirements of United States' Department of Energy (D.O.E.) for H storage container. Similarly, Krypton and helium mixture was separated by 3D CNT-graphene nano structure with molecular dynamic simulations [97]. It is found that the atoms with high density tended to flow into the CNT tube, so that separation is more successful for mixture with two more different specials.

Outstanding electrical properties of 3D CNT-graphene nano structure are on account of large active surface area and rapid charge transfer [77], providing huge potentials of applications in nanoelectronics such as supercapacitors, Li-ion batteries, and field-emitter devices.

Covalent C-C boned 3D CNT-graphene nanomaterials, with low interface resistance, are potential electrodes for high efficient supercapacitors, providing increased energy density and fast AC response compared to commercial supercapacitors [82][75]. Du et al. [85, 86] illustrated that supercapacitors made by 3D CNT-graphene nanomaterials possess high rate capability and excellent cycling ability. Zheng [81] et al. fabricated supercapacitors using CNT-graphene and porous nickel, with advanced functions than CNT- metal systems.

Furthermore, covalent C-C bond 3D CNT-graphene nano structures could be utilized to fabricate new electrodes for batteries and fuel cells [85]. Both cathode and anode [78, 86] with extraordinary rate performance for Li-ion batteries could be made by this 3D material due to its

high electrical conductivities [83]. It is believed that doping could enhance applications of 3D structures on fuel cells [81], and energy storage capabilities of graphene with doping has been studied widely [102].

Researchers have proposed that 3D CNT-graphene nano structures could be used to fabricate high performance field emitting devices due to their excellent interfacial contacts and volume utilizations [81]. Lee et al. [76] has implanted 3D CNT-graphene nano structures into filed emitting devices with high reliable emission currents obtained. Zheng et al. [81] also synthesized 3D CNT-graphene upon porous nickel films, which was utilized for high efficient field emitting devices. They concluded that the quality of CNT-graphene influences behavior of devices. That is, when both sides of Ni film were covered by 3D CNT-graphene nano structures, high field-emission properties could be achieved. When just one side of Ni film was covered by 3D CNT-graphene nano structures, device performance was not attractive.

It is believed that 3D CNT-graphene nano structure can be employed as nanoscale sensors such as gas pressure and position detections [91]. Dong et al. [77] have shown that covalent 3D carbon materials have the excellent sensitivity and low lower-detection-limit as biosensors [77]. 3D carbon materials also have potential to be employed as thermal transport materials [96], photo catalysts [79], actuators [101], and component units for nanoscale integrated devices [85].

2.5 Simulation Methodology

Property investigation of 3D CNT-graphene nanostructure is carried out by modeling methods due to the structure complication and laboratory apparatus limitations. Modeling can deal with materials in small scales such as atoms and electrons, so it is very helpful to understand

the 3D CNT-graphene nano structures. Molecular dynamics, first principles, and finite element analysis are primarily used computational methodologies.

2.5.1 Molecular Dynamics

Molecular dynamics (MD) are widely utilized to simulate nanoscale systems. Mechanical and thermal properties of 3D CNT-graphene nano structures are analyzed successfully by MD simulations. It is based on classical mechanics to solve Newton's Second Law of motion ($F = ma$) for N-body systems with velocities and forces of particles obtained during simulation durations. Interactions between particles are described with empirical force fields to compute dynamic behaviors of atomic structure. In N-body systems, Newton's second law of motion is:

$$m_i \frac{dv_i}{dt} = f_i = \sum_j F_2(r_i, r_j) + \sum_j \sum_k F_3(r_i, r_j, r_k) + \cdots$$

$$v_i = \dot{r}_i \tag{2.1}$$

$$f_i = -\frac{\partial U_{potentail}(r_1, r_2, r_3 \cdots r_N)}{\partial r_i} \tag{2.2}$$

Where m_i, v_i , and r_i are the mass, velocity, and position of particle i. f_i is the force exerting on particle i, which can also be expressed as a gradient of total potential energy respective to the positions (equation (2.2)). F_2 and F_3 are pairwise and three-body interactions and many-body interactions could be involved if needed. In order to get dynamic behavior of particles, initial positions and distributions of velocities have to be provided. Initial positions should obey stable material structures that usually come from experimental results. Velocity distributions are randomly selected via Maxwell-Boltzmann or Gaussian distribution. Requested temperatures are created with scaled velocities.

2.5.1.1 Integration Algorithms

In order to get trajectory of particles, Newton's law of motion was integrated numerically with the finite difference method, in which motion integration is divided into many small steps with time step of δt as shown in equation 2.3. In the numerical integration algorithm, it is supposed that positions, velocities, and accelerations obey the Taylor series expansion:

$$F(t+\delta t)=\sum_{n=0}^{\infty}\frac{F^{(n)}(t)}{n!}(\delta t)^n \quad (2.3)$$

In molecular dynamic simulations, there are mainly four types of integration algorithms: Verlet algorithm, Leap-frog algorithm, Velocity Verlet, and Beeman's algorithm.

(a) Verlet algorithm

According to Tayler series expansion, velocities at time t+ δt and t- δt can be written as:

$$r(t+\delta t)=r(t)+\delta t\, v(t)+\frac{1}{2}\,\delta t^2 a(t)+\cdots \quad (2.4)$$

$$r(t-\delta t)=r(t)-\delta t\, v(t)+\frac{1}{2}\,\delta t^2 a(t)-\cdots \quad (2.5)$$

Adding equation (2.4) to equation (2.5) and omitting higher order terms, we can get

$$r(t+\delta t)=2r(t)-r(r-\delta t)+\delta t^2 a(t) \quad (2.6)$$

Thus, position at time t+ δt can be calculated from position and accelerate at time t and position at t- δt. Velocity at time t+ δt is computed by equation:

$$v(t)=[r(t+\delta t)-r(t-\delta t)]/2\delta t \quad (2.7)$$

Verlet algorithm performs simply and directly with modest memory demand. However, the result is not accurate enough since the term $\delta t^2 a(t)$is much smaller than the term$(2r(t)-r(r-\delta t))$.

(b) Leap-frog algorithm

$$r(t+\delta t)=r(t)+\delta t\, v(t+\frac{1}{2}\delta t) \quad (2.8)$$

$$v\left(t+\frac{1}{2}\delta t\right)=v\left(t-\frac{1}{2}\delta t\right)+\delta t\, a(t) \tag{2.9}$$

The above equations give position at time t+ δt and velocity at time t+$\frac{1}{2}$δt, so that position and velocity do not come out at the same time, that is, they leap over each other. To get the velocity at time t+ δt, the following equation can be used:

$$v(t)=\frac{1}{2}\left[v\left(t-\frac{1}{2}\delta t\right)+v\left(t+\frac{1}{2}\delta t\right)\right] \tag{2.10}$$

This method gives demonstrable velocities with asynchronous velocity and position, meaning that at specific position, the contribution of kinetic energy to total energy could not be calculated simultaneously.

(c) Velocity—Verlet algorithm

The position and velocity at time t+ δt can be calculated from position, velocity, and acceleration at time t.

$$r(t+\delta t)=r(t)+v(t)\delta t+\frac{1}{2}a(t)\delta t^2 \tag{2.11}$$

$$v(t+\delta t)=v(t)+\frac{1}{2}[a(t)+a(t+\delta t)]\delta t \tag{2.12}$$

(d) Beeman's algorithm

Position and velocity are calculated by following equations:

$$r(t+\delta t)=r(t)+v(t)\delta t+\frac{2}{3}a(t)\delta t^2-\frac{1}{6}a(t-\delta t)\delta t^2 \tag{2.13}$$

$$v(t+\delta t)=v(t)+v(t)\delta t+\frac{1}{3}a(t)\delta t+\frac{5}{6}a(t)\delta t-\frac{1}{6}a(t-\delta t)\delta t \tag{2.14}$$

They are calculated in a more accurate way with more storage and simulation time needed.

2.5.1.2 Ensembles Utilized in Molecular Dynamic Simulation

Molecular dynamic simulations execute in a specific ensemble. An ensemble describes a cluster of systems, which have the same macroscopic properties and thermal dynamic status but various motion status. Widely employed ensembles are Microcanonical ensemble (NVE), Canonical Ensemble (NVT), Isobaric-Isothermal Ensemble (NPT) and Grand canonical Ensemble (mVT).

(a) Microcanonical ensemble (NVE)

NVE is an isolated and conserved ensemble, in which system evolution is according to isoenergetic orbit. In the MD simulation, atom quantities (N), system volume (V) and total energy (E) keep constant. Microcanonical ensemble describes the isolated and conserved system which does not have energy exchange with environment. It could not be used to govern macroscopic properties.

(b) Canonical Ensemble (NVT)

Total momentum maintains zero in NVT ensemble, and atom quantities (N), system volume (V) and temperature (T) keep constant. At a constant temperature, the total energy of the whole system varies to exchange energy with environment. To keep the temperature constant, thermostats could be employed, such as Nosé-Hoover thermostat, Berendsen thermostat, Andersen thermostat and Langevin dynamics.

(c) Isothermal–isobaric (NPT) ensemble

Atom quantities (N), system pressure (P) and temperature (T) keep constant. The same as NVT ensemble, thermostats are needed to control temperature. Besides, barostats are demanded

to conserve the pressure. Usually, pressure P is controlled through changing system volume V because P and V are conjugates.

(d) Grand Canonical (GVT) or (GPT) Ensemble

System temperature (T), chemical potential of the particle reservoir (μ) and system volume (V) or system pressure (P) keep constant. This ensemble describes a system which has energy exchange and particle exchange with environment.

Molecular dynamic simulation is a powerful tool to study nano-sized materials. It provides a complemental avenue for laboratory experiments to research fundamental theorems and properties.

2.5.1.3 Nonequilibrium Molecular Dynamics

Thermal transport properties [91, 94, 96] were studied with non-equilibrium molecular dynamics (NEMD). As temperatures on different parts of the whole system are various, then heat will flow from high temperature parts to low temperature parts. The temperature gradients drive the system away from equilibrium to non-equilibrium. NEMD can calculate thermal transport coefficients. Motion equations for NEMD [105] is

$$\mathrm{m}\ddot{r} = \dot{p} = F(r) - \zeta p = F(r) - \zeta \mathrm{m}\dot{r} \qquad (2.15) \quad [105]$$

ζ is a positive "friction coefficient ", maintaining kinetic energy steady; r is the position; p is the momenta of the particle; m is the mass of the particle; $F(r)$ is the force acting on position r. The simple motion equation meets 3 requirements [105]: (i) supposing the force changing in a linear

manner - ζp; (ii) Liouville Theorem [107] governs phase-space distribution function; (iii) phase-space distribution function follows Gibbs' equilibrium form.

To maintain the stable non-equilibrium status, thermostats have to be involved in NEMD which could lower the calculation precision. Also, NEMD takes long time to converge for transport coefficients calculations. To modify these shortcomings, Müller-Plathe et al. [108] proposed Reverse Non-equilibrium Molecular Dynamics (RNEMD) for non-equilibrium system. This method has been employed to calculate the thermal properties of 3D CNT-graphene nano structures [91, 96]. As shown in experiments, the temperature gradient drives the heat flux. In RNEMD, heat flux is introduced and temperature gradient is achieved from calculation. That is, the cause and effect are reversed. Heat flux J_z in Z direction can be described as:

$$J_z = -\lambda \frac{\partial T}{\partial z} \tag{2.16}$$

λ is the transport coefficient.

From system kinetic energy, temperature can be obtained according to equation:

$$\frac{3Nk_BT}{2} = \frac{1}{2}\left(\sum_i^N m_i v_i^2\right) \tag{2.17}$$

Compared to equilibrium MD and NEMD, RNEMD method owns some specific advantages such as no thermostat, no simulation wall, and converging easily.

2.5.2 Finite Element Method

Finite element method (FEM) is an excellent tool to study properties of complicated structures. Sihn et al. [93, 95] obtained elastic moduli and Poisson's ratios of 3D CNT-graphene nano architecture with this method.

Finite element method is a type of numerical analysis, calculating the approximation of mathematic equations for large piece of objectives. Since it is hard to get the governing equation for the complex model, it is divided into large number of small parts, so called elements, and nearby elements are connected with nodes which support forces in mechanical problems. For each element, mechanical problems are usually described with a governing equation and boundary conditions. Combining all the element equations, the approximate solutions for the entire model can be obtained. The mathematic equations are

$$[K]\{u\} = \{F\} \tag{2.18}$$

For elastic problems, $\{F\}$ represents force, $\{\mathrm{u}\}$ represents displacement and $[K]$ are stiffness matrix.

FEM method is extremely powerful to solve sophisticated systems. The model shape can be extremely complex, such as irregular shape, and combined configurations, which is the dominant superiority. It can deal with a wide range of materials including metal, polymers, ceramics, composites biomaterials and so forth, and 3D CNT-graphene nano structures [95] were investigated as referred above. A lot of structure properties are in research by this method, including solid mechanical problems [123, 124], thermal dynamics and heat transportations [125], hydromechanics [126], and electric field issues [127]. During parameter setup and

calculations, it has several strategies to change element configurations and dimensions. It is feasible to establish various boundary conditions in desired coordinate systems. Action load can be static or changing with time, with permit to acting on nodes as well as element area.

To calculate mechanical properties of 3D CNT-graphene nano architectures, Sihn et al. [95] consider C-C covalent bonds as beam elements and carbon atoms as nodes to sustain external loads. There are 3 translational and 3 rotational degrees of freedom at every carbon atoms in beam element theory. FEM builds element equations [93] for elements

$$k^e u^e = f^e$$

$$u^e = \{u_i^e, u_j^e\}^T \text{ where } u_i^e = \{u_x, u_y, u_{z,} \theta_x, \theta_y, \theta_z\}_i \quad (2.19)[95]$$

$$f^e = \{f_i^e, f_j^e\}^T \text{ where } f_i^e = \{f_x, f_y, f_{z,} m_x, m_y, m_z\}_i$$

u^e : carbon atom displacement on every carbon atom (node) i and j

f^e : carbon atom force on every carbon atom (node) i and j

k^e: elemental stiffness matrix

Typical mechanical properties can be obtained as [95]:

Young's Modulus: $E_x = \frac{1}{S_{11}}$ $E_y = \frac{1}{S_{22}}$ $E_z = \frac{1}{S_{33}}$

Poisson's Ratios: $v_{yz} = \frac{S_{23}}{E_3}$ $v_{xz} = \frac{S_{13}}{E_3}$ $v_{xy} = \frac{S_{12}}{E_2}$ (2.20) [95]

Shear Modulus: $G_{yz} = \frac{1}{S_{44}}$ $G_{xz} = \frac{1}{S_{55}}$ $G_{xy} = \frac{1}{S_{66}}$

[S] is the effective compliance matrix, a 6 x 6 matrix. According to FEA calculations, it is found that CNT tube length and distance between CNTs can significantly influence effective mechanical properties of 3D CNT-graphene nano structures. Better in-plane Young's Modulus and shear modulus could be obtained through decrease of CNT tube length, while out-of-plane Modulus could be obtained through decrease of distance between CNTs.

2.5.3 First-Principles Simulation

First principles solve Schrödinger equation of electrons to get the material features without relying on empirical parameters. It is much more accurate than molecular dynamics simulations.

There is a series of Schrödinger equations for each electron [109]:

$$H\Psi_n = \left(-\frac{\hbar^2}{2m}\nabla^2 + V_{ext} + V_{eff}\right)\Psi_n = E\Psi_n \quad (2.21)$$

Ψ_n is wave founction of the electron, V_{ext} is the external potential produced by atom nuclei, V_{eff} is the effective potential which stands for total effective potential of other elections exerting on the electron, and E is the energy of the electron.

2.5.3.1 Density Functional Theory (DFT)

Density functional theory is one of the most popular and capable first principles simulation methods. In DFT, the energy of the system is determined by the functional of electron density. It significantly simplifies the calculation, since the entire computation is based on density which is much simpler than wave function. The total energy can be represented as functional of density $\rho(r)$ [109, 110]:

$$E[\rho(r)] = \int dr\, V_{ext}(r)\rho(r) + F[\rho(r)]$$

$$\rho(r) = \sum_{n=1}^{N} \Psi_n^*(r)\Psi_n(r) \quad (2.22)$$

$$F[\rho(r) = E_K[\rho(r)] + E_H[\rho(r)] + E_{xc}[\rho(r)]$$

E_K is the kinetic energy of independent electrons that produce electron density $\rho(r)$, E_H is Hartee Coulomb term, and E_{xc} is exchange-correlation functional to enable the force accurate. It is difficult to calculate the exchange-correlation functional E_{xc}, so that it is necessary to involve approximation functions to fix this problem. There are two reliable ones that are local density approximation (LDA) and generalized gradient approximation (GGA).

i) Local density approximation (LDA)

The main idea of LDA is the assumption of uniform electron gas. The approximation of exchange-correlation term E_{xc} is

$$E_{xc}^{LDA}[\rho(r)] = \int dr\rho(r)\, \varepsilon_{xc}[\rho(r)]$$

$$\varepsilon_{xc}[\rho(r)] = \varepsilon_x[\rho(r)] + \varepsilon_c[\rho(r)] \quad (2.23)$$

$$\varepsilon_x = -\frac{3}{4}\left(\frac{3\rho(r)}{\pi}\right)^{1/3}$$

Definition of ε_c has not been clearly known so far.

ii) Generalized gradient approximation (GGA).

LDA neglects changes of electron density, while generalized gradient approximation (GGA) is an advanced approximation by utilizing density gradient to improve calculation accuracy.

$$E_{xc}^{GEA}[\rho_\alpha, \rho_\beta] = \int dr\, f(\rho_\alpha, \rho_\beta, \nabla\rho_\alpha, \nabla\rho_\beta) \quad (2.24)$$

LDA and GGA are powerful to obtain precise results for a lot of materials, even though they are not accurate enough.

2.5.3.2 Density Functional Based Tight Binding (DFTB)

Although DFT is powerful and accurate for material calculation, semi-empirical methods are still needed due to large atom quantity systems. Density Functional based tight binding method is a simplified density functional theory approximated by tight binding methods, with small amounts of parameters derived from DFT computations. It can solve hundreds of atoms with relative satisfactory precision. In TB theory, the basic functions of a system including M electrons and N nuclei are Kohn-Sham equations (2.25-2.28) [111]:

$$\left[-\frac{1}{2}\nabla^2 + v_{KS}(r)\right]\Psi_i = \varepsilon_i \Psi_i \tag{2.25}$$

$$v_{KS}(r) = v_{ext}(r) + \frac{\delta j[\rho]}{\delta \rho(r)} + \frac{\delta E_{xc}[\rho]}{\delta \rho(r)} = v_{ext}(r) + \int \frac{\rho(r')}{|r-r'|} dr' + v_{xc}(r) \tag{2.26}$$

$$v_{xc}(r) = \frac{\delta E_{xc}[\rho]}{\delta \rho(r)} \tag{2.27}$$

$$\rho(r) = \sum_i^M |\Psi_i(r)|^2 \tag{2.28}$$

v_{KS} is the Kohn-Sham effective potential; Ψ_i is single particle orbitals; ε_i is the energy; v_{ext} is the external potential; v_{xc} is the exchange-correlation potential. External potential is caused by atomic nuclei and exchange correlation. ρ is the electronic density and E_{xc} represents remaining interactions including exchange-correlation contribution.

The total energy of the system (including M electrons and N nuclei) can be obtained by solving the Kohn-Sham equations. Total energy E can be expressed as [111]:

$$E[\rho] = \sum_i^M n_i < \Psi_i \left| -\frac{1}{2}\nabla^2 + v_{ext}(r) + \frac{1}{2}\int \frac{\rho(r')}{|r-r'|} dr' \right| \Psi_i > + E_{xc}[\rho] + \frac{1}{2}\sum_\beta^N \sum_{\alpha \neq \beta}^N \frac{Z_\alpha Z_\beta}{|R_\alpha - R_\beta|} \tag{2.29}$$

n_i represents occupation of a single-particle state Ψ_i.

According to DFT, total energy $E[\rho]$could be transformed into equation (2.30) [111], intending to get leading matrix elements.

$$E[\rho] = \sum_i^M n_i < \Psi_i | \hat{\mathrm{H}}_0 | \Psi_i >$$

$$-\frac{1}{2}\int\int \frac{\rho_0{}'\rho_0}{|r-r'|} dr dr' + E_{xc}[\rho_0] - \int v_{xc}[\rho_0]\,\rho_0 dr + E_{nn}$$

$$+\frac{1}{2}\int\int (\frac{\delta\rho\delta\rho'}{|r-r'|} + \frac{\delta^2 E_{xc}}{\delta\rho\delta\rho'}|_{\rho_0}) dr dr' \qquad (2.30)$$

ρ_0 is the reference electronic density; E_{nn} is ion-ion core repulsion.

Using various approximation schemes, several types of DFTB methods can be obtained, for example, standard DFTB, SCC-DFTB and Dispersion-Corrected (SCC-) DFTB.

2.5.3.2.1 Standard DFTB Model – Zeroth Order Non Self-Consistent Charge Method

When electronic-density fluctuation $\delta\rho$ is not considered-- the last term of equation (2.30) is omitted, the standard DFTB model can be obtained, which is a typical standard non-self-consistent TB scheme. The force between atoms [111] can be expressed as

$$F_\alpha = -\sum_i^M \sum_{\mu,v}^N C_{iu}\, C_{iv} \left[\frac{\partial H^0_{\mu v}}{\partial R_\alpha} - \varepsilon_i \frac{\partial S_{\mu v}}{\partial R_\alpha}\right] - \frac{\partial E_{rep}}{\partial R_\alpha} \qquad (2.31)$$

C_{iv} and $C_{i\mu}$ are expansion coefficients; $H^0_{\mu v}$ is the Hamiltonian matrix and $S_{\mu v}$ is the overlap matrix; E_{rep} is the repulsive energy.

The results of standard DFTB are accurate as SCC-DFTB when a proper reference electronic density ρ_0 is given [113]. This method is acceptable to research homo-nuclear covalent structures or highly ionic structures, in which a sum of atomic-like densities can

describe the multi-atom electron density. It has been well utilized to calculate dynamic properties and structure formations of nitrides [114], total energies and solid state modifications of carbon clusters [112], and equilibrium geometry of germanium [115].

2.5.3.2.2 Self-Consistent Charge (SCC) DFTB-Second-Order Extension

When electronic-density fluctuation $\delta\rho$ is considered, the SCC-DFTB model can be obtained. The force between atoms [111] can be expressed as

$$F_\alpha = -\sum_i^M n_i \sum_{\mu,v}^N C_{iu} C_{iv} \left[\frac{\partial H^0_{\mu v}}{\partial R_\alpha} - \left(\varepsilon_i - \frac{\partial H^1_{\mu v}}{\partial S_{\mu v}}\right)\frac{\partial S_{\mu v}}{\partial R_\alpha}\right] - \Delta q_\alpha \sum_\xi^N \frac{\partial \Upsilon_{\alpha\beta}}{\partial R_\alpha} \Delta q_\xi - \frac{\partial E_{rep}}{\partial R_\alpha} \quad (2.32)$$

SCC-DFTB considers long-range Coulomb interactions. It can calculate systems with hetero-nuclear molecules in polar semiconductors, since chemical bonds in these structures are dominated by a more sensitive charge balance between atoms [116]. In this method, system energy, force and transferability are advanced than standard DFTB results. SCC-DFTB are widely used to calculate material structure and dynamics [117], NMR spectra [118], Optical excitations [119], and so forth. More importantly, it is proved to be successful to calculate metal organic materials [120] and aluminum oxide [121]. In this dissertation, we will show the work of junction growth of 3D CNT-graphene with metal catalyst with this SCC-DFTB approach.

In addition, as calculation about DNA, protein, and peptides, dispersion force will be involved, Dispersion-Corrected (SCC-) DFTB will be suitable [111, 122].

2.6 References

[1] S. Iijima, Nature 354 (1991) 56.

[2] J. Gavillet, A. Loiseau, C. Journet, F. Willaime, F. Ducastelle, J.C. Charlier, PRL 87 (2001) 275504.

[3]. R. S. Wagner, W. C. Ellis, Appl. Phys. Lett. 4 (1964) 89.

[4].Y. Saito et al., Jpn. J. Appl. Phys. 33 (1994) 526.

[5] Y. Saito et al., CARBON 33 (1995) 979.

[6] O.M. Dunens, A.T. Harris. Ind. Eng. Chem. Res. 49 (2010) 5323.

[7] A. Zangwill, Physics at Surfaces (Cambridge UniversityPress, Cambridge, 1988).

[8] E. Bauer, J.H. van der Merwe, Phys. Rev. B 33 (1986) 3657.

[9] S.S. Coffee, J.G. Ekerdt. J. Appl. Phys. 102 (2007) 114912.

[10] A. Baskaran, P. Smereka, J.appl. Phys. 111 (2012) 044321.

[11] H. Dai, A.G. Rinzler, P. Nikolaev, A. Thess, D.T. Colbert, R.E. Smalley, Chem. Phys. Lett. 260 (1996) 471.

[12] S.B. Sinnott, R. Andrews, D. Qian, A.M. Rao, Z. Mao, E.C. Dickey, F. Derbyshire, Chem. Phys. Lett. 315 (1999) 25.

[13] V. Jourdain, C. Bichara, CARBON 58 (2013) 2.

[14] V. I. Merkulov, A.V. Melechko, M. A. Guillorn, D.H. Lowndes, M.L. Simpson, Appl. Phys. Lett. 79 (2001) 29702.

[15] M. Kumar, Carbon Nanotube Synthesis and Growth Mechanism. In: Yellampalli S, editors. Carbon Nanotubes - Synthesis, Characterization, Applications, InTech; 2011, p. 147-170. (Available from: http://www.intechopen.com/books/carbon-nanotubes-synthesis-characterization-applications/carbonnanotube-synthesis-and-growth-mechanism)

[16] C. Berger, Z. Song, X. Li, X. Wu, N. Brown, C. Naud, et al., Science 312 (2006) 1191.

[17] K.V. Emtsev, A. Bostwick, K. Horn, J. Jobst, G.L. Kellogg, L. Ley, J.L. McChesney, et al., Nat. Mater. 8 (2009) 203.

[18] C. Riedl, C. Coletti, U. Starke, J. Phys. D: Appl. Phys. 43 (2010)374009.

[19] K.S. Novoselov, A.K. Geim, S.V. Morozov, D. Jiang, Y. Zhang, S.V. Dubonos, I.V. Grigorieva, A.A. Firsov, Science 306 (2004) 666.

[20] K.S. Novoselov, A.K. Geim, S.V. Morozov, D. Jiang, M.I. Katsnelson, I.V. Grigorieva, S.V. Dubonos, A.A. Firsov, Nature 2005, 438, 197–200.

[21] B. Hu, H.A. Carlo, M. Orofeo, Y. Ogaw, M. Tsuji, New J. Chem. 36 (2012) 73.

[22] K. Yan, L. Fu, H. Peng, Z. Liu. Chem. Res. 46 (2013) 2263.

[23] P. Blake, P.D. Brimicombe, R.D. Nair, T.J. Booth, D. Jiang, F. Schedin, L.A. Ponomarenko, S.V. Morozov, H.F. Gleeson, E.W. Hill, A.K. Geim, K.S. Novoselov, Nano Lett. 8 (2008) 1704.

[24] J.B. Wu, H.A. Becerril, Z.N. Bao, Z.F. Liu, Y.S. Chen, P. Peumans, Appl. Phys. Lett. 92 (2010) 263302.

[25] T.J. Echtermeyer, M.C. Lemme, M. Baus, B.N. Szafranek, A.K. Geim, H. Kurz, IEEE Electron Device Lett. 29 (2008) 952.

[26] K.S. Kim, Y. Zhao, H. Jang, S.Y. Lee, J.M. Kim, K.S. Kim, J.H. Ahn, P.Kim, J.Y. Choi. B.H. Hong, Nature 457 (2009) 706.

[27] A.K. Geim, K.S. Novoselov, Nat. Mater. 6 (2007) 183.

[28] D.A. Dikin, S. Stankovich, E.J. Zimney, R.D. Piner, G.H.B. Dommett, G. Evmenenko, S.T. Nguyen, R.S. Ruoff, Nature 2007,448 (7152) 457.

[29] S. Gilje, S. Han, M. Wang, K.L. Wang, R.B. Kaner, Nano Lett. 7 (2007) 3394.

[30] S. Stankovich, D. A. Dikin, G.H.B. Dommett, K.M. Kohlhaas, E.J. Zimney, E.A. Stach, R.D. Piner, S.T. Nguyen, R.S. Ruoff, Nature 442 (2006) 282.

[31] S. Park, R. S. Ruoff, Nat. Nanotechnol 4 (2009) 217.

[32] H. Shioyama, J. Mater. Sci. Lett. 20 (2001) 499.

[33] L.M. Viculis, J.J. Mack, R.B. Kaner, Science 299 (2003) 1361.

[34] S. Horiuchi, et al., Appl. Phys. Lett. 84 (2004) 2403.

[35] S. Marchini, S. Gunther, J. Wintterlin, Phys. Rev. B 76 (2007) 075429.

[36] E. Loginova, N. C. Bartelt, P.J. Feibelman, K.F. McCarty, New J. Phys. 10 (2008) 093026.

[37] P.W. Sutter, J.-I. Flege, E.A. Sutter, Nat. Mater. 7 (2008) 406.

[38] Q. Yu, J. Lian, S. Siriponglert, H. Li, Y.P. Chen, S.-S Pei, Appl.Phys. Lett. 93 (2008) 113103.

[39] A. Reina, X. Jia, J. Ho, D. Nezich, H. Son, V. Bulovic, M.S. Dresselhaus, J. Kong, Nano Lett. 9 (2009) 30.

[40] K.S.Kim,; Y.Zhao,; H.Jang,; S. Y. Lee,; J. M. Kim,; K. S. Kim,; J.-H. Ahn,; P. Kim,; J.-Y.Choi,; B. H. Hong, Nature 457 (2009) 706.

[41] X.S. Li, W.W. Cai, J.H. An, S. Kim, J. Nah, D.X. Yang, R.D. Piner, A.Velamakanni, I. Jung, E. Tutuc, S.K. Banerjee, L. Colombo, R.S. Ruoff, Science 34 (2009) 1312.

[42] T. Greber, DOI: arXiv:0904.1520v1, 2009

[43] P.W. Sutter, J.-I. Flege, E.A. Sutter, Nat. Mater. 7 (2008) 406.

[44] F.J. Himpsel, K. Christmann, P. Heimann, D.E. Eastman, P.J. Feibelman, Surf. Sci. 115 (1982) L159.

[45] J. Coraux, A.T. N'Diaye, C. Busse, T. Michely, Nano Lett. 8 (2008) 565.

[46] A. Kholin, E.V. Rut'kov, A.Y. Tontegode, Sov. Phys.–Solid State 27 (1985) 155.

[47] J.C. Hamilton, J.M. Blakely, Surf. Sci. 91 (1980) 199.

[48] M. Losurdo, M.M. Giangregorio, P. Capezzuto, G. Bruno, Phys. Chem. Chem. Phys. 13 (2011) 20836.

[49] M. Eizenberg, J. M. Blakely, Surf. Sci. 82 (1979) 228.

[50] A.N. Obraztsov, E.A. Obraztsova, A.V. Tyurnina, A.A. Zolotukhin, CARBON 45 (2007) 2017.

[51] A. Reina, X. Jia, J. Ho, D. Nezich, H. Son, V. Bulovic, M.S. Dresselhaus, J. Kong, Nano Lett. 9 (2009) 30.

[52] Z.P. Hu, D.F. Ogletree, M.A. Van Hove, G.A. Somorjai, Surf. Sci. 180 (1987) 433.

[53] T.A. Land, T. Michely, R.J. Behm, J.C. Hemminger, G. Comsa, Surf. Sci. 264 (1992) 261.

[54] X. Li, W. Cai, L. Colombo, R.S. Ruoff. Nano Lett. 9 (2009) 4268.

[55] S. Bae, H. Kim, Y. Lee, X. Xu, J.-S. Park, Y. Zheng, J. Balakrishnan, T. Lei, H. Ri Kim, Y. I. Song, Y.-J. Kim,K. S. Kim, B. Ozyilmaz, J.-H. Ahn, B. H. Hong, S. Iijima, Nat. Nanotechnol. 5 (2010) 574.

[56] M.P. Levendorf, C.S. Ruiz-Vargas, S. Garg, J. Park, Nano Lett. 9 (2009) 4479.

[57] C. Mattevi, H. Kima, M. Chhowalla, J. Mater. Chem. 21 (2011) 3324.

[58] A.K. Geim, K.S. Novoselov. Nat. Mater. 6 (2007) 183.

[59] H. Huang,W. Chen, S. Chen, and A.T.S. Wee, Acs Nano 2 (2008) 2513

[60] M. Hupalo, E.H. Conrad, M.C. Tringides, Phys. Rev. B 80 (2009) 041401(R).

[61] P. sutter. How silicon leaves the scene. Nat. mater. 8 (2009) 171.

[62] M.L. Bolen, S.E. Harrison, L.B. Biedermann, M.A. Capano. Phys. Rev. B 80 (2009) 115433.

[63] D.V. Badami, Nature 193 (1962) 570.

[64] C. Berger, et al., J. Phys. Chem. B 108 (2004) 19912.

[65] Z. Fan, J. Yan, L. Zhi, Q. Zhang, T. Wei, J. Feng, M. Zhang, W. Qian, F. Wei, Adv. Mater. 22 (2010). 3723.

[66] T.K. Hong, D.W Lee, H.J. Choi, H.S., Shin, B. S. Kim, ACS Nano 4 (2010) 3861.

[67] H.R. Byon, S.W. Lee, S. Chen, P.T. Hammond, Y. Shao-Horn, Carbon 49 (2011) 457.

[68] Y. Liu, Y. Liu, H. Feng, Y. Wu, L. Joshi, X. Zeng, J. Li, Biosens. Bioelectron. 35 (2012) 63.

[69] D.S. Yu, L.M. Dai, J. Phys. Chem. Lett. 1 (2010) 467.

[70] L.W. Peng, Y.Y. Feng, P. Lv, D. Lei, Y.T. Shen, Y. Li, W. Feng, J. Phys. Chem. C, 116 (2012) 4970.

[71] J.J. Shao, W. Lv, Q.G. Guo, C. Zhang, Q. Xu, Q.H. Yang, F.Y. Kang, Chem. Commun. 48 (2012) 3706.

[72] J.F. Shen, Y.Z. Hu, C. Li, C. Qin, M. Shi, M.X. Ye, Langmuir 25 (2009) 6122.

[73] B.S. Kong, J.X. Geng, H.T. Jung, Chem. Commun. 16 (2009) 2174.

[74] Y.K. Kim, D.H Min, Langmuir 25 (2009) 11302.

[75] K. Yu, G. Lu, Z. Bo, S. Mao, J. Chen, J. Phys. Chem. Lett. 2 (2011) 1556.

[76] D.H. Lee, J.E. Kim, T.H. Han, J.W. Hwang, S. Jeon, S.Y. Choi, S.H. Hong, W.J. Lee, R.S. Ruoff, S.O. Kim, Adv. Mater. 22 (2010) 1247.

[77] X. Dong, Y. Ma, G. Zhu, Y. Huang, J. Wang, M.B. Chan-Park, L. Wang, W. Huang, P.J. Chen, Mater. Chem. 22 (2012) 17044.

[78] S.-H. Bae, K. Karthikeyan, Y.-S. Lee, Il-K. Oh, CARBON 64 (2013) 527.

[79] J. Wen, Y. Li, W. Yang, Vacuum 101 (2014) 271.

[80] Y. Zhu, L. Li, C. Zhang, G. Casillas, Z. Sun, Z. Yan, G. Ruan, Z. Peng, A.R.O. Raji, C. Kittrell, R.H. Hauge, J. M.Tour, Nature commu. 3 (2012) 1225.

[81] Z. Yan, L. Ma, Y. Zhu, I. Lahiri, M.G. Hahm, Z. Liu, S. Yang, C. Xiang, W. Lu, Z. Peng, Z. Sun, C. Kittrell, J. Lou, W. Choi, P.M. Ajayan, J.M. Tour, Acs Nano 7 (2013) 58.

[82] J. Lin, C. Zhang, Z. Yan, Y. Zhu, Z. Peng, R.H. Hauge, D. Natelson, J.M. Tour, Nano Lett. 13 (2013) 72.

[83] M. Zhao, Q. Zhang, J. Huang, G. Tian, T. Chen, W. Qian, F Wei. CARBON 54 (2013) 403.

[84] M.Q. Zhao, X.F. Liu, Q. Zhang, G.L. Tian, J.Q. Huang, W. Zhu, F. Wei, ACS NANO 6 (2012)10759.

[85] F. Du, D. Yu, L. Dai, S. Ganguli, V. Varshney, A.K. Roy, Chem. Mater. 23 (2011) 4810.

[86] C. Kang, R. Baskaran, J. Hwang, B. Ku, W. Choi. CARBON 68 (2014) 493.

[87] D. Baowan, B.J. Cox, J.M. Hill. CARBON 45 (2007) 2972.

[88] Y.F. Li, B.R. Li, H.L. Zhang. Nanotechnology, 20 (2009) 225202.

[89] B.J. Cox, J.M. Hill, J. Phys. A: Math. Theor. 41(2008) 125203.

[90] Y. Mao, J. Zhong, New Journal of Physics 11 (2009) 093002.

[91] L. Xu, N. Wei, Y. Zheng, Z. Fan, H.-Q. Wang, J.-C. Zheng, J. Mater. Chem. 22 (2012) 1435.

[92] F.D. Novaes, R, Rurali, P. Ordejo, ACS NANO 4 (2010) 7596.

[93] S. Sihn, V. Varshney, A.K. Roy, 51st AIAA/ASME/ASCE/AHS/ASC Structures, Structural Dynamics, and Materials Conference
18th 12 - 15 April 2010, Orlando, Florida/

[94] V. Varshney, S.S. Patnaik, A.K. Roy, G. Froudakis, B.L. Farmer, ACS NANO 4 (2010) 1153.

[95] S. Sihn, V. Varshney, A.K. Roy, B.L. Farmer, CARBON 50 (2012) 603.

[96] J. Park, V. Prakash, J. Mater. Res. 28 (2013) 940.

[97] R.P. Wesołowski, A.P. Terzyk, Phys. Chem. Chem. Phys. 13(2011) 17027.

[98] G.K. Dimitrakakis, E. Tylianakis, G. E. Froudakis, Nano Lett. 8 (2008) 3166.

[99] G.C. Loh, E.H.T. Teo, B.K. Tay, J. Appl. Phys. 110 (2011) 083502.

[100] D. Kondo, S. Sato, Y. Awano, Appl. Phys. Express 1 (2008) 074003.

[101] R.K. Paul, M. Ghazinejad, M.Penchev, J. Lin, M. Ozkan, C.S. Ozkan, Small 6 (2010) 2309.

[102] L. Zhang, J. Niu, L. Dai, Z. Xia, Langmuir 28 (2012) 7542.

[103] D.J. Evans, G.P. Morriss, Statistical Mechanics of Nonequilibrium Liquids (Academic, London, 1990).

[104] H.J.C. Berendsen, in Computer Simulation in Materials Science, edited by M. Meyer and V. Pontikis (Kluwer, Dordrecht, 1991)

[105] R. Vogelsang, C. Hoheisel, M. Luckas, Mol. Phys. 64 (1988) 1203.

[106] Wm.G. Hoover, C.G. Hoover. Condensed Matter Phys. 8 (2005) 247.

[107] Wm.G. Hoover, J. Chem. Phys, 109 (1998) 4164.

[108] F. Müller-Plathe, P. Bordat, Lect. Notes Phys. 640 (2004) 310.

[109] M.D. Segall, P.J.D. Lindan, M.J. Probert, C.J. Pickard, P.J. Hasnip, S.J. Clark, M.C. Payne, J. Phys.: Condens. Matter 14 (2002) 2717.

[110] The 1998 Nobel Prize in chemistry: http://www.nobel.se/chemistry/laureates/1998/

[111] A. F. Oliveira, G. Seifert, T. Heinec, H.A. Duarte, J. Braz. Chem. Soc. 20 (2009) 1193.

[112] D. Porezag, Th. Frauenheim, Th. Ko¨hler, G. Seifert, R. Kaschner, Phys. Rev. B 51 (1995) 12947.

[113] M. Elstner, D. Porezag, G. Jungnickel, J. Elsner, M. Haugk, Th. Frauenheim, S. Suhai, G. Seifert, Phys. Rev. B 58 (1998) 7260.

[114] J. Widany, F. Weich, Th. Kijhler, D. Porezag, Th. Frauenheim, Diamond and Related Materials 5 (1996) 1031.

[115] P. Sitch, Th. Frauenheim, R. Jones, J. Phys.: Condens. Matter. 8 (1996) 6873.

[116] Th. Frauenheim, G. Seifert, M. Elstner, Z. Hajnal,G. Jungnickel, D. Porezag, S. Suhai, and R. Scholz. Phys. Stat. Sol. (b) 217 (2000) 41.

[117] T. Heine, H.F.D. Santos, S. Patchkovskii, H.A. Duarte, J. Phys. Chem. A 111 (2007) 5648–5654.

[118] T. Heine, G. Seifert, P.W. Fowler, F. Zerbetto, J. Phys. Chem. A, 103 (1999) 8738.

[119] J.Frenzel, J.O. Joswig, G. Seifert, J. Phys. Chem. C 111 (2007) 10761.

[120] A. Kuc, A. Enyashin, G. Seifert, J. Phys. Chem. B 111 (2007) 8179.

[121] R. Luschtinetz, A.F. Oliveira, J. Frenzel, J.O. Joswig, G. Seifert, H.A. Duarte, Surf. Sci. 602 (2008) 1347.

[122] M. Elstner, Theor. Chem. Acc. 116 (2006) 316.

[123] G. Alfano, M.A. Crisfield, Int. J. Numer. Meth. Engng. 50 (2001)1701.

[124] Z. Xia, T. Sujidkul, J. Niu, C.E. Smith, G.N. Morscher, Composites Part A 43 (2012) 1730.

[125] G. Comini, S.D. Guidice, R.W. Lewis, O.C. Zienkiewicz, Int. J. Numer. Meth. Engng. 8 (1974) 613.

[126] S.H. Zhang, K.B. Nielsen, J. Danckert, D.C. Kang, L.H. Lang, J. Mater. Process. Technol. 102 (2000) 1.

[127] C.C. Mcintyre, W.M. Grill, Ann. Biomed. Eng. 29 (2001) 227.

CHAPTER 3

GROWTH OF JUNCTIONS IN 3D CARBON NANOTUBE-GRAPHENE NANOSTRUCTURES: A QUANTUM MECHANICAL MOLECULAR DYNAMIC STUDY

3.1 Introduction

Owing to their unique mechanical [1, 2], electrical [3, 4] and thermal [5, 6] properties, carbon nanomaterials such as carbon nanotubes (CNTs) and graphene have attracted considerable interest for a wide range of potential applications. The one-dimensional (1D) and two-dimensional (2D) graphene sheets are considered as ideal 'building blocks' for the bottom-up strategy by combining them to create three-dimensional (3D) nano networks. Recent theoretical studies predicted that the 3D pillared CNT-graphene network nanostructures possesses desirable out-of-plane properties [7-10] while maintaining in-plane properties, attractive for numerous innovative applications, including new efficient electrodes for fuel cells [11], nanoporous structures for hydrogen storage [12] and supercapacitors [13], tailored orthogonal thermal transport materials [14], and building blocks for nano/microscale integrated devices [15-16]. For these applications, covalently-bonded junctions, especially seamless C-C covalently bonded junctions, are needed to enhance the mechanical properties and stability, and thermal electrical transport.

A few of experimental approaches have been developed to fabricate the 3D nanostructures with the covalently-bonded junctions. For instance, Du et al. demonstrated a 3D structure consisting of several layers of graphene with CNTs grown on them perpendicularly [15]. Zhu et al. developed a method to bond graphene and single-walled carbon nanotubes carpet [17, 18]. Because of process and structural complexity, however, the growth mechanism and detailed structures of the CNT-graphene junctions in these 3D nanostructures have not been

clearly revealed and it remains controversial if the junctions are covalent C-C bonds. Experimental observation of the junction growth in these 3D structures remains a significant challenge because the CNT growth is very fast with over 10-μm long nanotubes in seconds [19]. Therefore, fundamental understanding of the junction growth mechanism could provide unique information and useful design guidelines for materials and process development towards these and other novel 3D carbon nanostructures.

Molecular dynamics (MD) are powerful tools that can gain new insights into growth mechanism as well as structures of nanomaterials. These methods have been widely used to study the growth mechanisms and nanomechanical behavior of carbon nanotubes [20-23]. The pioneering MD investigations in this area relied on the reactive empirical bond order (REBO) force field [24-27]. The use of this force-field makes MD simulations on nanosecond timescales possible. Nevertheless, the REBO potentials cannot accurately describe the chemistry of CNT nucleation, including *p*-conjugation and aromatic stabilization of carbon (central to the formation and extension of an sp^2-hybridised carbon network, such as a CNT), charge transfer effects and the near-degeneracy of transition metal *d*-orbitals (crucial in the case of transition metal catalysts) [31]. In this chapter, the growth of a carbon nanotube on a graphene sheet with Fe nanoparticles as catalyst was simulated by quantum mechanical molecular dynamics (QM/MD) methods. This type of method has the advantage of providing classical molecular dynamics features and quantum mechanical accuracy. We found that the junction with covalent C-C bonds could be formed at the junction during the CNT growth on graphene. Pure covalent C-C bonds could be generated by moving the catalyst during the CNT growth or post treatment. Our simulation thus provides a novel approach for design and process of carbon-based 3D nanostructures with seamless C-C junctions.

3.2 Computational Methodology

SCC-DFTB+ (self-consistent-charge Density Functional Tight Binding) [28] code was employed to simulate the growth of CNT-graphene junction in the presence of iron catalysts. The method has been approved to be successful to simulate the CNT growth with catalyst [29-34]. The atomic motion was propagated using velocity Verlet dynamics with Nose Hoover thermostat [28]. The simulation was performed at a temperature of T=1400K with a timestep of 1 fs, and the finite electronic temperature [35-37] was controlled at 0.05Ha. The operation temperature was determined according to laboratory reports [38]. The electronic temperature allows fractional occupancies for molecular orbitals and takes into account the near-degeneracy of transition metal *d*-orbitals, which is essential in this growth mechanism.

3.2.1 Junction Growth with a Carbon Nanotube Precursor

The model consists of a piece of preformed graphene of 1.98 nm x 2.0 nm, in the center of which, a hole of 1.1 nm x 1.2 nm was drilled and an iron nanoparticle of 0.57 nm x 0.57 nm x 0.57 nm was then filled into the hole. The system was heated at 1127 ^{o}C and fully relaxed at the temperature with a time step of 1fs before CNT growth (**Fig. 3.1**). Carbon source of C_2 was then inserted into the system with reasonable energies. C_2 has been proved to be the appropriate carbon source in carbon nanotube growth by simulations [40]. It was observed that most of the C_2 were absorbed onto the iron nanoparticle and C-Fe bonds formed upon touch. As soon as the iron particle was covered by the carbon atoms, a carbon nanotube precursor (0.618 nm length and 4.0 nm diameter) was introduced to speed up the junction growth between CNT and graphene. In the simulation, the C_2 source was kept to flow into the system for about 50 ps with

the timestep of 1 fs. In the end of the simulation, the number of added carbon atoms was about 300.

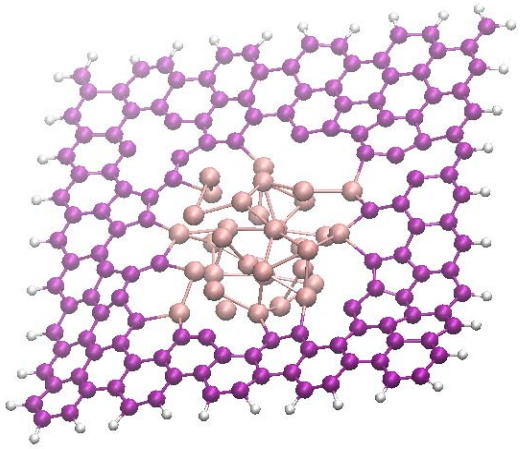

Fig. 3.1 Graphene with an iron nanoparticle relaxed at a growth temperature before carbon source was added. (Purple, pink, black, and blue balls refer to graphene, iron particle, added carbon source, CNT precursor, and hydrogen atoms to stabilize the system)

3.2.2 Junction Growth without Carbon Nanotube Precursor

The simulation model consists of an iron nanoparticle embedded in a single graphene sheet, as shown in **Fig. 3.2**. The model was constructed with a piece of hexagonal graphene (edge length of 1.4~ 1.8 nm） with a hole of 1.13 nm x1.23 nm, drilled in the center. The outlining boundaries of the graphene were saturated by hydrogen atoms. An iron particle of 0.86 nm x 0.86 nm x 0.86 nm was inserted into the hole. The whole model contains 244 carbon atoms and 44 hydrogen atoms in the graphene, 91 iron atoms in the iron particle and 460 carbon atoms added during simulation. To our knowledge, the number of atoms used in the simulation is record high (totally over 800) compared to reported simulations using the similar methods. The system was relaxed at the process temperature for 2 ps. After relaxation, the iron particle became spherical shape (diameter d ~1 nm) with Fe-C bonds formed between the particle and graphene edge. The size of the iron particle is close to those catalysts used in the experiment [17]. To

simulate nanotube growth, carbon source (C_2) was continuously injected into the system from an arbitrary position but toward the center of the graphene/particle, with an average supplying rate of 12 C atoms/ps. The magnitude of the incident energy of the supplied carbon atom was set to 0.13 eV, which corresponds to the kinetic energy equivalent to the atomic nuclear temperature of 1400K [39]. C_2 has been proved to perform better than the single carbon atoms in the catalytic CNT growth [39].

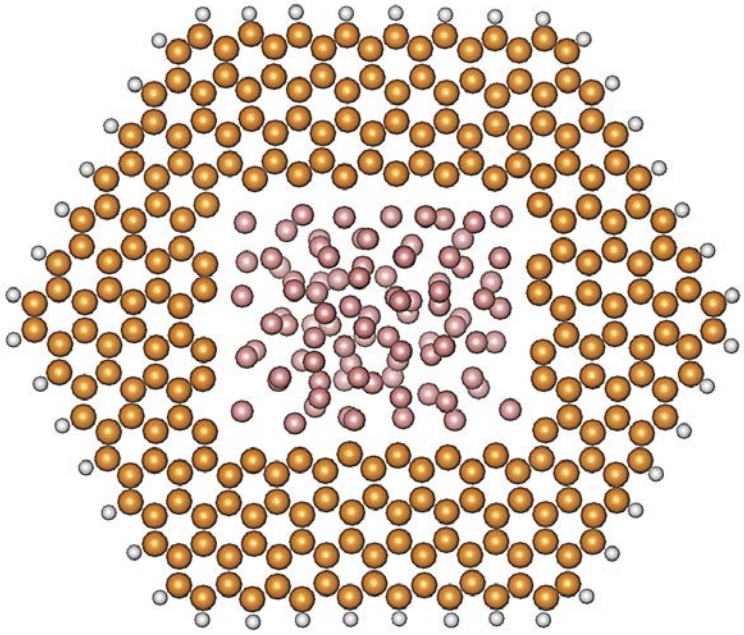

(a)

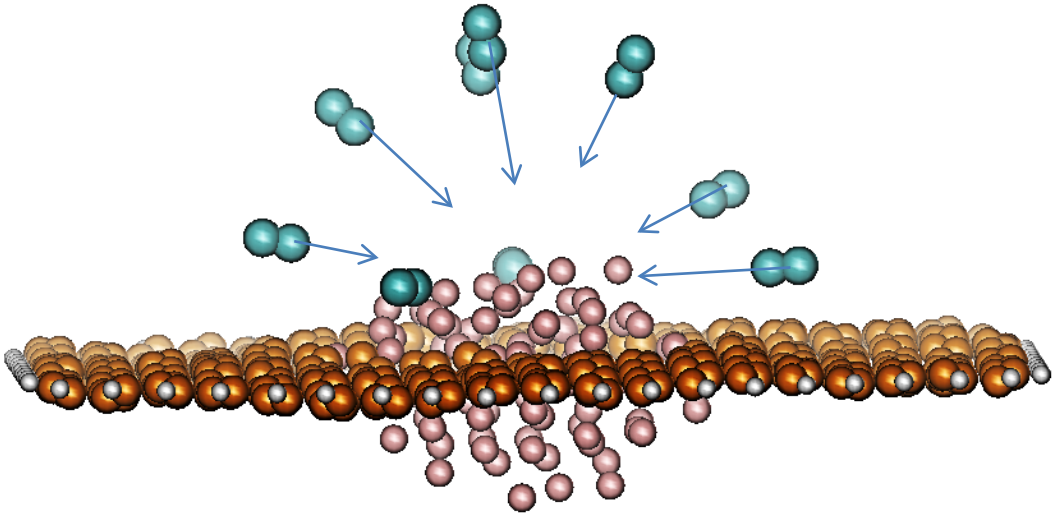

(b)

Fig. 3.2 Optimized geometric structure—the hexagonal graphene (orange) was saturated by hydrogen atoms (white) and the iron catalyst (pink) sits in the central hole of the graphene. (a) Top view; (b) side view showing the way how C_2 (green) was supplied.

3.3 Results and Discussion

3.3.1 Mechanism of Junction Growth with A CNT Precursor

It was showed in the simulation that the iron nanoparticle was gradually embraced by the added carbon atoms in the forms of hexagons and pentagons which connect graphene and carbon nanotube to form a carbon-based junction although many defects exist in the junction (**Fig. 3.3**). As a result, the Fe particle was trapped in the graphene/CNT junction and the CNT continuously grew as the carbon source was added into the system. It is of interest to note that the graphene and CNT were directly connected at their interface by covalent carbon bond. Even if the catalytic particle is removed by e.g. chemical etching, the junction can keep intact. Compared with the graphene/CNT interface maintained by the van der Waals force, this type of covalently-bonded

junctions is expected to have much better mechanical, thermal and electrical properties for various applications.

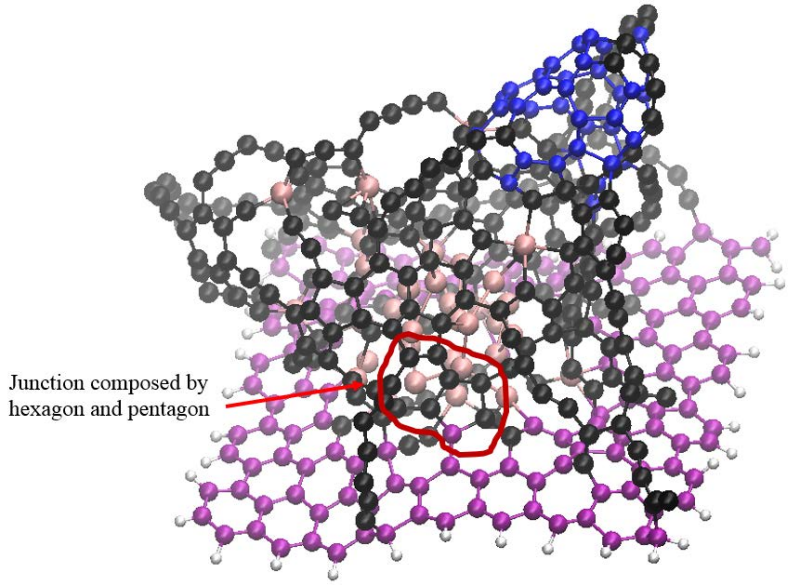

Fig. 3.3 The formation of graphene/CNT heterojunction. The CNT and graphene was connected by C-C bond, and the catalytic particle was trapped at the junction (Purple, pink, black, and blue balls refer to graphene, iron particle, added carbon source, CNT precursor, and hydrogen atoms to stabilize the system)

3.3.2 Mechanism of Junction Growth without CNT precursor

We simulated the process of carbon nanotube growth and the junction formation between the graphene and the newly-grown carbon nanotube. In the initial stage of the growth process, short polyyne chains gradually formed and branched on the surface of the iron particle as carbon source was continuously fed into the system, as shown in **Fig. 3.4** (a). As more chains form, they tend to connect to each other. Eventually, an embryo polygon (hexagon in this case) was born from these carbon chain clusters (**Fig. 3.4** (b)). Once the first polygon formed, other polygons quickly emerged along the edges of this polygon. The incident carbon atoms subsist on the iron nanoparticle as polygons were apt to encircle the catalyst to form a carbon nanotube. As carbon

nanotube grows, C-C covalent bonds between the graphene and growing carbon nanotube eventually formed at the edge of the graphene (**Fig. 3.4** (c)).

Fig. 3.5 shows the population of different polygons versus time. Pentagons, hexagons and heptagons were the major structures of the CNT wall throughout the CNT growing process. The first polygon—hexagon emerged at 11.5 ps. After 15 ps, the number of pentagons exceeds that of hexagons, indicating that the depositing carbon prefers to form pentagons first. While the number of pentagons and hexagons kept growing, the number of heptagons is relatively small and nearly constant after formation of the nanotube. We also observed octagons in the simulation but they quickly disappeared, indicating that it is a temporal form of growing species. In addition to the octagons, short polyyne chains also appear as important intermediate structures, facilitating growth [39, 40]. Therefore, the pentagons were a majority of the polygons during the growth. However, the number of pentagon as defects rapidly reduced once the carbon supply was down or during annealing.

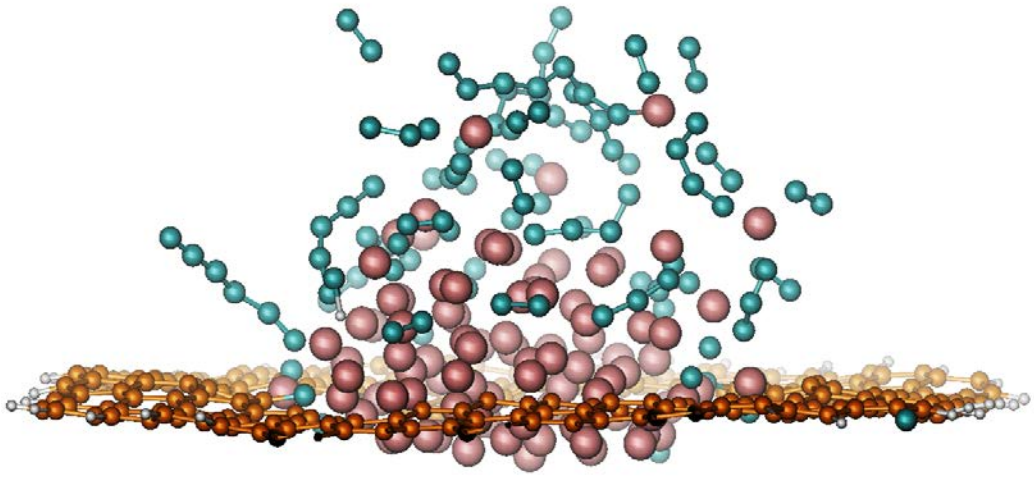

(a)

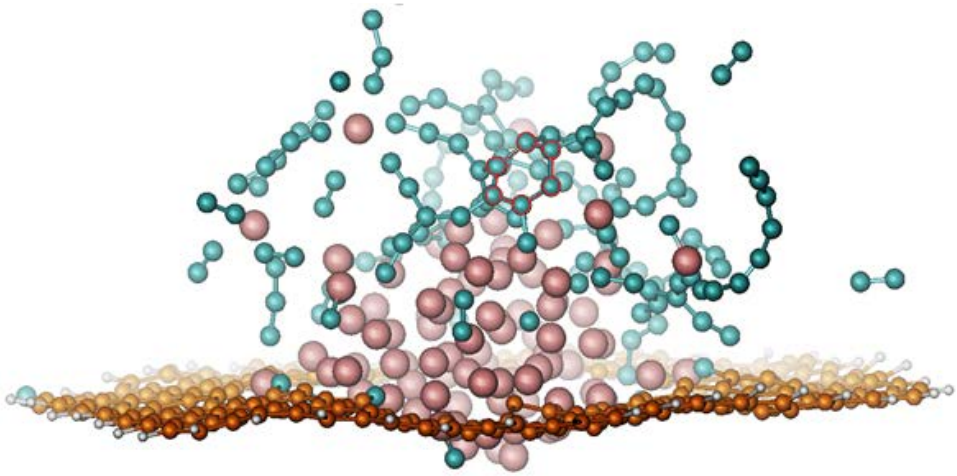

(b)

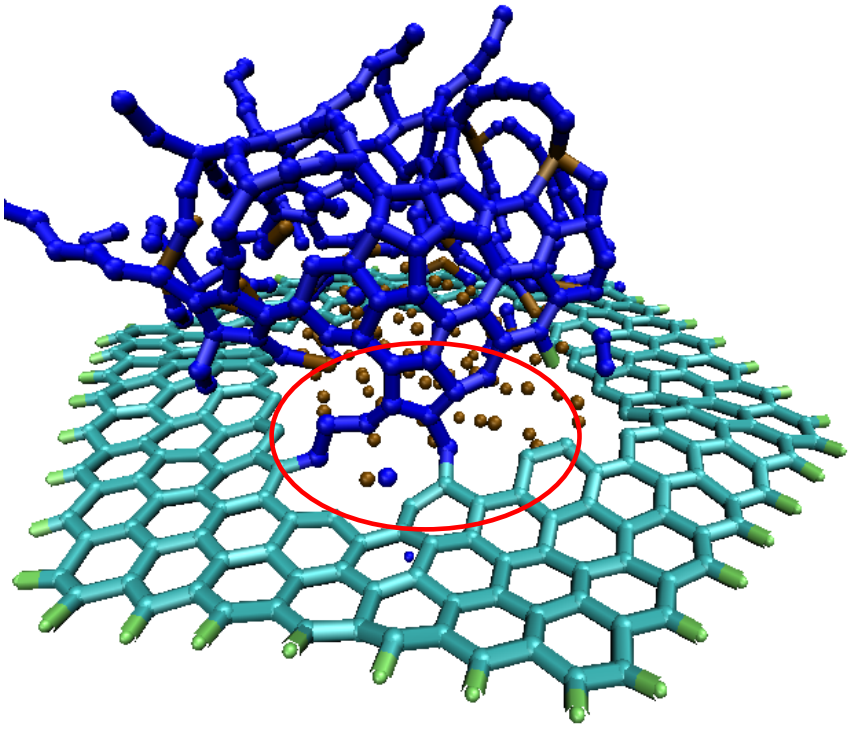

(c)

Fig. 3.4 Snapshots of CNT-graphene junction at different stages: (a) Carbon chains with brunching formed as the C2 injected in the system, (b) The first polygon (hexagon) formed from polyyne chains, and (c) The first C-C covalent bond formed after nanotube grew from the particle. Pentagons, hexagons and heptagons could be observed in the carbon network. The

structure of the iron nanoparticle fluctuated dramatically compared to early stage of growth. The catalyst moved out of the graphene hole shown in (c).

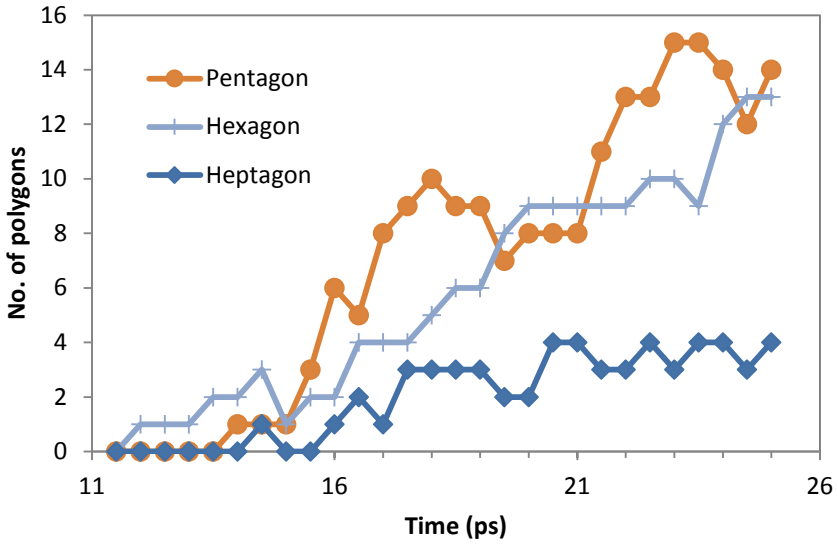

Fig. 3.5 The numbers of polygons (pentagons, hexagons and heptagons) as a function of simulation time.

While carbon atoms were configuring to polygons, some injected carbon atoms attached onto the dangling bonds on the edge of the graphene. Pure C-C covalent bonds were therefore formed between the graphene and the CNT. The existence of dangling bonds seemed crucial to the C-C junction formation since the Fe particle was confined in the graphene and strongly bonds to the graphene edge. Although the hole on the graphene could produce large number of dangling bonds, many of them have been saturated with the iron atoms. Consequently, the growing carbon nanotube could connect to the graphene through the Fe-C and C-C covalent bonds (**Fig. 3.4** (c)).

It is worthwhile noting that the shape and position of the iron nanoparticle change drastically during the simulation, as shown in **Fig. 3.1** (b) and **3.2** (c). The catalyst moved toward the CNT growing direction perpendicular to the graphene basal plane, but it was still hold by the graphene at the time the simulation ceased. Some iron atoms also departed from the mother

particle and moved with the growing CNT. Nevertheless, the iron particle still kept its spherical shape and all the atoms moved together. We have examined the iron structures during the CNT growth by calculating the Fe-Fe radical distribution function (RDF) (**Fig. 3.6**). The RDF of the nanoparticle was similar to those for liquid iron structures, indicating that the nanoparticle was in liquid state throughout junction growth.

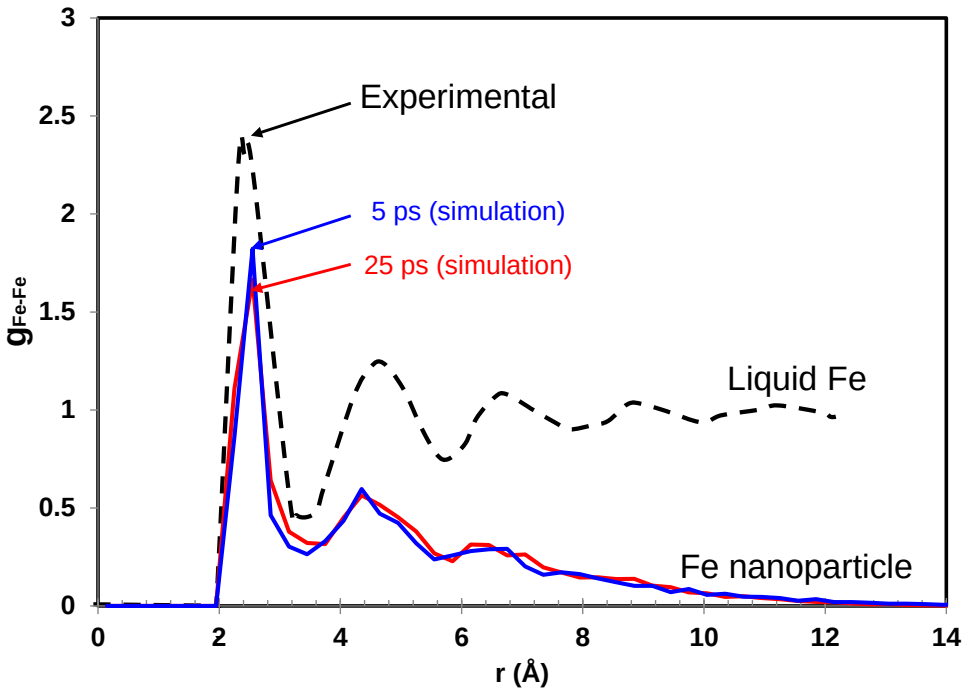

Fig. 3.6 Calculated radical distribution function of nanoparticle during the junction growth, compared to the experimental results for liquid iron at a temperature of 1800 ^{o}C [42].

To explore the details how the incident carbon atoms interacted with the catalyst and graphene sheet, we examined the bond types and their evolution during the CNT growth. **Fig. 3.7** shows the number of Fe-C and *sp* bonds as a function of the growing time. Before the C_2 was supplied, there were Fe-C bonds between the iron particle and graphene. As the C_2 was injected into the system, the number of Fe-C bonds slowly increased but reduced to its initial level as polygons started to form. Thus, early incident carbon atoms deposited on the iron nanoparticle

do create new Fe-C bonds and existed in the form of iron carbides on the surface of the iron particle. Once sp^2 bonds appeared, some Fe-C bonds were broken to form more stable nanotube structure. The increase in sp^2 bond number indicated the formation of embryonic polygons and growth of nanotube. The sp^3 bonds were observed after the nanotube formation but the population was rare in the CNT growth. It is well known that two growing mechanisms may occur when carbon nanotubes grow from nanoparticles [41]. One is the so-called "tip-growth", which occurs when the catalyst bonds to substrate loosely. In this growth mechanism, the catalyst is picked up by the newly grown CNT tip and move with the CNT growing tip. On the other hand, the "base-growth" takes places when the catalyst bonds to substrate strongly. In this case, the saturated carbon atoms expel out from the top face of the catalyst particle in the CNT form, and the catalyst is left on the substrate at the CNT base. Our simulation results indicate that the bond between the graphene and iron particle is strong and the number of Fe-C bonds maintain the same (**Fig. 3.7**). As a result, the CNT formation in this particular case is via a base-growth mode.

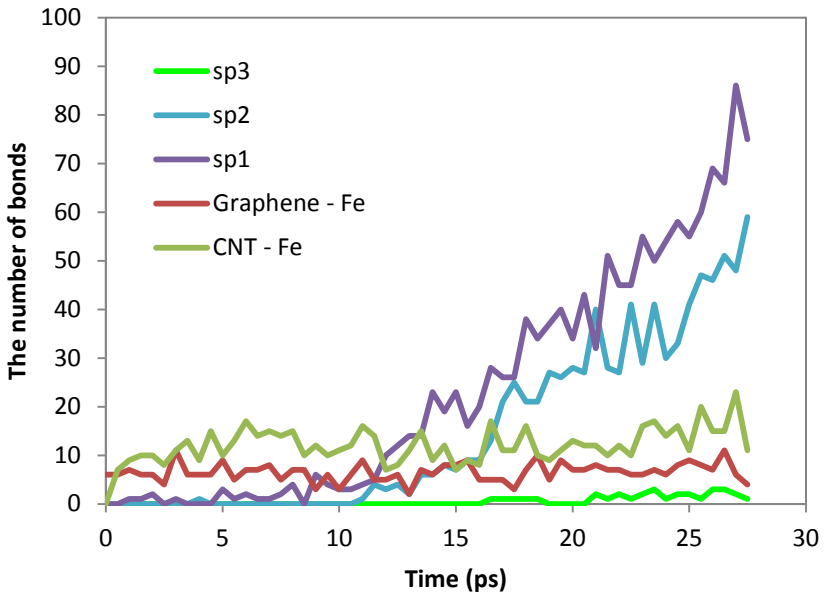

Fig. 3.7 The number of Fe-C, sp^1, sp^2 and sp^3 bonds versus simulation time.

3.3.3 Formation of Metal-Free C-C Covalently Bonded Junction between CNT and Graphene

As discussed above, the CNT-graphene junction is a crucial to determine the mechanical and transport properties of the 3D pillared CNT-graphene structures. It is highly desirable to have junctions made of pure C-C covalent bonds for many applications; though the abovementioned mixed Fe-C/C-C bond junctions could have certain advantages for some specific applications. Although the iron particle bonded strongly to the graphene substrate, it does have a strong tendency to move with the CNT cage, as observed in the simulation (**Fig. 3.4** (c)). If the Fe-C bonds between the graphene and particle are sufficiently weak and can be broken, the iron particle could then move with the CNT cage to generate seamless C-C covalently bonded junctions. In view of this possibility, we explore two avenues to produce C-C bonded junctions *via* QM/MD simulation.

3.3.3.1 Pure C-C Bonds by Lifting the Catalysts

To transform the base-growth mode to tip-growth mode, we gradually lifted the iron particle at the velocity of 0.05 nm/ps by a "force" applied on the iron nanoparticle after the CNT cage emerged in 27.5 ps, as schematically show in **Fig. 3.8**. This mimicks the move of catalyst with CNT tip during the tip growth. **Fig. 3.9** shows the corresponding structural change of the growing CNT. After about 3 ps since lifting, the first hexagon junction formed as highlighted in red circle in **Fig. 3.9** (a). Thereafter, C-C bonds contunued to form while the existing Fe-C bonds were broken during the lifting. Eventually, a pure C-C bonded junction was formed (**Fig. 3.9** (b)). Since the "force" could be induced by various procedures, such as adhesion, carrier gas flowing, and electromagnetic fields, a seamless covalently C-C bonded junction could be formed by various approaches.

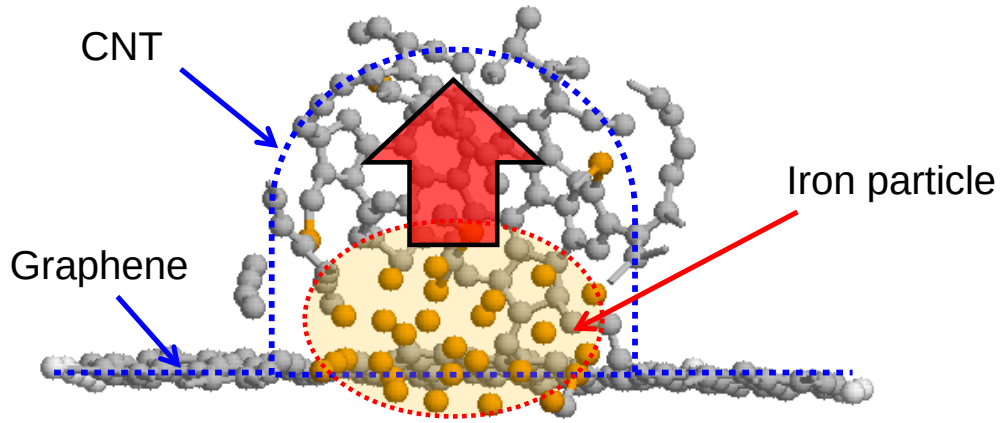

Fig. 3.8 schematics of growth mode transformation from base-growth to top-growth modes through moving the catalysts with CNT cage by "force".

Zhu *et al.* provided an excellent example of producing seamless covalently C-C bonded junction using adhesion force [17]. In their experiment, Fe nanoparticles were first deposited on the pre-grown graphene plane. An Al_2O_3 thin film was then deposited on the Fe nanoparticles. When carbon source was introduced, an aligned single-wall CNT array grew from the Fe nanoparticles by lifting the Al_2O_3 layer and producing a seamless C-C covalent bonded junction between CNT and graphene. The use of Al_2O_3 layer is critical in this process since the Fe particles adhered to the Al_2O_3 layer more strongly than to the graphene layer. Along with this particular study reported by Zhu *et al.* [17]. the Fe particles were picked up by the Al_2O_3 film during the CNT growth. Our simulation shows a more general way to produce seamlessly C-C bonded junction between CNT and graphene.

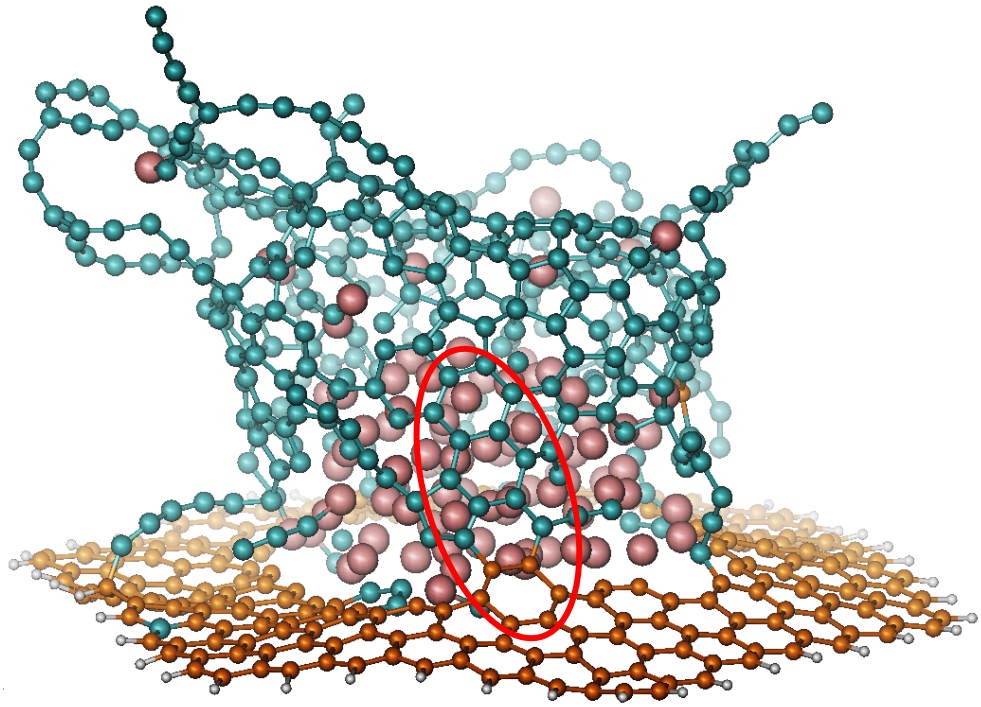

(a)

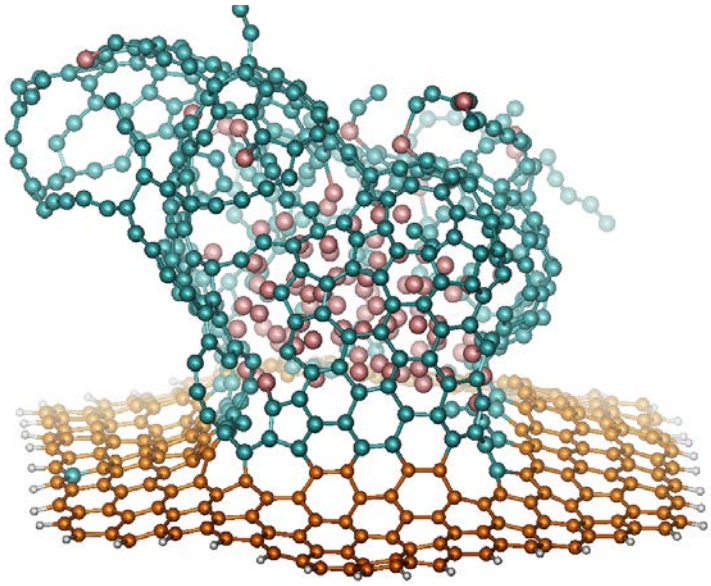

(b)

Fig. 3.9 Formation of C-C covalently-bonded junction between graphene and growing CNT in the lifting procedure: (a) the first hexagon junction formed at 3 ps, as highlighted in red color, and (b) fully C-C bonded junction formed at 11 ps.

3.3.3.2 Pure C-C Bonds By Etching and Annealing

As indicated by our QM/MD simulation, the C-C bonded junction can also be produced by removing the iron nanocatalysts with physical or chemical methods. It has been experimentally demonstrated that the iron catalysts could be removed by chemical etching from preformed graphene-supported nanotubes [38]. In Zhao's work [38], the iron nanoparticles were completely etched in acidic and alkali aqueous solutions after 3D graphene-CNT structures were synthesized. However, it is unclear in this case whether the connection between the graphene and grown CNT is C-C bond or just physical contact through the outermost graphene layer observed at the end of the single-walled CNTs.

We simulated the C-C bond formation after the iron nanoparticle was removed. **Fig. 3.10** shows the simulated nanostructures during annealing. As shown in **Fig. 3.10** (a), the bonds between carbon atoms and iron atoms broke up due to the removal of the catalyst with some dangling bonds on graphene and CNT clearly seen at the beginning of annealing. Interestingly, the gap between the CNT and the graphene were gradually sealed with annealing even at room temperature. At around 2 ps, the first pentagon and octagon appeared (**Fig. 3.10** (b)). Up to 6 ps, the gap between the two parts was attached by carbon pentagon, hexagon, heptagon and octagon (**Fig. 3.10** (c)). Thus, our DFTB simulations provide theoretical evidence for the C-C bonded junction formation, which is almost impossible to observe in the laboratory with the limitation of currently-available experimental tools, but hope to be realized in the near future.

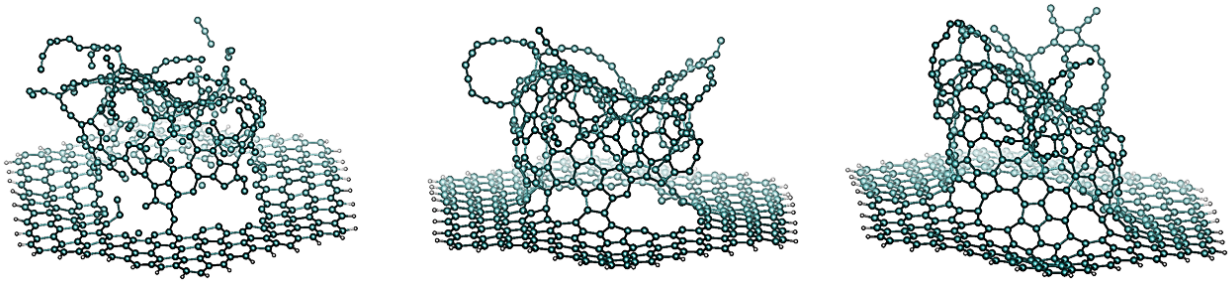

(a) (b) (c)

Fig. 3.10 C-C bonded junction formation during annealing at room temperature after the catalyst particle was removed from the structure. (a) Bond structure after the removal of the catalyst, some dangling bonds on graphene and cage left at 0 ps, (b) the first hexagon formed at 2 ps, and (c) fully C-C bonded junction formed at 6.6 ps.

3.4 Conclusions

Junction growth of CNT and graphene with CNT precursor and iron catalyst was simulated via QM/MD method. Pre-exist CNT grew longer when carbon source was injected into system and covalent C-C bond junction formed between CNT and graphene.

Vertical CNT growth on a graphene substrate with iron nanoparticles as catalyst and without CNT precursor was simulated *via* the QM/MD method. In consistence with the experimental observations on the CNT growth on graphene, our simulation indicated that the CNT growth was characterized by several stages: in the early stage, short polyyne chains appeared and brunched on the surface of the catalyst, followed by the polygons (pentagons, hexagons and heptagons) growth, and CNT cage formation and growth in a “base-growth” mode. The junction between CNT and graphene are formed with a mixture of C-C and Fe-C bonds. The catalyst has a strong tendency to move with the growing CNT cage, which facilitated the C-C bonded junction formation.

Furthermore, our simulation pointed out two avenues to produce C-C covalently bonded junctions for the 3D nanostructures. Seamlessly C-C bonded junctions could be produced by: (i)

lifting up the catalysts during CNT growth by transforming the CNT growth from “base-growth mode” to “tip-growth mode” with force, and (ii) etching and annealing after the CNT growth to remove iron nanoparticles, leading to the release of carbon dangling bonds at graphene edge from strong Fe-C bonds to form C-C bonds even at relatively low temperature.

3.5 References

[1] J.P. Salvetat, J.M. Bonar, N.H. Thomson, A. Kulik, J. Forro, W. Benoit, L. Zuppiroli, Appl. Phys. A 63 (1999) 255.

[2] R. Faccio, P.A. Denis, H. Pardo, C. Goyenola, A.W. Mombru, J Phys: Condens Matter. 21 (2009) 285304.

[3] Z. Ounaies, C. Park, K.E. Wise, E.J. Siochi, J.S. Harrison, Compos. Sci. Technol. 63 (2003) 1637.

[4] Z. Chen, Y.M. Lin, M.J. Rooks, P. Avouris, Physica E 40 (2007) 228.

[5] R.S. Ruoff, D.C. Lorents, Carbon, 33 (1995) 925.

[6] A.A. Balandin, S. Ghosh, W. Bao, I. Calizo, D. Teweldebrhan, F. Miao, et al., Nano Lett. 8 (2008) 902.

[7] F.D. Novaes, R. Rurali, P. Ordejon, ACS NANO 4 (2010) 7596.

[8] Y. Kim, K. Kumar, F.T. Fisher, E. Yang, Nanotechnology 23 (2012) 015301.

[9] L. Xu, N. Wei, Y. Zheng, Z. Fan, H. Wang, J. Zheng, J. Mater. Chem. 22 (2012) 1435.

[10] V. Varshney, S.S. Patnaik, A.K. Roy, G. Froudakis, B.L. Farmer, ACS NANO 4 (2010) 1153.

[11] J.Y. Jhan, Y.W. Huang, C.H. Hsu, H. Teng, D. Kuo, P.L. Kuo, Energy 53 (2013) 282.

[12] G.K. Dimitrakakis, E. Tylianakis, G.E. Froudakis, Nano Lett. 8 (2008) 3166.

[13] D. Yu, L. Dai, J. Phys. Chem. Lett. 1 (2010) 467.

[14] V. Varshney, S.S. Patnaik, A.K. Roy, G. Froudakis, B.L. Farmer, ACS NANO 4 (2010) 1153.

[15] F. Du, D. Yu, L. Dai, S. Ganguli, V. Varshney, A.K. Roy, Chem. Mater. 23 (2011) 4810.

[16] F.D. Novaes, R. Rurali, P. Ordejon, ACS NANO 4 (2010) 7596.

[17] Y. Zhu, L. Li, C. Zhang, G. Casillas, Z. Sun , Z. Yan, et al., Nature Commu. 3 (2012) 1.

[18] Z. Yan, L. Ma, Y. Zhu, I. Lahiri, Z. Liu, M.G. Hahm, et al., ACS Nano 7 (2013) 58.

[19] H. Yoshida, S. Takeda, T. Uchiyama, H. Kohno, Y. Homma. Nano Lett. 8 (2008) 2082.

[20] M. Griebel, J. Hamaekers, Comput. Methods. Appl. Mech. Engrg. 193 (2004) 1773.

[21] K. Esfarjani, N. Gorjizadeh, Z. Nasrollahi, Comput. Mater. Sci. 36 (2006) 117.

[22] A. Martinez-Limia, J. Zhao, P.B. Balbuena, J. Mol. Model. 13 (2007) 595.

[23] D. Feng, K. Bolton, A. Rosen, Comput. Mater. Sci. 35 (2006) 243.

[24] D.W. Brenner, O.A. Shenderova, J.A. Harrison, S.J. Stuart, B. Ni, S.B. Sinnott, J. Phys: Condens. Matter. 14 (2002) 783.

[25] D.W. Brenner, Phys. Rev. B 42 (1990) 9458.

[26] J.A. Harrison, C.T. White, R.J. Colton, D.W. Brenner, Phys. Rev. B 46 (1992) 9700.

[27] D.W. Brenner, D.H. Robertson, M.L. Elert, C.T. White, Phys. Rev. Lett. 70 (1993) 2174.

[28] http://www.dftb.org/

[29] A.J. Page, Y. Ohta, S. Irle, K. Morokuma, Acc. Chem. Res. 43 (2010) 1375.

[30] Y. Ohta, Y. Okamoto, S. Irle, K. Morokuma, CARBON 47 (2009) 1270.

[31] Y. Ohta, Y. Okamoto, A.J. Page, S. Irle, K, Morokuma, ACS NANO 3 (2009) 3413.

[32] A.J. Page, H. Yamane, Y. Ohta, S. Irle, K.J. Morokuma, Am. Chem. Soc. 132 (2010) 15699.

[33] A.J. Page, S. Minami, Y. Ohta, S. Irle, K. Morokuma, CABON 48 (2010) 3014.

[34] A.J. Page, S. Irle, K. Morokuma, J. Phys. Chem. C 114 (2010) 8206.

[35] M. Weinert, J.W. Davenport, Phys. Rev. B 45 (1992) 13709.

[36] R.M. Wentzcovitch, J.L. Martins, P.B. Allen, Phys. Rev. B 45 (1992) 11372.

[37] F. Wagner, Th. Laloyaux, M. Scheffler, Phys. Rev. B 57 (1998) 2102.

[38] M. Zhao, X. Liu, Q. Zhang, G. Tian, J. Huang, W. Zhu, et al., ACS NANO 6 (2012) 10759.

[39] Y. Ohta, Y. Okamoto, S. Irle, K. Morokuma, ACS NANO 2 (2008) 1437.

[40] Y. Ohta, Y. Okamoto, S. Irle, K. Morokuma, Phys. Rev. B 79 (2009) 195415.

[41] M. Kumar, Carbon Nanotube Synthesis and Growth Mechanism. In: Yellampalli S, editors. Carbon Nanotubes - Synthesis, Characterization, Applications, InTech; 2011, p. 147-170. (Available from: http://www.intechopen.com/books/carbon-nanotubes-synthesis-characterization-applications/carbonnanotube-synthesis-and-growth-mechanism)

[42] J. Liu, R.L. Davidchack, H.B. Dong. Comput. Mater. Sci. 74 (2013) 92.

CHAPTER 4

GROWTH MECHANISMS OF 3D CARBON NANOTUBE-GRAPHENE JUNCTIONS ON COPPER TEMPLATE: MOLECULAR DYNAMIC SIMULATIONS

4.1 Introduction

Carbon nanotube (CNT) and graphene, as one dimensional and two dimensional materials, attract extraordinary research interests in broad area, across materials science, physics, chemistry, medicine, biology etc. Recently, the 3D nanostructure - hybrid of graphene sheet and pillared single wall or multi-wall CNTs caught more attention in both experimental and theoretical fields.[1-6] Assembling these one dimensional CNT and two dimensional graphene with seamless CNT-graphene junctions can create 3D hybrid nanostructures with new functions while complementing their properties and retaining their advantage in maximum. For instance, the structure of graphene sheet and vertical single-wall or multi-wall CNTs was reported to possess broad application prospect such as energy storage [7], thermal sinker [8, 9] and electronic devices [10, 11].

3D nanostructures were produced in laboratory in the presence of metal catalysts [12-14]. The growth of junction of 3D carbon nanotube-graphene was also simulated via quantum mechanical molecular dynamic method, providing specific theoretic foundations for the experimental effort to fabricate the new 3D structures [15]. However, most 3D nanostructures were fabricated with aid of metal particle catalysts, in which the metal particles remain in the junction structure even after subsequent treatments.

To avoid the problem of catalyst remaining in the 3D CNT-graphene nanostructures, it is highly desirable to synthesize the nanostructures without catalysts. It has been shown that single-layer graphene can be grown on copper substrates [19-25]. X. Li et al. [19] illustrated that

the single layer graphene growth on Cu is mainly ascribed to the low carbon solubility in copper using the ^{12}C ^{13}C isotopic labeled methane. In this chapter, we first prove the growth of single layer graphene on copper template with classic molecular dynamic simulations. Then, we proposed a new process based on copper templates to synthesize the 3D nanostructure without catalysts. The synthesizing process of single CNT-graphene junctions was simulated via molecular dynamic simulations.

4.2 Computational Methodology

4.2.1 Template Growth of Single Layer Graphene

Copper and Nickel are excellent substrate material for graphene growth. Quantum mechanical study of graphene growth on copper and nickel template has been done recently [47-49]. Since we plan to pursue a method to fabricate 3D CNT-graphene nanostructure on Cu template with molecular dynamic simulations, MD modeling of single layer graphene on Cu substrate was carried out first. The system includes a small piece of copper substrate (template) and carbon sources. A triangle (111) face with edge of 7.41 nm of Cu are treated as target surface as shown in **Fig. 4.1** (a). Carbon sources are distributed above the (111) surface. The MD algorithm was used here as implanted in the LAMMPS code to simulate the deposit of carbon atoms on the template by releasing the fixed carbon atoms discontinuously (**Fig. 4.1**(b)). The forces between Cu atoms were calculated using an EAM potential [27-30], while the forces of the C atoms were computed using the second-generation reactive empirical bond-order potential (AIREBO) [31-34]. These many-body potentials have been used to study the growth of carbon materials [35]. The interaction between C and Cu atoms were described by a Lannerd-Jones potential: $E=4\varepsilon\,[(\sigma/r)^{12}-((\sigma/r)^{6}]$ with r the distance between atoms, in which the parameters (ε =

0.02587 eV and σ=3.0825 Å) were used since experimental results has definitely shown that the interaction between the carbon atoms and copper atoms is weak [36, 37]. With a rescaling thermostat to control temperature (1073K), the equations of motion were integrated with a time step of 1.0 fs.

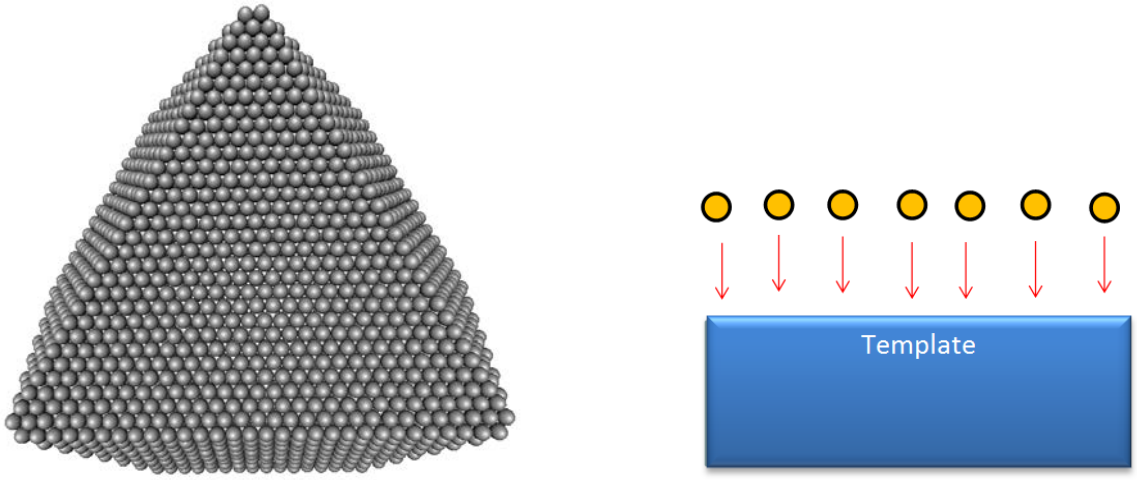

(a) (b)

Fig. 4.1 Cu (111) surface is the target surface and (b) deposit of carbon atoms placed at 0.5 nm above the Cu (111) surface for the growth of single layer graphene.

4.2.2 Template Growth of 3D CNT-graphene Junctions

We proposed to deposit carbon sources on a copper template with hole on it, such that CNT could grow into the hole to form 3D CNT-graphene nanostructures. It has been reported that copper is an ideal substrate for the growth of single-layer graphene [19-25], and single-wall CNT and single-layer graphene and their junctions could be fabricated with the copper template. To verify this idea, we used MD methods to simulate the growing process of the 3D nanostructures. The model system is composed of a copper substrate (template) and carbon

sources. To generate the copper template, a single-crystal copper with a size of 12nmx 12nm x1.672nm was created with (111) on its surface. A hole of given diameter (d = 1~6 nm) was then drilled out of the center of the copper template, as shown in **Fig. 4.2** (a). Carbon sources are distributed over the template with an atom spacing of 0.3 nm. Periodic boundary conditions were applied in three directions to represent an infinite large system. Carbon sources deposited onto the surface of the template as shown in **Fig. 4.2**(b). Detailed calculation procedure follows part 4.2.1.

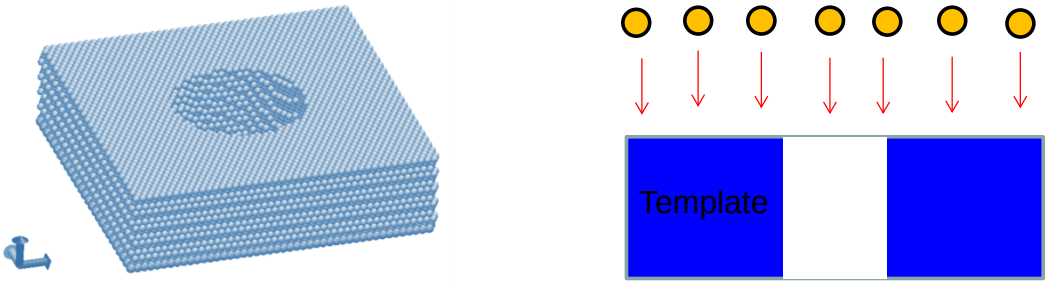

(a) (b)

Fig. 4.2 (a) Copper template with (111) on surface and a hole in the center, and (b) deposit of carbon atoms placed at 0.5 nm above the Cu (111) surface for the growth of 3D CNT-graphene nanostructures.

4.3 Results and Discussion

4.3.1 Growth of Single Layer Graphene on Cu Template

The growth of single layer graphene was simulated with MD method. As carbon sources deposited onto the template surface, they exited in the form of amorphous (**Fig. 4.3** (a)) with the thermal conditions. Then the amorphous carbon changed dramatically, and after about 0.15 μs a part of amorphous carbon spread on Cu surface in the form of graphene while the other part formed a carbon cage (**Fig. 4.3** (b)and (c)). With continuous heating, the carbon system cruised on the substrate, and carbon cage unfolded into a graphene at about 1 μs as shown in **Fig. 4.3** (d).

Since C60 was successfully fabricated in laboratory [50], different types of carbon cages has been discovered [51, 52], which could be transitional carbon configurations during carbon nanotubes and graphene synthesis.

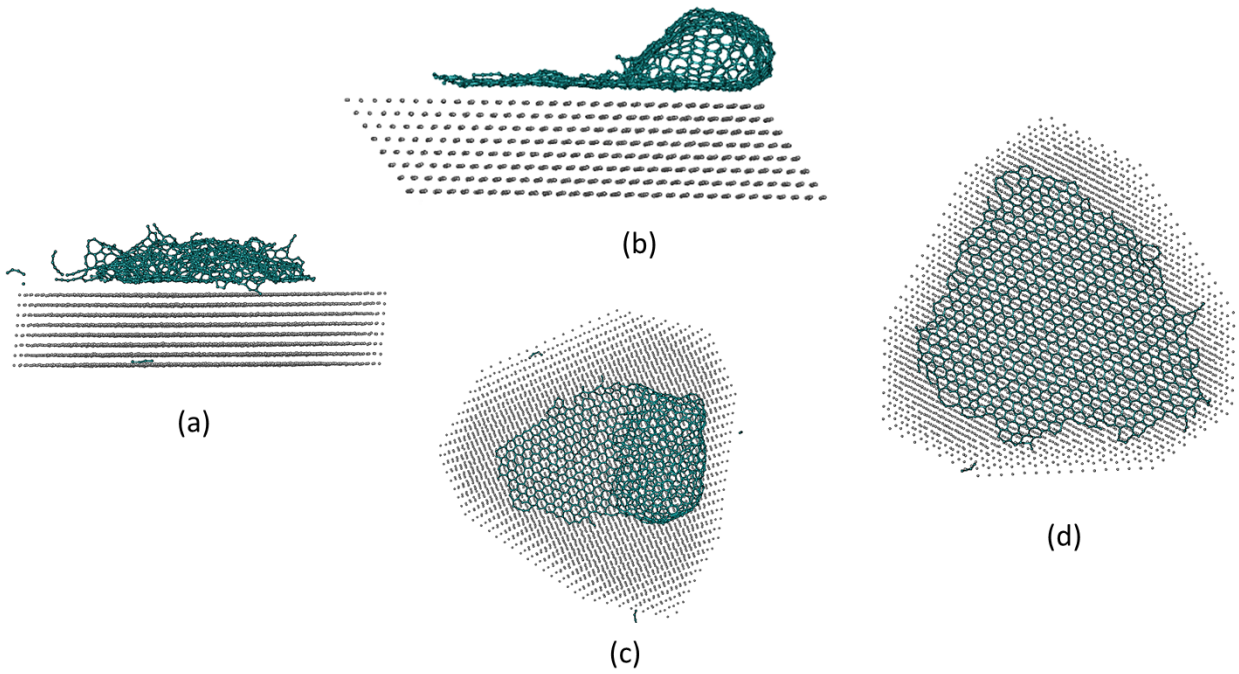

Fig. 4.3 Growth process of single layer graphene on Cu (111) face. (a) Carbon sources form amorphous carbon. (b) and (c) side view and top view of graphene and carbon cage. (d) Carbon cage unfolds to form single layer graphene.

We have studied the structural evolution of single layer graphene during the growth. **Fig. 4.4** (a) shows the number of atoms with sp^2 bonds and sp^3 bonds for graphene growing on Cu template (111) face. The number of sp^2 bonds increases rapidly at the initial stage and then reaches a plateau while the number of other type of bonds (sp^0 and sp^1) quickly reduces to a low level. There are almost no sp^3 bonds in the system mainly because the growing graphene consist of single-layer graphene. Remaining sp^1 and sp^0 bonds are due to edge effect and some flying carbon clusters in the space. **Fig. 4.5** shows some carbon atoms with sp^1 and sp^0 bonds at the

edge. Obviously, the large number of sp^2 bonds indicates well-grown graphene on template (111) surface.

The number of polygons other than hexagons represents the quality of graphene in term of defects. **Fig. 4.4** (b) shows the number of polygons during the graphene growth. While the number of pentagons and heptagons rapidly decreases, the number of hexagons rapidly increases in the early stage. It is well known that pentagons and heptagons are typical defects in carbon materials. As shown in **Fig. 4.4** (b), the population of hexagons is much larger than other types of carbon rings, suggesting that the graphene are in high quality. The remaining heptagons and pentagons are caused by edge effect. **Fig. 4.5** shows that heptagon and pentagon exit on the border area, and in the internal area, carbon atoms form hexagons. Single layer graphene grows exceedingly fast, in just several picoseconds in MD simulations, which can also be observed in growing of 3D CNT-graphene nanostructure.

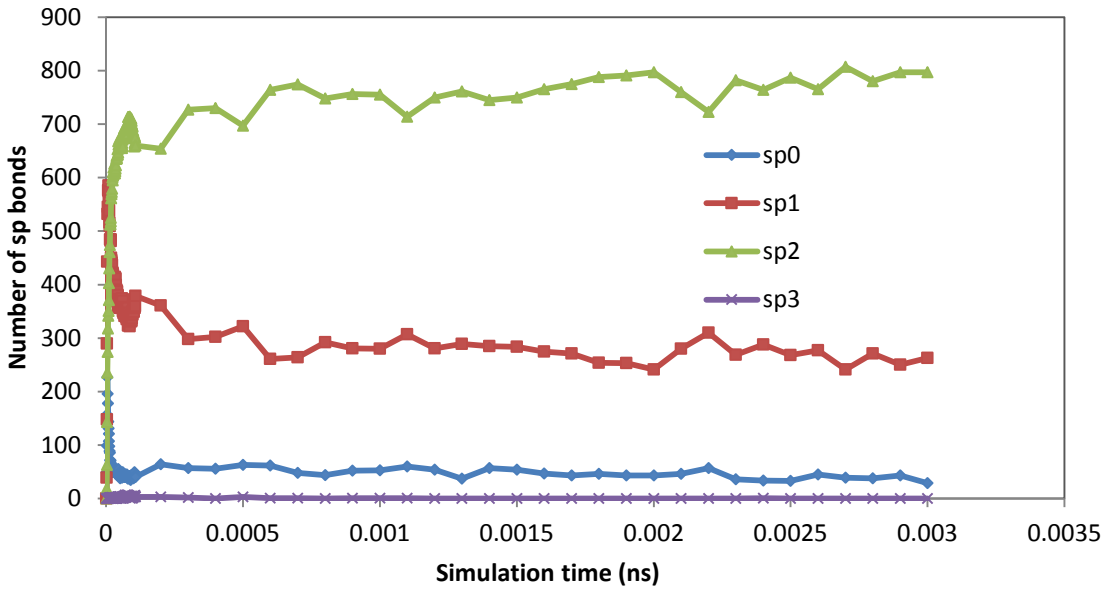

(a)

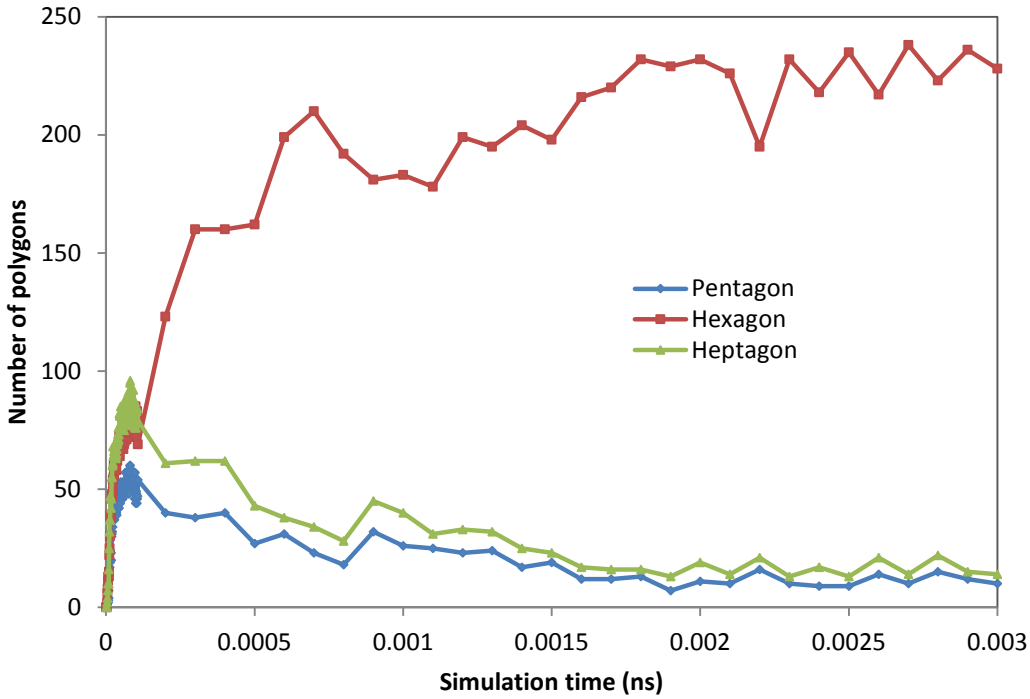

(b)

Fig. 4.4 Structural evolution of the single layer graphene growing on Cu template: (a) number of atoms with different *sp* bond types, and (b) number of polygons during the growth.

Fig. 4.5 gives top view of well-grown single graphene layer on Cu template. Besides edge area, the graphene sheet does not have defects, such as heptagons and pentagons, and the main part of the graphene is composed with carbon hexagons. And interestingly, in local area, carbon hexagons just sit in the space generated by three close packing Cu atoms on (111) face, for instance, as highlighted in red rectangle. This may provide evidence for copper (111) face as graphene layer growth template.

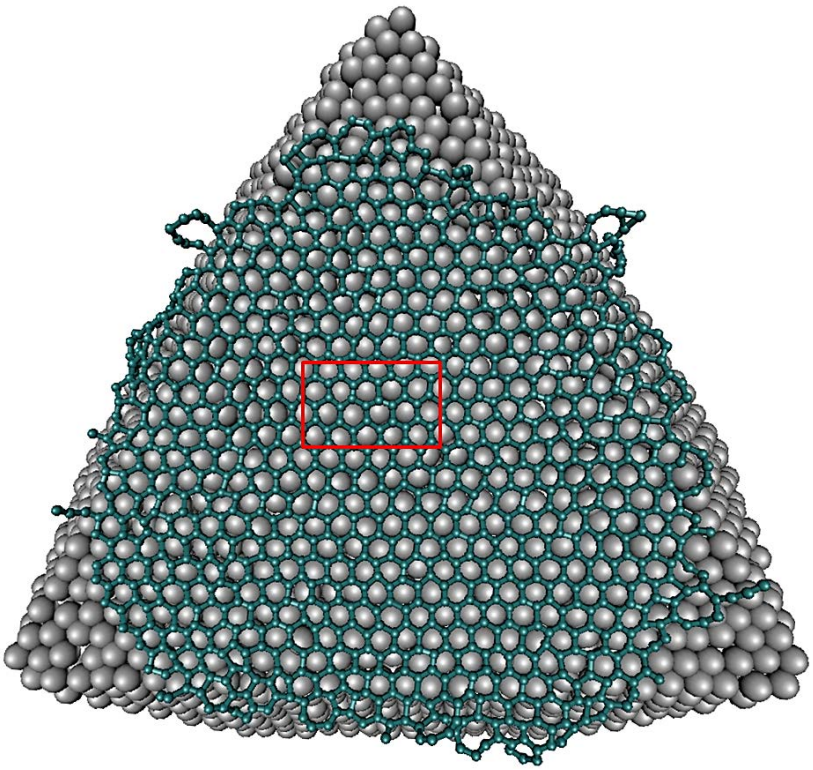

Fig. 4.5 High quality single layer graphene grows on Cu (111) surface. Red highlighted area shows carbon hexagons sit in the space provided by three closed packing Cu atoms on (111)face.

This theoretically proves that the Cu (111) faces are ideal template for single-layer graphene, proposed by Li et al. [53]. Then, we can further explore avenues to grow 3D CNT-graphene nano structure with Cu template.

4.3.2 Growth of Graphene, CNT and their Junctions on Cu Template

The growth processes of graphene, CNT and their junctions on the Cu template with different hole sizes (1-6 nm in diameter) were simulated using classical MD method. Generally, a single layer graphene forms quickly on the (111) surface of the Cu template, followed by the formation of a seamlessly C-C bonded CNT-graphene junction and the growth of CNT.

Eventually, a 3D single-walled CNT-graphene nanostructure was formed and the architecture of 3D structure was determined by the template design.

It was found that there are two growth mechanisms for the junction formation, depending on the size of the hole. When the hole diameter is larger than 3 nm, after the formation of the graphene over the template surface (**Fig. 4.6** (a)), the injected carbon atoms attaches to the remaining dangling bonds in the graphene and the newly formed graphene surrounding the hole curves down into the hole to form an embryo of CNT cap (**Fig. 4.6** (b)). With the feeding of carbon sources, the cap keeps growing into the hole to form a CNT (**Fig. 4.6** (c)). The detailed growing process can be seen in supplementary information (Video S1).

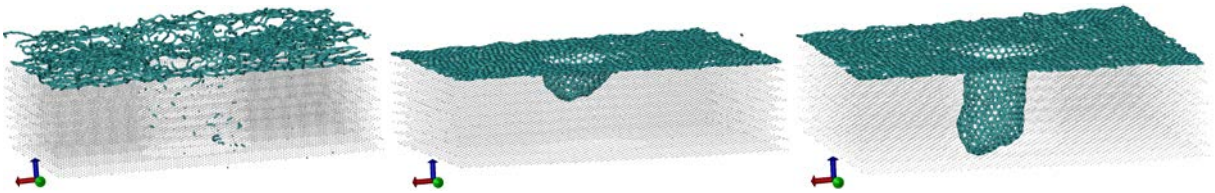

(a) (b) (c)

Fig. 4.6 (a) Carbon atoms deposited over the template surface; (b) formation of graphene and an embryo of CNT cap; (c) The CNT grown into the hole to form CNT-graphene junctions.

When the hole diameter is smaller than 3nm, we observed an interesting CNT growing mechanism, as shown in **Fig 4.7**. Instead of growing into the hole, the embryo of CNT grows upward over the hole to form CNT and junction as shown in **Fig. 4.8**. In the initial stage of growing, the template surface was first covered by randomly distributed carbon atoms (**Fig. 4.7** (b)), and then defective graphene formed from these carbon sources (**Fig. 4.7** (c)). In the initial stage, the graphene sheet has a hole as well at the Cu hole area due to lack of supporting. During relaxation it is generally sealed by C atoms, and a whole piece of graphene sheet formed.

Some carbon dangling bonds is still remained in the graphene, and the injected carbon atoms attach on these dangling bonds to involve the junction growth. The extra C atoms diffuse on the graphene surface in single atom as well as in cluster (**Fig. 4.7** (c)). These carbon sources eventually move into the hole area and a CNT grows out of the graphene, as shown in **Fig 4.7** (d). Since the CNT grows upward over the hole, this growth mode could simplify the template preparation, providing a new route for synthesis of 3D CNT-graphene nanostructures with seamless C-C bonded junction without template/catalyst.

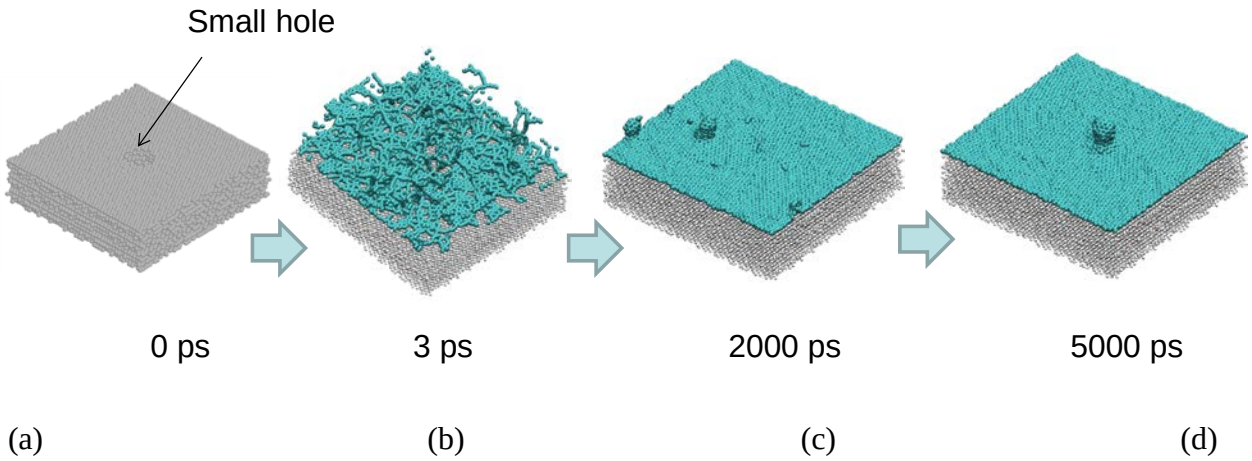

Fig. 4.7 (a) Cu template with small hole (dimameter: 2 nm). (b) Cu template surface was first covered by randomly-distributed carbon atoms. (c) defective graphene formed from these carbon sources and covered the surface and the extra C atoms diffused on the graphene surface in single atom as well as in cluster, and (d) CNT growth out of the graphene after extra carbon atoms diffuse into the hole area.

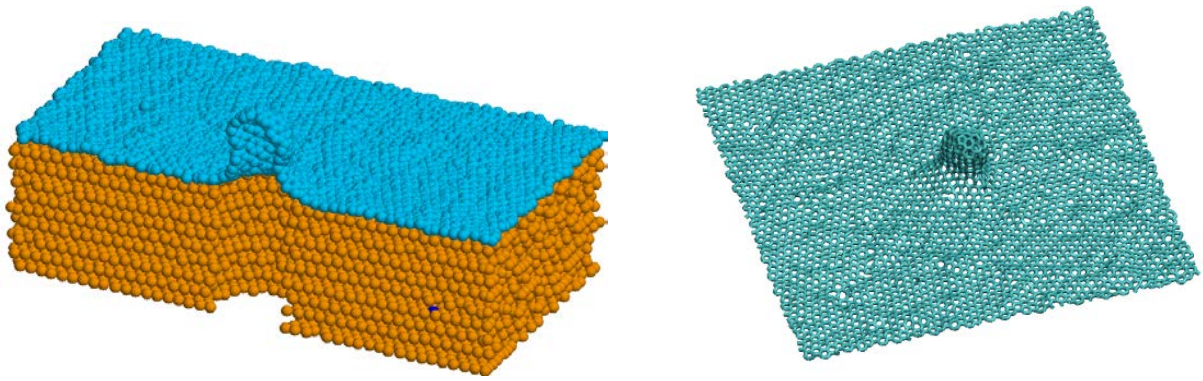

(a) (b)

Fig. 4.8 A CNT growing upward over the hole to form CNT-graphene junction. (a) Cross section of junction. (b) Top view of the junction after the template is removed.

We have studied the structural evolution of 3D nanostructures during their growth. **Fig. 4.9** (a) shows the number of atoms with different bond types for the nanostructure growing on Cu template with a 4 nm diameter hole. The number of sp^2 bonds increases rapidly at the initial stage and then reaches a plateau while the number of other type of bonds (sp^0 and sp^1) quickly reduces to a low level. There are almost no sp^3 bonds in the system mainly because the growing nanostructures consist of single-layer graphene, CNT and junctions. The small numbers of sp^0 and sp^1 bonds indicate defects and dangling bonds remaining due to incomplete relaxation. Obviously, the large number of sp^2 bonds indicates well-grown CNT, graphene and junction on template surface.

The number of polygons other than hexagons represents the quality of CNT and graphene in term of defects. **Fig. 4.9** (b) shows the number of polygons during the growth. While the number of pentagons and heptagons rapidly decreases, the number of hexagons rapidly increases. It is well known that pentagons and heptagons are typical defects in carbon materials and exist simultaneously in the form of Stone-Wales defects. As shown in **Fig. 4.9** (b), the population of hexagons is much larger than other types of carbon rings, suggesting that the CNT- graphene

junctions are in high quality. The microstructure of the junctions was further examined after long time relaxation and both point and line defects were found in the structures, as reported in experiments [45, 46]. **Fig. 4.10** shows a typical structure of CNT-graphene junctions. There are point defect (5577) and grain boundaries in the form of pentagons and heptagons distributed alternatively in graphene (**Fig. 4.10** (a)). Similar line defects are also found in CNT while these defects also exist in the transition region between graphene and CNT (**Fig. 4.10** (b)). The population of pentagons and heptagons in the junction area is larger than that in CNT and graphene. Thus, heptagons and pentagons are crucial for the formation of 3D CNT-graphene junctions.

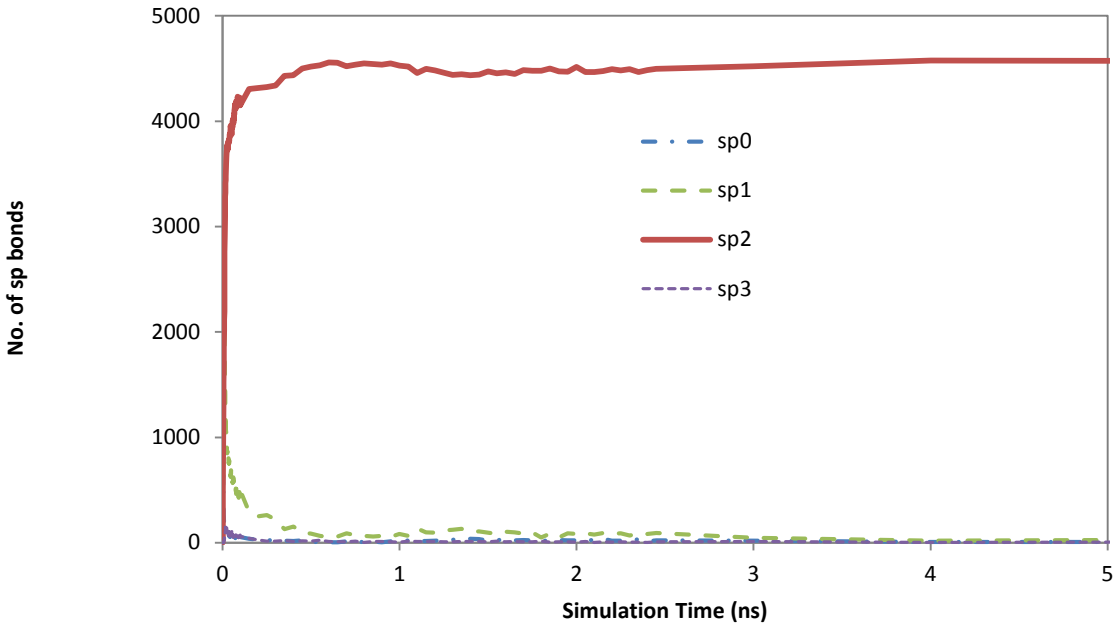

(a)

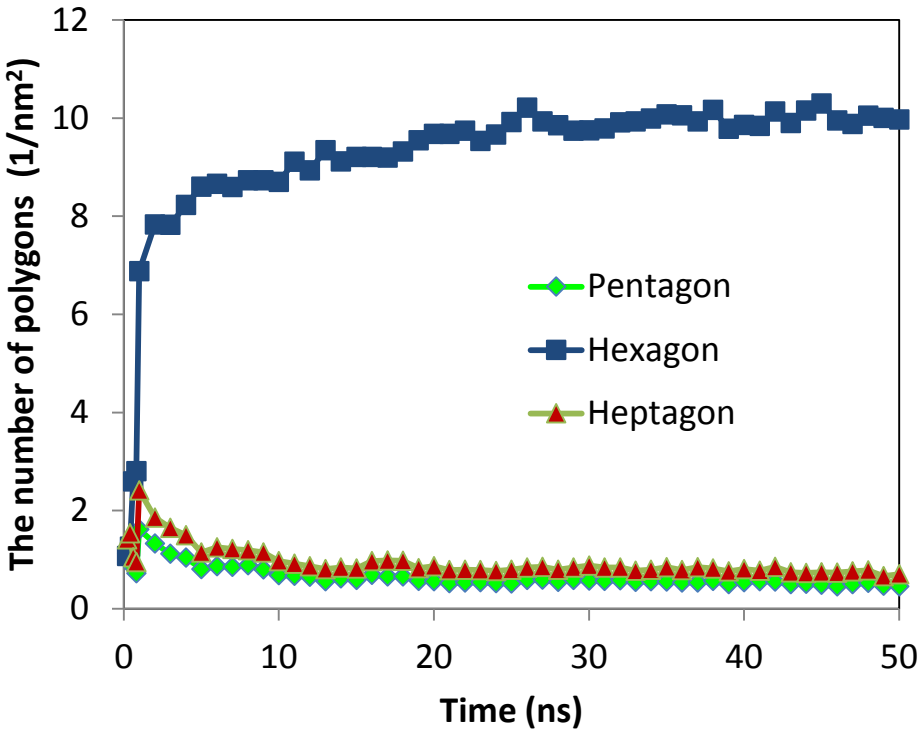

(b)

Fig. 4.9 Structural evolution of the 3D nanostructure growing on Cu template with a 4 nm diameter hole: (a) The number of atoms with different bond types, and (b) the number of polygons during the growth.

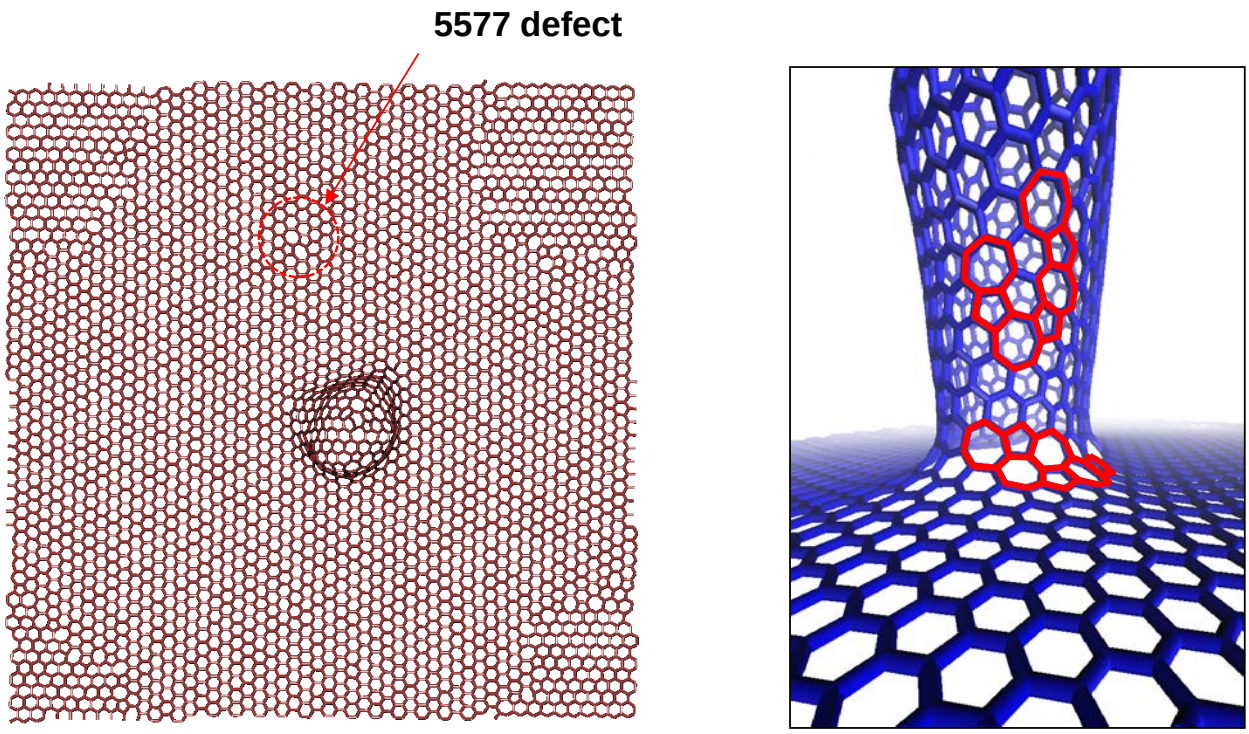

(a) (b)

Fig. 4.10 (a) single-layer CNT-graphene junction with point defect (5577) and grain boundaries in the form of pentagons and heptagons distributed alternatively in graphene, and (b) similar line defects (highlighted in red) in CNT and the transition region between graphene and CNT.

4.4 Conclusions

Growth processes of single layer graphene on Cu template were simulated via classical MD simulation. The newly grown graphene is in high quality, providing molecular dynamic evidence for applications of Cu as templates for carbon nano material growth.

Growth processes of 3D CNT-graphene junction on Cu templates were simulated via classical MD simulations. There are two growing mechanisms depending on the size of template holes: i) CNT growth over small hole, and ii) CNT growth inside large hole. Line and point defects were found in the grown CNT, graphene and junctions. Pentagons and heptagons play an important role in the junction growth especially at the transition region of CNT and graphene. The seamless

C-C junction growth mechanisms found in this study provide a theoretic foundation for growth of 3D nanostructures without any catalysts.

4.5 References

[1] D. Yu, L. Dai, J. Phys. Chem. Lett. 1 (2010) 467.

[2] S. Bae, K. Karthikeyan, Y. Lee, II-K. Oh, CARBON 64 (2013) 527.

[3] C. Kang, R. Baskaran, J. Hwang, B. Ku, W. Choi, CARBON 68 (2014) 493.

[4] Z. Fan, J. Yan, L. Zhi, Q. Zhang, T. Wei , J. Feng, M. Zhang, W. Qian, F. Wei, Adv. Mater. 22 (2010) 3723.

[5] G.C. Loh, E.H.T. Teo, B.K. Tay, J. Appl. Phys. 110 (2011) 083502.

[6] R.P. Wesotowski, A.P. Terzyk, Phys. Chem. Chem. Phys. 13 (2011) 17027.

[7] G.K. Dimitrakakis, E. Tylianakis, G.E. Froudakis, Nano Lett. 8 (2008) 3166.

[8] V. Varshney, S.S. Patnaik, A.K. Roy, G. Froudakis, B.L. Farmer, ACS NANO 4 (2010) 1153.

[9] L. Xu, N. Wei, Y. Zheng, Z. Fan, H. Wang, J. Zheng, J. Mater. Chem. 22 (2012) 1435.

[10] F. Du, D. Yu, L. Dai, S. Ganguli, V. Varshney, A.K. Roy, Chem. Mater. 23 (20110 4810.

[11] Y. Kim, K. Kumar, F.T. Fisher, E. Yang, Nanotechnology 23 (2012) 015301.

[12] J. Lin, C. Zhang, Z. Yan, Y. Zhu, Z. Peng, R.H. Hauge, D. Natelson, J.M. Tour, Nano Lett. 13 (2013) 72.

[13] M. Zhao, X. Liu, Q. Zhang, G. Tian, J. Huang, W. Zhu, F. Wei, ACS NANO 6 (2012) 10759.

[14] J. Wen, Y. Li, W. Yang, Vacuum 101 (2014) 271.

[15] J. Niu, M. Li, W. Choi, L. Dai, Z. Xia, CARBON 67 (2014) 627.

[16] S. Sihn, V. Varshney, A.K. Roy, B.L. Farmer, CARBON 50 (2012) 603.

[17] S. Sihn, V. Varshney, A.K. Roy, 51st AIAA/ASME/ASCE/AHS/ASC Structures, Structural Dynamics, and Materials Conference
18th 12 - 15 April 2010, Orlando, Florida.

[18] F.D. Novaes, R. Rurali, P. Ordejon, ACS NANO 4 (2010) 7596.

[19] X. Li, W. Cai, L. Colombo, R.S. Ruoff, Nano Lett. 9 (2009) 4268.

[20] X. Li, W. Cai, J. An, S. Kim, J. Nah, D. Yang, R. Piner, A. Velamakanni, I. Jung, E. Tutuc, S.K. Banerjee, L. Colombo, R.S. Ruoff, Science 324 (2009) 1312.

[21] J.D. Wood, S.W. Schmucker, A.S. Lyons, E. Pop, J.W. Lyding, Nano Lett. 11 (2011) 4547.

[22] Z. Sun, Z. Yan, J. Yao, E. Beitler, Y. Zhu, J. M. Tour, Nature 468 (2010) 549.

[23] L. Gao, J.R. Guest, N.P. Guisinger, Nano Lett. 10 (2010) 3512.

[24] J.M. Wofford, S. Nie, K.F. McCarty, N.C. Bartelt and O.D. Dubon, Nano Lett. 10 (2010) 4890.

[25] X. Li, C.W. Magnuson, A. Venugopal, R.M. Tromp, J.B. Hannon, E.M. Vogel, L. Colombo, R.S. Ruoff, J. Am. Chem. Soc. 133 (2011) 2816.

[26] S.L. Mielke, D. Troya, S. Zhang, J. Li, S. Xiao, R. Car, R.S. Ruoff, G.C. Schatz, T. Belytschko, Chem. Phys. Lett. 390 (2004) 413.

[27] A.F. Voter, Los Alamos Unclassified Technical Report No. LA-UR-93-3901.

[28] S.J. Zhou, D.M. Beazley, P.S. Lomdahl, B.L. Holian, PRL 78 (1996) 479.

[29] C.L. Liu, J.M. Cohen, J.B. Adams, A.F. Voter, Surf. Sci. 253 (1991) 334.

[30] S.M. Foiles, M.I. Baskes, M.S. Daw, Phys. Rev. B 33 (1986) 7983.

[31] D.W. Brenner, O.A. Shenderova, J.A. Harrison, S.J. Stuart, B. Ni, S.B. Sinnott, J. Phys.: Condens. Matter. 14 (2002) 783.

[32] D.W. Brenner, Phys. Rev. B 42 (1990) 9459.

[33] J.A. Harrison, C.T. White, R.J. Colton, D.W. Brenner, Phys. Rev. B 46 (1992) 9700.

[34] D.W. Brenner, D.H. Robertson, ML. Elert, C. T. White, Phys. Rev. Lett. 70 (1993) 2174.

[35] S. Banerjee, S. Naha, I. K. Puri, Appl. Phys. Lett. 92 (2008) 233121.

[36] A.L. Va´zquez de Parga, F. Calleja, B. Borca, M.C.G. Passeggi, Jr., J.J. Hinarejos, F. Guinea, R. Miranda, PRL 100 (2008) 056807.

[37] P. Sutter, J.T. Sadowski, E. Sutter, Phys. Rev. B 80 (2009) 245411.

[38] http://www.dftb.org/

[39] A.J. Page, Y. Ohta, S. Irle, K. Morokuma, Acc. Chem. Res. 43 (2010) 1375.

[40] Y. Ohta, Y. Okamoto, S. Irle, K. Morokuma, CARBON 47 (2009) 1270.

[41] Y. Ohta, Y. Okamoto, A.J. Page, S. Irle, K. Morokuma, ACS NANO 3 (2009) 3413.

[42] A.J. Page, H. Yamane, Y. Ohta, S. Irle, K. Morokuma, J. Am. Chem. Soc. 132 (2010) 15699.

[43] A.J. Page, S. Minami, Y. Ohta, S. Irle, K. Morokuma, CARBON 48 (2010) 3014.

[44] A.J. Page, S. Irle, K. Morokuma, J. Phys. Chem. C 114 (2010) 8206.

[45] J.C. Meyer, A. Chuvilin, G. Algara-Siller, J. Biskupek, U. Kaiser, Nano Lett. 9 (2009) 2683.

[46] J.C. Meyer, C. Kisielowski, R. Erni, M.D. Rossell, M.F. Crommie, A. Zettl, Nano Lett. 8 (2008) 3582.

[47] Y. Wang, A.J. Page, Y. Nishimoto, H. Qian, K. Morokuma, S. Irle, J. Am. Chem. Soc. 133 (2011) 18837.

[48] L. Meng, Q. Sun, J. Wang, F. Ding, J. Phys. Chem. C 116 (2012) 6097.

[49] W. Zhang, P. Wu, Z. Li, J. Yang, J. Phys. Chem. C 115 (2011) 17782.

[50] W. Kratschmer, L.D. Lamb, K. Fostiropoulos, D.R. Huffman, Nature (London) 347 (1990) 354.

[51] R. Ettl, I. Chao, F. Diederich, R.L. Whetten, Nature (London) 149 (1991) 353.

[52] T.G. Schmalz, W.A. Seitz, D.J. Klein, G.E. Hite, J. Am. Chem. Soc. 110 (1988) 1113.

[53] X. Li, W. Cai, J. An, S. Kim, J. Nah, D. Yang, R. Piner, A. Velamakanni, I. Jung, E. Tutuc, S.K. Banerjee, L. Colombo, R.S. Ruoff, Science 324 (2009)1312.

CHAPTER 5

MOLECULAR DYNAMIC SIMULATIONS OF GROWTH MECHANISMS OF FILLETED CARBON NANOTUBE-GRAPHENE JUNCTIONS

5.1 Introduction

Carbon nanotube (CNT) and graphene are famous carbon allotrope due to their special structure and excellent properties. CNT is cylindrical carbon networks with high aspect ratio, and graphene is one single layer carbon networks in plan direction. They possess similar properties due to the same carbon atoms arrangements. It is desirable to combine CNT and graphene into 3D CNT-graphene nanostructures with new mechanical, thermal and electric properties. Theoretical studies on 3D nano structures have revealed outstanding mechanical, thermal and electrical properties of this 3D material, which provides huge potential applications on aerospace, integrated circuit, energy generation and storage. Some experimental strategies have been developed to synthesis the 3D nanostructure. Zhao et al. [1] produced covalent C-C bonds junction through one-step Catalytic Growth. Du et al. [2] use the method of intercalated growth of vertical aligned CNTs into thermally expanded highly ordered pyrolytic graphite. Yan et al. [3] got hybrid material with the aid of Al_2O_3 porous film. However, most 3D nanostructures were fabricated with aid of metal particle catalysts, in which the metal particles remain in the junction structure even after subsequent treatments.

In chapter 4, we have simulated 3D junction growth on Cu template without catalyst via MD method, in which CNT, graphene, and junction are in the configuration of single layer. Herein, we would like to investigate new avenues to grow multi-layer junctions. It has been shown that multi-layer graphene and CNTs can be grown on Al_2O_3 substrates [4-10]. Bae et al. have synthesized aligned vertical multi-wall CNTs on a porous anodic aluminum oxide template

[24] without any catalysts. It is believed that the anodic aluminum oxide template works as catalysts for CNTs growth. Moreover, two-layer graphene was prepared on large porous Al_2O_3 ceramic pieces without other metal catalysts involved [8]. As reported, the CNT growth on Al_2O_3 template is distinguished from other templates. Growth conditions are more controllable since the Al_2O_3 can be tailored on the hole width and depth by changing anodizing voltage and time [8]. Moreover, CNTs obtained by porous Al_2O_3 template are usually in good quality and high order due to the organized Al_2O_3 template holes [8]. Applications of CNTs and graphene upon alumina are attractive. The alumina coated CNTs are successful Li-ion batteries anodes with high capacity [22], and CNT embedded alumina cathodes offer high electron emissions [23]. The porous graphene/Al_2O_3 composites have potential applications such as light-emitting diode (LED) and other electronic devices [8]. Therefore, it is expected that multi-layer 3D CNT-graphene nano architecture would grow on porous Al_2O_3 templates.

Generally, in mechanical engineering, a filleted junction is popular when two individual components are welded together, which is a bevel at the corner of two parts connection. For the junction of 3D nano structure, the vertical CNT and parallel graphene form a right angle, which can cause stress concentrations, lower durable of mechanical load, and hinder electron and phonon transportations. In this situation, a fillet is necessary at the exterior corner of the junction to distribute stress, thermal, and electrical concentrations.

In this chapter, we proposed a new process based on Al_2O_3 templates to synthesize the filleted multi-wall 3D nanostructure without catalysts. The synthesizing process of single CNT-graphene junctions with fillets was simulated via molecular dynamic simulations. Furthermore, an analytical model was developed to analyze the stability of the filleted junction.

5.2 Computational Methodology

5.2.1 Template Growth of 3D CNT-graphene Junctions

Template-grown CNT-graphene junctions were made by depositing carbon sources on amorphous alumina templates with hole on them, such that CNT could grow into the hole to form 3D CNT-graphene nanostructures. Molecular dynamic (MD) method was employed to simulate the growing process of the 3D nanostructures. The model system is composed of an amorphous Al_2O_3 substrate (template) and carbon sources. To generate the amorphous alumina mold (**Fig. 5.1** (b)), an alumina lattice containing 2604 O atoms and 1620 Al atom was heated at temperature 5000 K for 350 ps and then quenched to room temperature. The amorphous alumina density is 3.28 g/cm^3 according to literatures [11]. The system was healed at temperature 1073 K with templates fixed and carbon sources relaxed to grow filleted 3D junction. Periodic boundary conditions were applied in three directions to represent an infinite large system. In some cases such as smaller hole and multi-layer graphene, the hole becomes too small. In order to form proper junctions with a hole and CNT, a core was used to form the hole of the junctions. It is trimmed to form a tunnel inside and carbon sources are filled in the templates.

The MD algorithm was used here as implanted in the LAMMPS code to simulate the deposit of carbon atoms on the template by releasing the fixed carbon atoms (**Fig. 5.1** (a)). The interactions in Al_2O_3 templates were calculated using the transferable potential of Matsui [12], while the forces of the C atoms were computed using the second-generation reactive empirical bond-order potential (AIREBO) [13-16]. These many-body potentials have been used to study the growth of carbon materials [19]. The interaction between C and Al O atoms were described by a Lannerd-Jones potential: $E=4\varepsilon\,[(\sigma/r)^{12}-((\sigma/r)^{6}]$, where r is the distance between atoms and the parameters are[17, 18]: ε_{Al-C}= 0.0315 eV, ε_{O-C}= 0.00326 eV, σ_{Al-C}= 2.976 Å and σ_{O-C}=

3.19 Å. With a rescaling thermostat to control temperature (1073K), the equations of motion were integrated with a time step of 0.25 fs. Subsequently, grown junction was heat treated at temperature at 3000K for 2.5 μs.

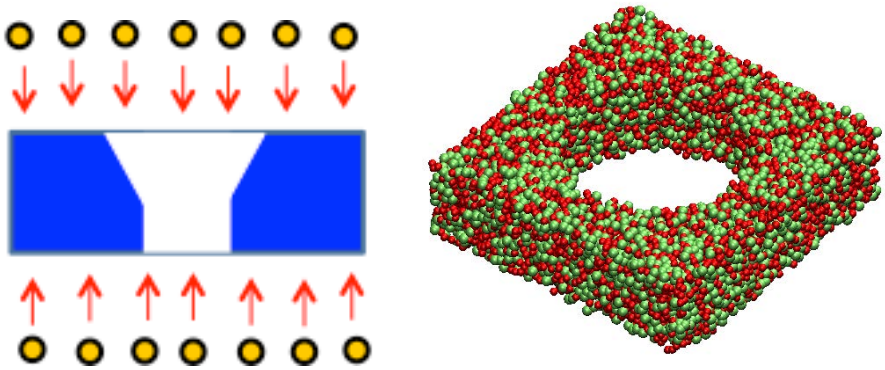

(a) (b)

Fig. 5.1 (a) Schematics of Al_2O_3 template with a filleted hole in the center, (b) MD model of the template.

5.3 Analysis of Stability of Filleted CNT-graphene Junctions

We consider a filleted CNT-graphene junction with filleted length *L* and angle θ, and CNT diameter *d*, as shown in **Fig. 5.2**. There is also an angle formed at the intersection of fillet and graphene (Point B), α, which depends on the angle θ.

$$\alpha = \frac{3\pi}{2} - \theta \tag{5.1}$$

The fillet may be connected by two curves with radii, r_1 and r_2, at the intersections (Points A, and B), respectively. In general, the curvatures are related to the intersection angles. We assume that the radius of the curves is proportional to the angles as

$$r_1 = r_0[1 + n\left(\theta - \frac{\pi}{2}\right)] \tag{5.2}$$

$$r_2 = r_0[1 + n(\pi - \theta)] \tag{5.3}$$

where r_0 and n are the unknown parameters.

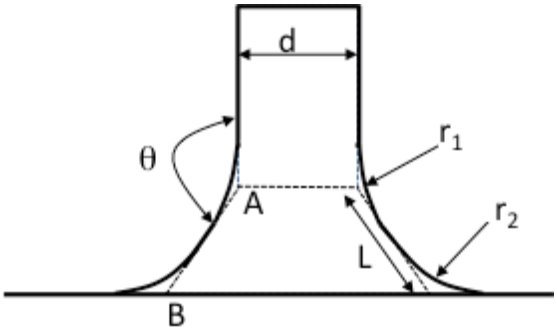

Fig. 5.2 Schematics of CNT-graphene junction

It is known that, relative to the ground state of flat graphene, the deformation of a curved graphene involves both the bending curvature κ and in-plane strain ε [20]. As the tube radius increases, the bending energy ($W_b = D\kappa^2 / 2$) decreases and the in-plane strain energy ($W_s = C\varepsilon^2 / 2$) increases, where D and C are the elastic moduli for bending and in-plane stretch, respectively. For a fully relaxed curved graphene and under pure bending conditions, the total strain energy of the filleted junction with respect to the bending curvature, can be approximately expressed as

$$W = (W_1 A_1 + W_2 A_2)/(A_1 + A_2) \tag{5.4}$$

where W_1 and W_2 are the bending energy of curves A and B, respectively. A_1 and A_2 are the areas of curves A and B, and are approximated as

$$A_1 = \pi d r_1 (\pi - \theta) \tag{5.5}$$

$$A_2 = \pi d r_2 \left(\theta - \frac{\pi}{2}\right) \left[1 + \frac{2L}{d}\sin(\pi - \theta)\right] \tag{5.6}$$

Substituting bending energy expression ($W_b = D/2r^2$, where r is the radius of curves) and

Eqs.(5.5) and (5.6) into Eq.(5.4) yields

$$W = \frac{D}{2r_0^2}\frac{\left\{(\pi-\theta)/[1+n(\theta-\frac{\pi}{2})+(\theta-\frac{\pi}{2})/[1+n(\pi-\theta)]\ \left[1+\frac{2L}{d}\sin(\pi-\theta)\right]\right\}}{\left\{(\pi-\theta)[1+n\left(\theta-\frac{\pi}{2}\right)]+\left(\theta-\frac{\pi}{2}\right)[1+n(\pi-\theta)]\ \left[1+\frac{2L}{d}\sin(\pi-\theta)\right]\right\}} \quad (5.7)$$

Therefore, the total energy is a function of the angle θ and there may be a critical angle with minimum energy for the junctions.

5.4 Results and Discussion

5.4.1 Formation of Large-scale 3D CNT-graphene junctions

The growth processes of graphene, CNT and their junctions on the alumina template were simulated using classical MD method. Generally, a single and multi-layer graphene forms quickly on the surface of the template, with the simultaneous formation of a seamlessly C-C bonded CNT-graphene junction. Eventually, a 3D CNT-graphene nanostructure was formed and the architecture of 3D structure was determined by the template design. The structures of the junctions basically show graphene-layered structures parallel to the template surfaces, but sp^3 bonds are found between the layers, making the layers rough at the surface (**Fig. 5.3**). These disordered microstructures are similar to those observed in the experiment. After long heat treatment at high temperature, the disordered graphene layers can become much ordered.

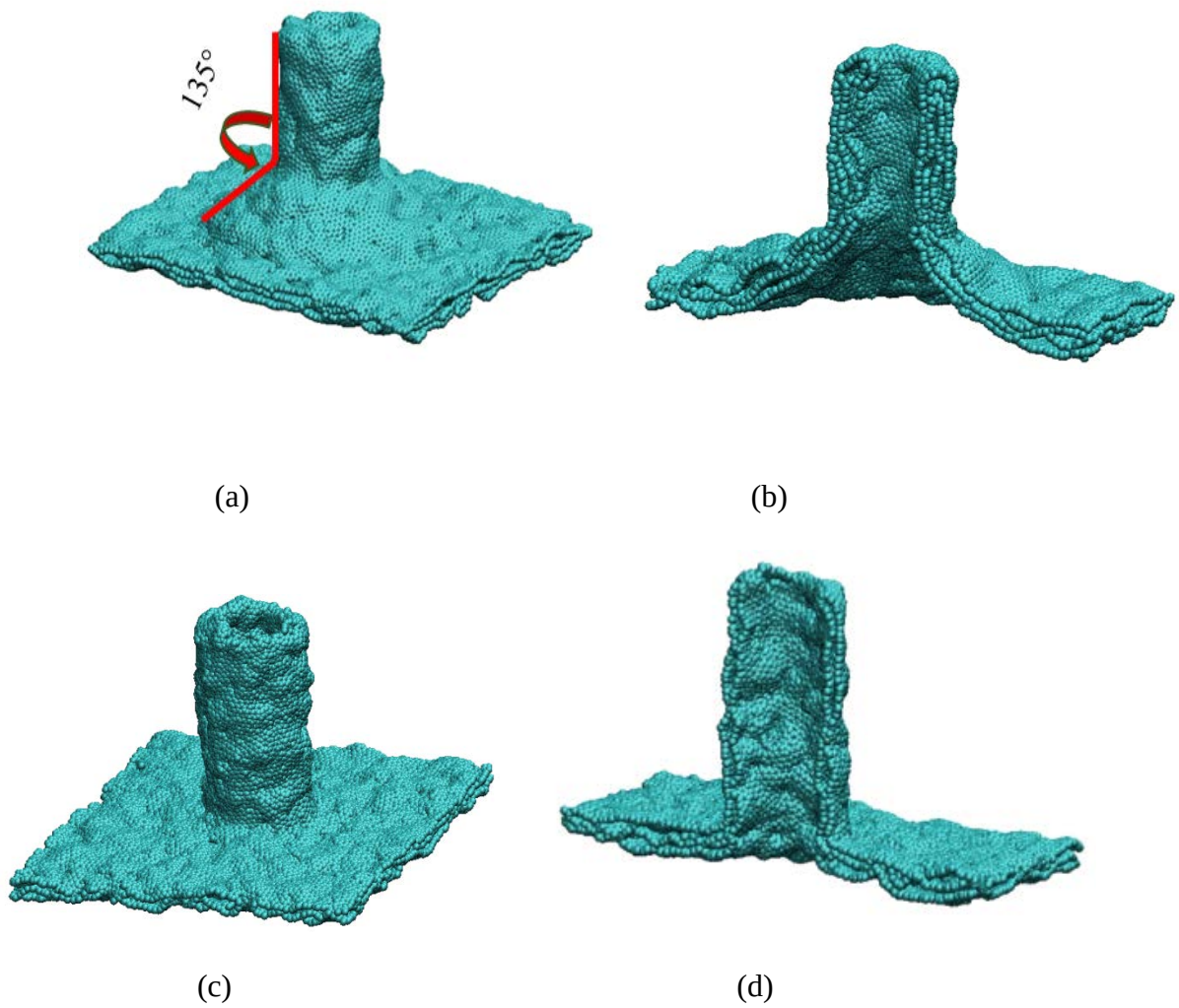

Fig. 5.3 (a) Side view and (b) Cross section of three-layered CNT-graphene junctions with 135^0 fillet. (c) Side view and (d) Cross section of three-layered CNT-graphene junctions with no fillet.

5.4.2 Fillet Shapes of 3D CNT-graphene Junctions

We have calculated the strain energy due to the bending curvature within the junctions. **Fig. 5.4** show the strain energy normalized by ($D/2r_0^2$) as a function of the angle θ between the CNT and fillet. With increasing the angle from 90^o to 180^o (the possible angle for the junctions), the energy initially reduces and then increases. There is a critical angle at which the energy reaches a minimum value. From energetic point of view, the junction with this critical angle will

be most stable. Since *n* in equations (5.2-5.3) is unknown, we have adjusted the value of n and calculated the critical angle which is ~120^0. These predicted value is however smaller than those observed in the experiment. The discrepancy between the analytical model and experiment may be attributed to the number of factors such as residual stresses, defects and multi-layer walls. Anyway, the simple analytical model captures the major feature of the junctions—fillet.

To confirm the analytical predictions, we made the CNT-graphene junctions with different fillets by adjusting the fillet angle of the templates using MD simulation, as shown in **Fig. 5.3**. These model junctions are double-layer graphene structures with sp^3 bonds between the layers. The CNT diameter and graphene size are the same for all these models. Since the total potentials of the systems represent the stability of the structures, we calculate the potentials (E) for each junction structures at near zero temperature (T=0.05K). The normalized potentials ($1 - \frac{E_\theta - E_{90}}{E_{90}}$), where E_{90} is the potential at $\theta = 90^0$ are also plotted in **Fig. 5.4** (b). The MD results show that the minimum potential occurs at $= 135^0$, which is consistent with the experimental observation. Thus, the 1350-fillets are naturally formed because of the minimum energy required to form the junctions.

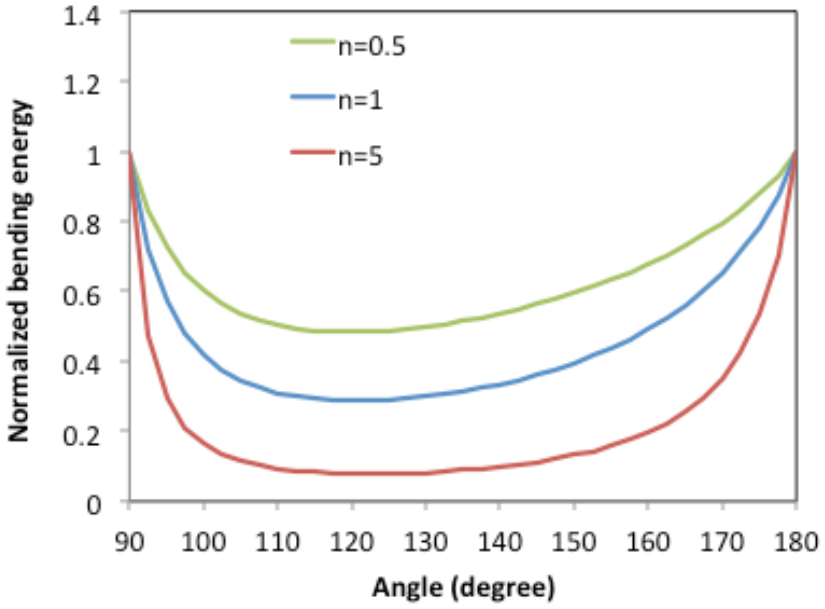

(a)

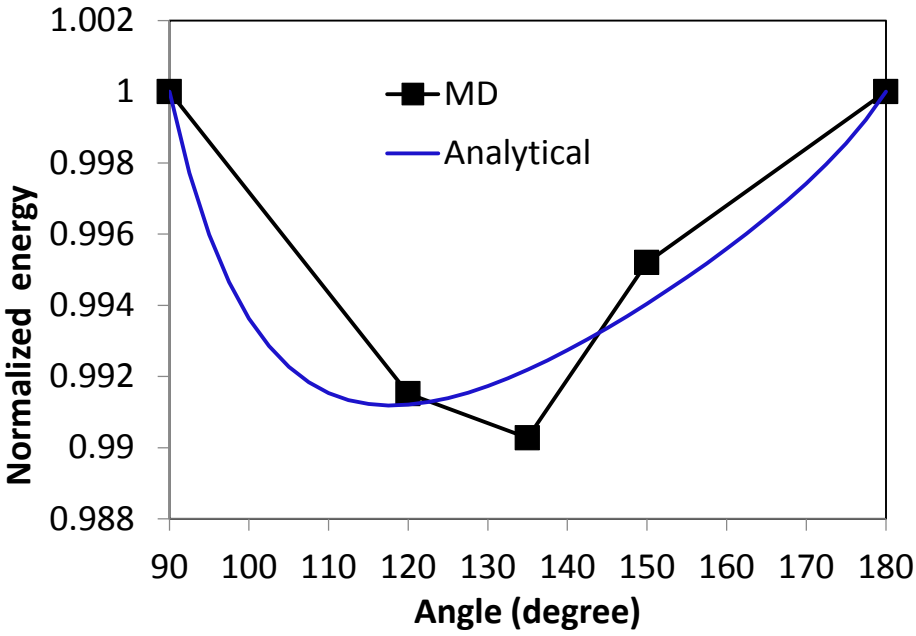

(b)

Fig. 5.4 (a) Normalized bending energy as a function of fillet angle, and (b) Normalized bending energy, predicted by theoretical analysis (Eq.7) and normalized potential energy calculated by MD as a function of the fillet angle.

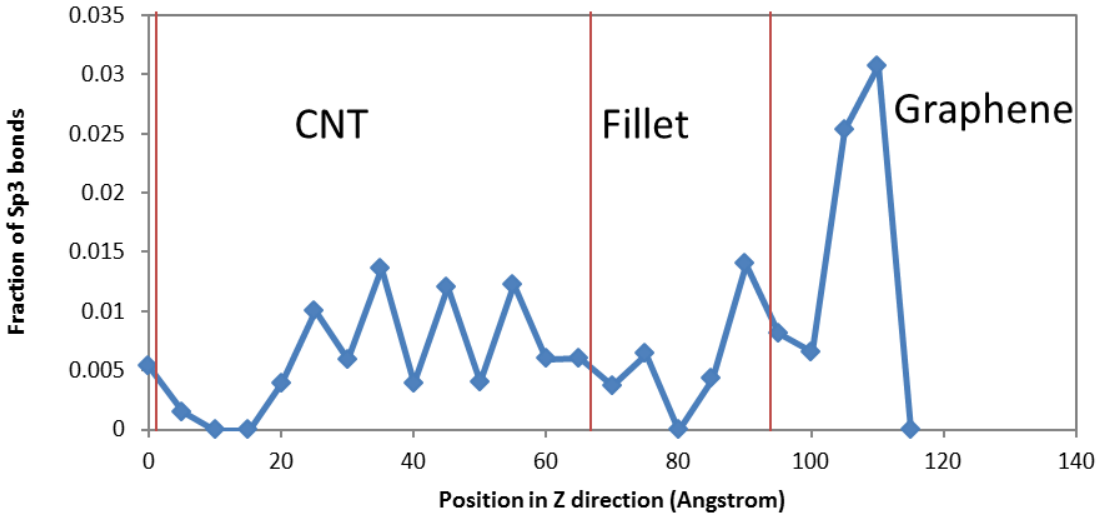

Fig. 5.5 Fraction of atoms with *sp3* bonds versus position in z direction for 135˚filleted junction.

It is reported that sp^3 bonds have huge effect on multi wall carbon nanotubes, including load transfer, buckling strength, and energy dissipation [21]. The fraction of atoms with sp^3 bonds for junctions were counted. The plot in **Fig. 5.5** represents 135° filleted junction. sp^3 bonds evenly distributed between the inter walls of CNT, fillet, and graphene, proving that 3D junction is composed with multiwall CNT and graphene. As shown in **Fig. 5.3**, the surface of junction is rough because of sp^3 existance, which provides stress concentration points and heat transfer obstruction points to influence mechanical and thermal properties of 3D junctions. It is expected that controlling of mechanical and thermal properties can be achineved through sp^3 engineering.

5.5 Conclusions

Growth processes of 3D CNT-graphene junction on alumina templates were simulated via classical MD simulations. Multi-layer CNT-graphene junctions with fillet were formed on the alumina template. In such growth condition, there are sp^3 bonds between the layers, which

make the surface rough. A simple analytical model is developed to explain why the fillet takes the particular angle (135^0). The model predicts that there is a critical fillet angle, at which the system energy reaches its minimum value. The predictions are consistent with the MD simulation and experimental observations. Our simulations show that it possible to synthesize high-quality 3D CNT-graphene nanostructures using template methods without catalysts.

5.6 References

[1] M.Q. Zhao, X.F. Liu, Q. Zhang, G.L. Tian, J.Q. Huang, W. Zhu, F. Wei, ACS NANO 6 (2012) 10759.

[2] F. Du, D. Yu, L. Dai, S. Ganguli, V. Varshney, A.K. Roy, Chem. Mater. 23 (2011) 4810.

[3] Z. Yan, L. Ma,Y. Zhu, I. Lahiri, M.G. Hahm, Z. Liu, S. Yang, C. Xiang, W. Lu, Z. Peng, Z. Sun, C. Kittrell, J. Lou, W. Choi, P.M. Ajayan, J.M. Tour, ACS Nano 7 (2013) 58.

[4] G.P. Sklar, K. Paramguru, M. Misra, J.C. LaCombe, Nanotechnology 16 (2005) 1265.

[5] Z Xia, L. Riester, W.A. Curtin, H. Li, B.W. Sheldon, J. Liang, B. Chang, J.M. Xu, Acta Materialia 52 (2004) 931.

[6] J. Li, C. Papadopoulos, J.M. Xu, M. Moskovits, Appl. Phys. Lett. 75 (1999) 367.

[7] Q.-L. Chen, K.-H. Xue, W. Shen, F.-F. Tao, S.-Y. Yin, W. Xu, Electrochimica Acta 49 (2004) 4157.

[8] M. Zhou, T. Lin, F. Huang, Y. Zhong, Z. Wang, Y. Tang, H. Bi, D. Wan, J. Lin, Adv. Funct. Mater. 23 (2013) 2263.

[9] M. Zhou, H. Bi, T. Lin, X. Lü, F. Huang, J. Lin, J. Mater. Chem. A 2 (2014) 2187.

[10] X. Liu, T. Lin, M. Zhou, H. Bi, H. Cui, D. Wan, F. Huang, J. Lin, Carbon 71 (2014) 20.

[11] G. Gutiérrez, Phys. Rev. B 65 (2002) 104202.

[12] M. Matsui, Miner. Mag. 58A (1994) 571.

[13] D.W. Brenner, O.A. Shenderova, J.A. Harrison, S.J. Stuart, B. Ni, S. B. Sinnott, J. Phys.: Condens. Matter. 14 (2002) 783.

[14] D.W. Brenner, Phys. Rev. B, 42 (1990) 9459.

[15] J.A. Harrison, C.T. White, R.J. Colton, D.W. Brenner, Phys. Rev. B 46 (1992) 9700.

[16] D.W. Brenner, D.H. Robertson, ML. Elert, C.T. White, Phys Rev Lett. 70 (1993) 2174.

[17] K. Kobayashi, M. Shibahara, A molecular dynamics study on behavior of carbon clusters in a nano channel. 6th Asia-Pacific Conference on Combustion, Nagoya Congress Center, Nagoya, Japan. 20-23 May 2007.

[18] T. Werder, J.H. Walther, R.L. Jaffe, T. Halicioglu, P. Koumoutsakos, J. Phys. Chem. B 107 (2003) 1345.

[19] S. Banerjee, S. Naha, I.K. Puri, Appl. Phys. Lett. 92 (2008) 233121.

[20] Q. Lu, R. Huang, J. Comput. Theor. Nanosci. (in press; preprint available at http://www.ae.utexas.edu/~ruihuang/papers/Graphene2.pdf).

[21] Z.H. Xia, P.R. Guduru, W.A. Curtin, PRL 98 (2007) 245501.

[22] I. Lahiri, S.-M. Oh, J.Y. Hwang, C. Kang, M. Choi, H. Jeon, R. Banerjee, Y.-K. Sun, W. Choi, J. Mater. Chem. 21 (2011) 13621

[23] R. Seelaboyina, I. Lahiri, W. Choi, Nanotechnology 21 (2010) 145206.

[24] E.J. Bae, W. Choi, K.S. Jeong, J.U. Chu, G.-S. Park, S. Song, I.K. Yoo, Adv. Mater. 14 (2002) 277.

CHAPTER 6

MECHANICAL PROPERTIES INVESTIGATION OF JUNCTIONS IN 3D CARBON NANOTUBE-GRAPHENE NANO ARCHITECTURE

6.1 Introduction

As one dimensional and two dimension materials, carbon nanotubes and graphene have anisotropic mechanical stabilities and properties. For CNT, strength in axial direction is much higher than that in tangential direction. For graphene, it is much stronger in plane direction than out of plane direction. These are because of unique material structures, that is, sp^2 C-C bonds determine excellent mechanical properties in strong strength direction and Van der Waals forces mainly control the interactions in weak strength direction. Other properties, such as electronic transportation and thermal conductivity etc., are in similar situations for CNT and graphene. Therefore, the 3D CNT-graphene nano structures are expected to overcome these shortcomings, since it has covalent C-C sp^2 bonds in all three directions.

In this chapter, mechanical properties of 3D structure will be investigated with both first principle and molecular dynamic methods. We have grown multi layers 3D nanostructure in previous chapters, and a lot of sp^3 bonds found significantly influencing mechanical properties. Therefore, effect of sp^3 bonds on CNT reinforced amorphous carbon matrix composites will be investigated with classical MD. Then, mechanical properties of various filleted 3D junction was tested through pullout. Finally, tensile tests of different types of junctions including seamless C-C bond junctions (**Fig. 6.6** (a)), the junctions embedded with particles between CNT and graphene (C-Fe-C or C-Ni-C junctions; **Fig. 6.6** (b)) and the junctions with particle embedded inside CNT (**Fig. 6.6** (c)) will be simulated via quantum mechanical molecular dynamic method. Finally, tensile test of filleted junctions will be simulated using MD methods.

6.2 Effect of sp^3 Bonds on Toughening Mechanisms in Carbon Nanotube-Reinforced Amorphous Carbon Matrix Composites

Nanocomposites with microstructures comprising of various nanofibers and nanoparticles in a lubricious matrix such as amorphous carbon (a-C) can produce superior mechanical and tribological properties. The a-C based composites with carbon nanotubes (CNT), nano-diamond, and TiC nano-particles were fabricated and reported to have high hardness, very low friction coefficient and high elastic recovery [23, 24, 25, 26, 27, 28]. These materials are excellent candidates for protective applications as cutting or drilling tools; however, for tribological applications, toughness or load capacity are also needed in order to prevent the brittle fracture of the coating under severe conditions.

In traditional fiber-reinforced ceramic composites, fiber/matrix interface plays an essential role in toughening. The first fracture mode in these materials is matrix cracking. If the interface is weak enough for the matrix crack to be deflected along the interface, the fibers remain intact and the composites can be tough. If the interface is too strong, the matrix crack penetrates into the fibers and the composite is brittle like a monolithic ceramic. Therefore, the crack propagation behavior at the interface is critical to toughening in fiber-reinforced ceramic composites. The mechanics of crack-interface interactions in microscale fiber composites have been addressed in several papers [29, 30, 31, 32], which are primarily concerned with interface debonding and crack kinking. Criteria for transition from interface debonding to crack penetration were given based on energy or stress approaches. At the nanoscale, similar toughening mechanisms can occur [33], but the intrinsic lengths and nanostructural lengths are intertwined and so interfacial behavior may be quite different from the microscale composites. In particular, for amorphous carbon (a-C) based composite systems, both van der Waals forces

and Poisson effects could be significant due to the molecular scale of the interfaces. Although some work has been done on molecular dynamics simulations of diamond and a-C composites [34, 35, 36, 37, 38], little is known about the crack-interface interactions at the molecular scale in these materials.

The main motivation of this section is to understand the crack deflection/penetration at the interfaces of CNT/a-C composites, i.e., brittle-to-tough transitions in the materials. Molecular dynamics simulations were performed to analyze interfacial stress and the crack deflection versus penetration for a crack with the tip on the interface in CNT/a-C composites. We show that the structure of the CNT reinforcement –ideal multi-wall vs. multi-wall with interwall sp^3 bonding – influences crack deflection/penetration. Since sp^3 bond in multi-walled CNTs can be controlled by several techniques [39, 40], our results thus suggest that a-C matrix composites reinforced by the multi-walled CNTs with interwall bonding can be engineered for higher toughness.

6.2.1 Models and Computational Details

We study a perpendicular matrix crack approaching the interface between a single carbon nanotube and a-C matrix in a composite. There are two possible failure paths: crack deflection on the interface; and crack penetration across the interface. Unit cells composed of a half the CNT, matrix and crack was used due to symmetry, as shown in **Fig. 6.1**. Ideal double-wall CNTs (DWCNTs) in armchair configurations were generated with the graphitic C-C bond length of 0.142 nm. Nanotube diameters in the range of d = 1.66 nm with a length of $L = 20 - 40$ nm were all calculations. sp^3 bonds were introduced between DWCNT walls by a procedure described in detail in [41]; their density is defined as the ratio of the number of sp^3 bonds to the

total number of atoms in nanotubes. The nanotube was then relaxed to equilibrium under zero applied loading. A diamond matrix of cross-sectional dimensions 3nm x 3nm was created. A hole of some diameter was then drilled out of the center of the diamond sample and a nanotube was then inserted into it. The amorphous matrix is then generated by melting at 6000 ~ 7000K and subsequent quenching of the surrounding diamond atoms, while keeping the atoms of the CNT frozen in their ideal positions. During the process, the matrix was allowed to expand and homogenize in a certain space such that the density of the amorphous carbon matrix can be controlled around the density of 2.0-2.3 g/cm^3. Next, the a-C matrix was cut to form a matrix crack with a width of 0.3 nm in the middle of the sample. To control the CNT/matrix interfacial strength, a layer of C atoms on the matrix surface, with a given thickness, was removed. Finally, the CNT was unfrozen and the entire system was fully relaxed to equilibrium at 0.05K.

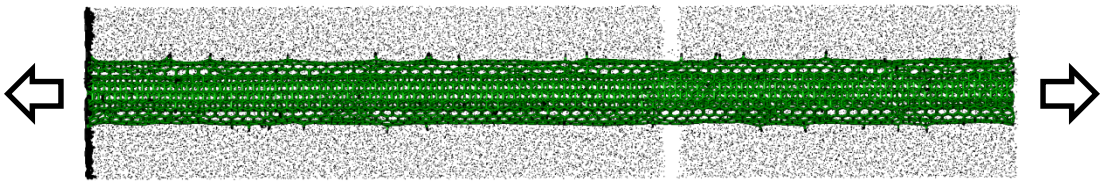

(a)

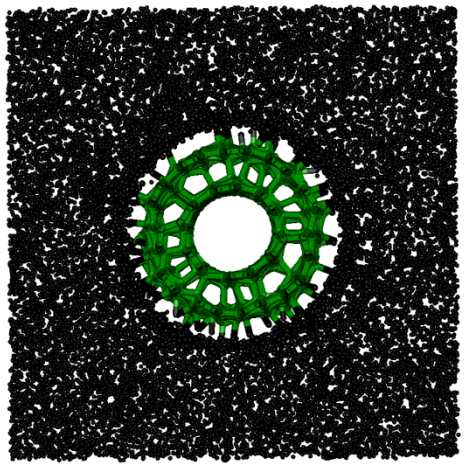

(b)

Fig. 6.1 (a) Model of a unidirectional composite with a crack approaching the interface, and (b) top view of an atomistic model of composites with an amorphous carbon matrix and a DWCNT with inter-wall sp^3 ($\rho = 0.04$). CNTs are represented by green color and matrix is black.

The molecular dynamics (MD) method was used to simulate interactions between the nanotube and matrix with the software LAMMPS (Large-scale Atomic/Molecular Massively Parallel Simulator). The interactions between atoms were calculated using an AIREBO potential [42]. With a rescale thermostat to control temperature, the equations of motion were integrated with a time step of 0.8fs. The bottom and top layer of matrix and nanotube atoms is held fixed in the z-direction (pullout direction) and unconstrained in x and y. Simulation was performed by holding the two ends as a rigid body, moving along CNT axial direction at a constant speed of ~2 m/s, achieving near equilibrium.

6.2.2 Results and Discussions

Multi-wall CNTs can have higher stiffness and strength than single-wall CNTs have if the external mechanical loads can be transferred to all the inner walls [41]. Engineering of the inter-wall coupling is possible to optimize various mechanical properties and experimental work has been done on modification of the interwall coupling in multi-wall CNTs by introducing sp^3

bonds between walls [39; 40 ; 41; 43]. Here, we investigated the effect of interwall sp^3 bond density on the failure behaviors of free-standing DWCNTs and then crack deflection/penetration in DWCNT/a-C systems. **Fig. 6.2** shows the typical stress-strain curves of free-standing pristine and sp^3 bonded DWCNTs with a sp^3 density of 0.06. The pristine nanotube fails in brittle manner while the sp^3 bonded DWCNT is more brittle.

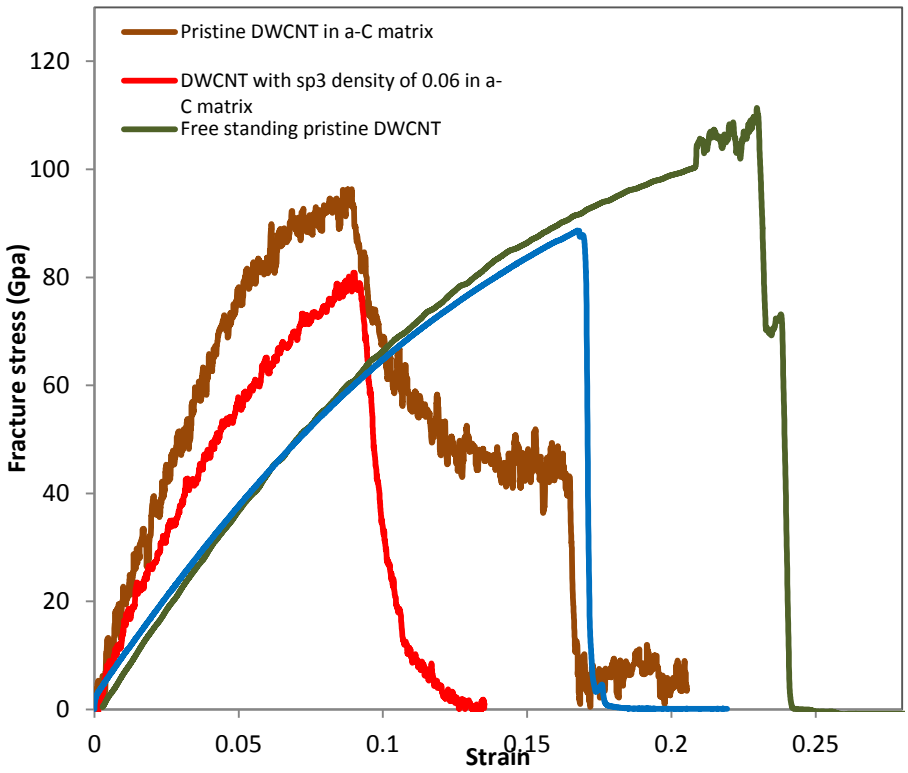

Fig. 6.2 Stress-strain curves for free-standing DWCNTs and DWCNT/a-C composites.

When CNTs are embedded into a-C matrix to form composites, sp^3 bonds can form at the a-C matrix/CNT interface. This is possible because CNTs are usually exposed to the reaction gas at elevated temperature during processing [44]. Our simulation also shows that large amount of sp^3 bonds are formed at CNT/a-C interface during treating process for a-C matrix, as shown in **Fig. 6.1**(b). Therefore, the CNT/a-C interface is strong in CNT/a-C composites. Under such

interfacial condition, bridging stress-strain curves for a CNT embedded in a-C matrix were calculated and plotted in **Fig. 6.2**. For comparison, the tensile stress is defined as the bridging force divided by CNT cross-sectional area. Two typical curves were observed for this composite system. For the composites with high density of sp^3 inter-wall bonds ($\rho = 0.06$) in the CNTs, the bridging stress increases nearly linearly with increasing strain up to a maximum value that is defined as the bridging strength, beyond the critical stress, the further increase in strain leads to a rapid decrease of stress when two walls of DWCNTs fracture at the same time. From the stress-strain dependence, this behavior can be ascribed to the typical brittle failure mechanism. In the case of a relatively low sp^3 bond density (e.g. $\rho < 0.001$), two peaks on stress-strain curves can be observed as shown in **Fig. 6.2**, one occurs when the outermost layer fractures, and the other takes place when inner layer fails. A tail of about 10MPa can also be seen on the plot (**Fig. 6.2**), which represents the pullout stress induced by the pullout of the fractured inner CNT from the outermost wall. This is a typical plastic fracture mode. In both case, no crack deflection occurs on the interface of matrix and reinforcement due to the existence of dense sp^3 bonds at the interface.

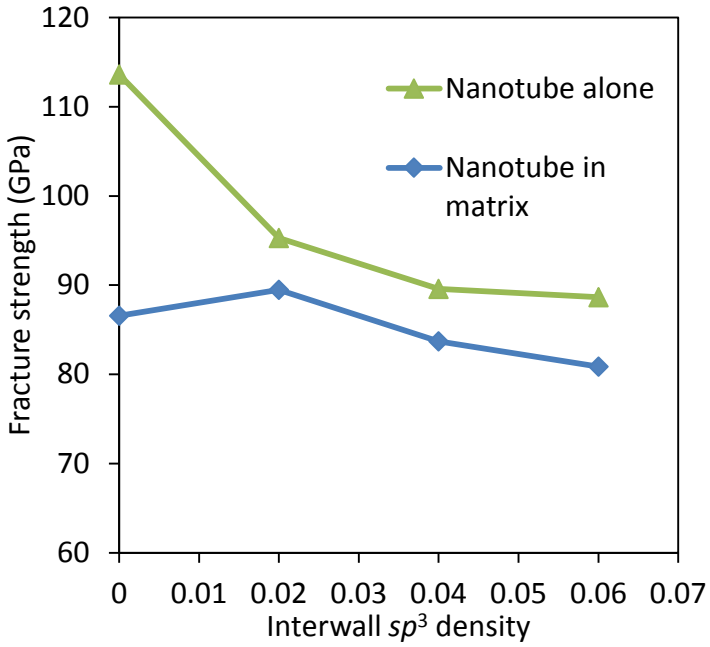

Fig. 6.3 Fracture Strength of free-standing and bridging DWCNTs versus the density of sp^3 inter-wall bonds.

Fig. 6.3 shows the tensile strength of DWCNTs versus the density of sp^3 bonds within the nanotubes for free-standing DWCNTs and those embedded in the a-C matrix. The tensile strength of the free-standing DWCNTs gradually reduces with increasing the density of sp^3 bonds and finally levels off for sp^3 density exceeding 0.02. Most free-standing DWCNTs fail near a sp^3 bond, with failure of inner and outer walls at the same position. No pullout of inner wall from outer wall was observed in the simulations. The reduction of the strength is attributed to the sp^3 bonds, which act as defects in the nanotubes. Both the inner and outer walls are weakened by the sp^3 bonds at the same position, resulting in brittle failure of the DWCNTs. However, the effect of sp^3 inter-wall bonds on the strength becomes stable after sp^3 bond density exceeds 0.02.

The bridging strength of DWCNTs in a-C matrix was calculated and also plotted in **Fig. 6.3**. For the pristine CNT reinforced a-C, the bridging strength reduces by over 20%. With

increasing sp^3 inter-wall bond density, the bridging strength slightly increases and then decreases. There is an optimal sp^3 inter-wall bond density at which the composite strength reaches a peak. Nevertheless, all the bridging strength of CNTs embedded in the matrix is lower than that for free-standing CNTs due to the stress concentration which results in premature failure of the CNTs.

Two typical fracture modes were observed in DWCNT/a-C composites, corresponding to two fracture modes described above, as shown in **Fig. 6.4**. For the composites with low or no sp^3 bond within the CNTs, after the outer wall fractures at the matrix crack, the crack deflects along the interface between the outer and inner walls. As a result, the inner wall is pulled out from the outer wall (**Fig. 6.4** (a)). In this mode, the outer wall works as sacrifice and protective layer during the processing and also during loading. This ‘‘sword-in-sheath’’ fracture mode is unique for CNT reinforced composites and has been observed experimentally in multi-wall CNT reinforced silicon nitride coatings [45]. When the sp^3 bond density reaches a certain level (here ρ >0.02), no crack deflection occurs between outer and inner walls of DWCNTs because of the sp^3 inter-wall bonds inhibit the crack propagation between CNT walls (**Fig. 6.4** (b)). In addition to the fracture modes, there is the third fracture mode in which matrix crack can deflect along the matrix/fiber interface, resulting in toughening, as observed in micro-fiber reinforced composites. Here, if it lacks of sp^3 bond existing at the CNT/a-C interface, crack may deflect along the CNT/a-C interface as well, resulting in whole CNT pullout (**Fig. 6.4** (c)), even for a high sp^3 inter-wall bond density. This type of fracture mode has also been observed in CNT reinforced alumina coatings [33]. Thus, for multiwall CNTs, the interfaces between the matrix and CNTs, as well as within the CNTs, can influence the fracture modes. Engineering these interfaces could increase both strength and fracture toughness of the nanocomposites.

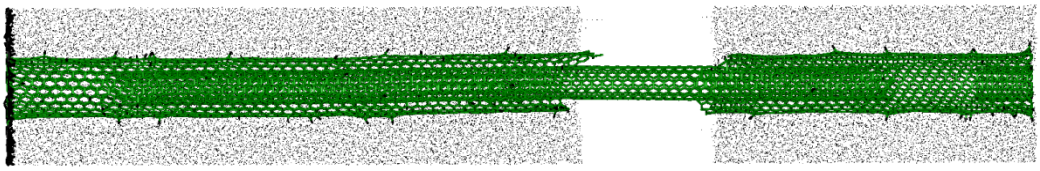

(a)

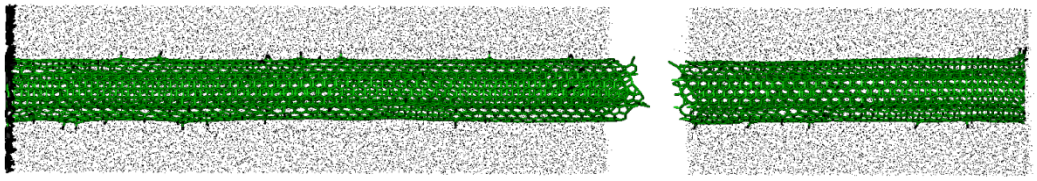

(b)

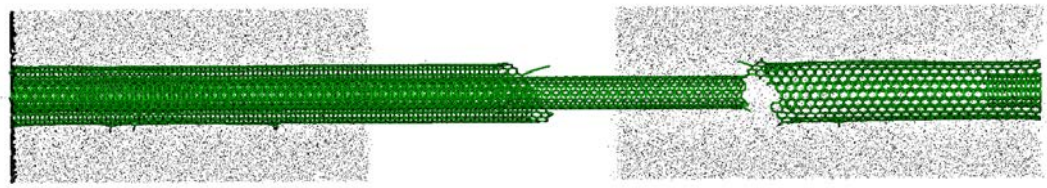

(c)

Fig. 6.4 Failure modes of DWCNT sp^3 bonds, observed in the simulations of the nanocomposites: (a) DCNT inner wall pullout from the outer wall, (b) brittle failure, and (c) DCNT outer and inner wall pullout from matrix. Green— CNT, and black— matrix.

The fracture energy was also calculated from the area under the stress-strain curves. **Fig. 6.5** shows the fracture energy for DWCNT reinforced a-C composites versus the density of inter-wall sp^3 bonds in DWCNTs. The composites with pristine CNTs show the highest fracture energy while the fracture energy of the composites rapidly decreases with increasing the sp^3 density. For example, the fracture energy for the composites with a sp^3 density of 0.04 is almost twice lower than those without sp^3 bond. Obviously, this rapid reduction in fracture energy is attributed to the density of sp^3 bonds within the CNTs, which causes the transition of failure from tough to brittle modes. From the simulation, two toughening mechanisms were identified,

namely, crack deflection and CNT pullout. Although the CNT/a-C matrix interface is strong due to the existence of dense sp^3 bonds at the CNT/a-C interface, crack deflection can still occur within the DWCNTs for low inter-wall sp^3 bond density. With increasing the sp^3 density in DWCNTs, possible sp^3 location will be closer to the matrix crack. Since sp^3 bonds are defects to the inner walls, stress concentration will build up around the defects during loading. The inner walls will break at the sp^3 bond close to the matrix crack, leading to short CNT pull-out, lowering the fracture energy. Overall, it is necessary to keep the sp^3 bond density at about 0.001 to achieve high strength and toughness for CNT/a-C composites.

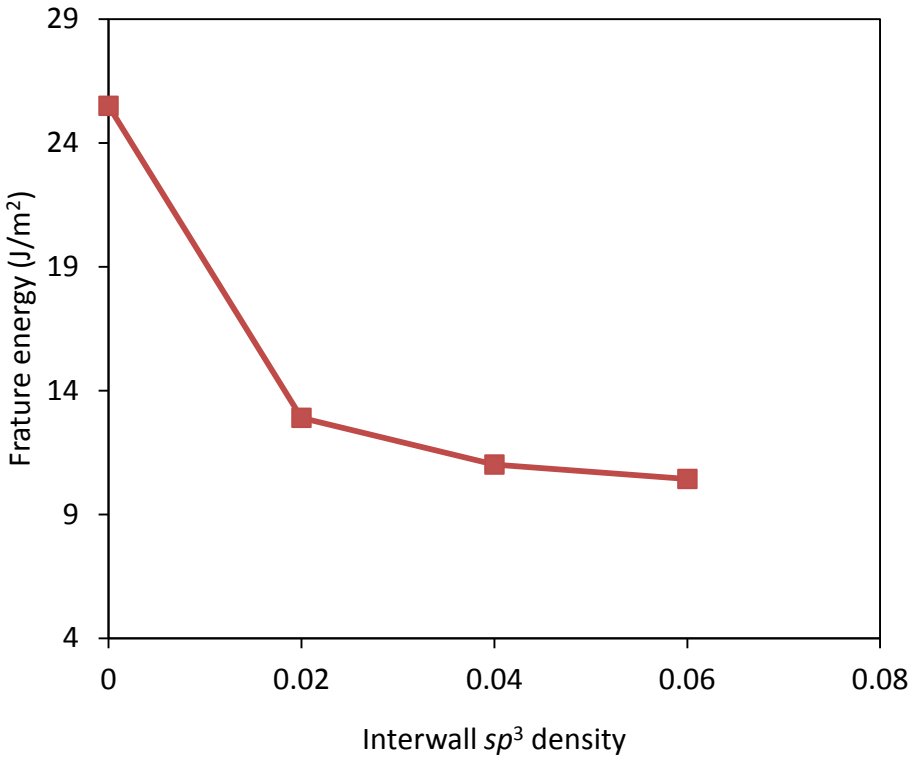

Fig. 6.5 Fracture energy of composites versus the density of sp^3 inter-wall bonds.

6.3 Mechanical Properties of Junction in 3D CNT-graphene Nano Architecture via QM/MD Method

3D nanostructures were produced in laboratory in the presence of metal catalysts [1-2]. The growth of junction of 3D carbon nanotube-graphene was also simulated via quantum mechanical molecular dynamic method, providing specific theoretic foundations for the experimental effort to fabricate the new 3D structures [4]. However, most 3D nanostructures were fabricated with aid of metal particle catalysts, in which the metal particles remain in the junction structure even after subsequent treatments. Therefore, understanding of mechanical properties and stability of the 3D nanostructures with metal particles is necessary for their applications. Simulation work has been done on mechanical property of large scale of pure C-C bonded CNT-graphene structure [5-7], most of which, however, were focused on CNT density and lengths selected as the main influential variables, with the assumption of prefect junctions. Obviously, junctions are the key elements in the 3D structures and metal particles at the junctions would strongly affect the junction performance. Thus, the strength of junctions with metal particle would be of significance for the whole 3D nanostructure and needs more consideration.

Furthermore, quantum mechanical molecular dynamic method was utilized to simulate the mechanical properties of as-grown C-C junctions as well as the junctions with metal particles embedded inside them.

6.3.1 Computational Methodology

The tensile strength of pure C-C junctions and those with catalysts was calculated with quantum mechanical molecular dynamic software SCC-DFTB+ (self-consistent-charge Density

Functional Tight Binding)[8-14]. In the computation, Noose Hoover thermostat was utilized to perform all the activities of atoms with timestep of 1 fs. The tensile test was done at room temperature (300k). In laboratory, Fe and Ni are usually used as catalysts to grow carbon nanostructure; hence deformation of the junctions with different metal catalysts –Fe and Ni— was calculated. We tested three types of junctions: seamless C-C bond junctions (**Fig. 6.6** (a)), the junctions embedded with particles between CNT and graphene (C-Fe-C or C-Ni-C junctions; **Fig. 6.6** (b)) and the junctions with particle embedded inside CNT (**Fig. 6.6** (c)). All the models consists of a (5, 5) armchair CNT and single hexagonal graphene with an edge length of 1 nm. The graphene sheet was drilled out a hole of 0.65 nm, and CNT was placed above the nanoparticle and graphene. The outlining boundaries of CNT and graphene were saturated by hydrogen atoms. Nanoparticle size varies with different metals. The total number of the atoms in the simulation is around 250-290. For comparison, single CNT, graphene and as-grown C-C junctions made in the process simulations were also tested. The saturated H atoms on graphene was fixed during the simulations, and tensile test was performed by holding the H atoms and fist top ring of CNT, moving along CNT axial direction at a constant speed of 0.0125 nm/ps.

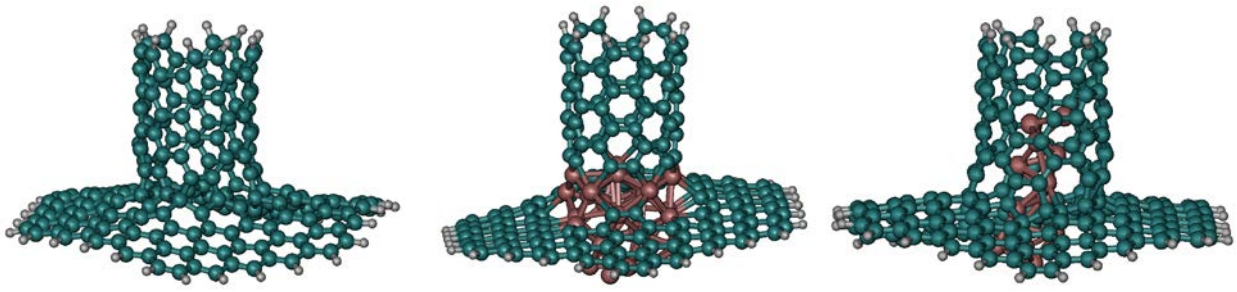

(a) (b) (c)

Fig. 6.6 Models for tensile testing of the junctions: (a) A pure C-C bonded junction, (b) A junction with Fe particle between CNT and graphene, and (c) A junction with Fe particle embedded in it. (Green represents C atoms, white is referred to H atoms; and pink represents Fe atoms)

6.3.2 Results and Discussions

Carbon nanotubes with C-C sp^2 hybrids bonds are believed to be one of the strongest materials, with tensile strength of 85-118 GPa [15]. Pristine graphene, with similar C atoms arrangement to CNT, was reported to possess fracture strength of 100-126 GPa[16]. With such high strength, mechanical properties of the 3D nanostructure composed of graphene and vertical CNT will strongly depend on the quality of their junctions. It has been shown from the simulations [4,17,18] and experiments[2, 19, 20] that CNT-graphene junctions could be pure C-C covalent, metal-C bonds or the mixtures of them. Here, we calculated the tensile strength of the as-grown CNT-graphene junctions described in section 3.1, as well as those with embedded metal nanoparticles (remaining catalysts) as simulated in our previous work[4].

Stress-strain curves of various junctions as well as pristine (5, 5) armchair CNTs are shown in **Fig. 6.7**. For the CNTs, the stress increases nearly linearly with increasing strain, but drops after reaching a maximum value that is defined as the tensile strength. From the stress-strain dependence, this behavior can be ascribed to the typical brittle failure mechanism, as simulated by others [15, 21]. In contrast, the pure C-C junction and the junctions with embedded Fe and Ni particles show relatively ductile fracture modes according to the stress-strain curves. For the covalent C-C junction, the ductile fracture stems from the compliant of graphene with out-of-plane deformation since graphene is fixed at its edge during loading. In the case of particle-embedded junctions, the ductile deformation can be attributed to the deformation of complaint graphene as well as the metallic particles.

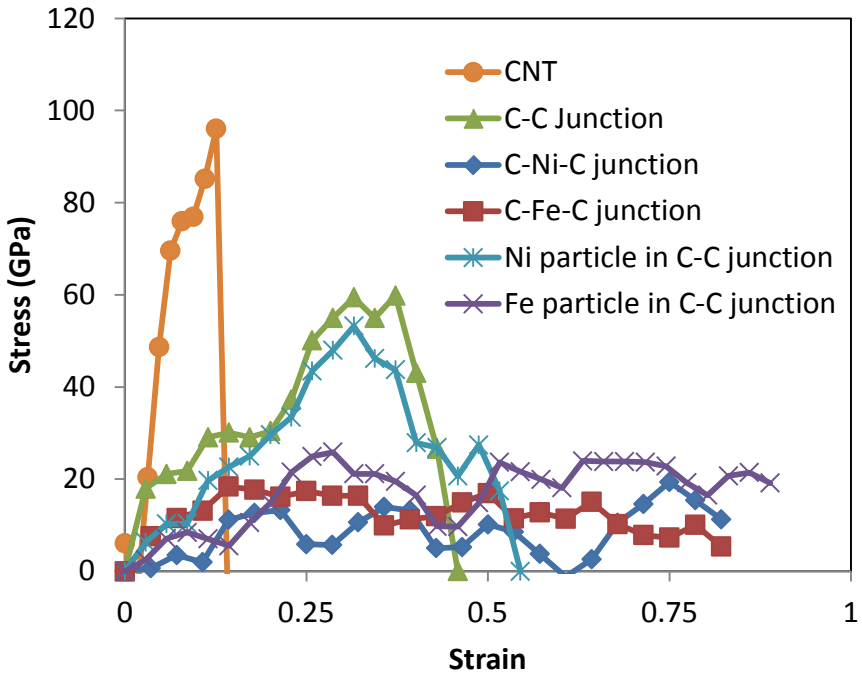

Fig. 6.7 Stress-strain curves for single-wall CNT, 3D C-C junction, junctions with Fe/Ni particles embedded between CNT and graphene (C-Fe-C and C-Ni-C junctions), and C-C junctions with Fe/Ni particles embedded in CNT.

Tensile strength of pure C-C junction is relatively lower than that of perfect CNTs. The lower strength is attributed to the existence of heptagons, pentagons, quadrangle at the junction area, which are considered as local defects. It was reported that for defective CNTs, the fracture strength reduces by ~9% for a Stone-Wales defect and ~26% for an atom vacancy [22]. Compared to pure C-C junction, tensile strength of metal-C junctions was further decreased by the metal particles embedded between CNT and graphene (**Fig. 6.6** (a)), even when metal particles are embedded within the junction and there are C-C bonds between CNT and graphene (**Fig. 6.6** (b)).

6.3.2.1 Tensile Test of Single Wall Carbon Nanotube, Single Layer Graphene, and C-C 3D Junction

Single wall carbon nanotube was tensile tested first. One end of CNT was fixed and the other end moved along CNT axial direction at a constant speed of 0.0125 nm/ps (Fig. 6.8 (a)). As strain increased, CNT elongated and C-C bonds was stretched (**Fig.** 6.8 (b)), and CNT fractured as the C-C could not sustain the continuous stretching (**Fig.** 6.8 (c)). Single wall carbon nanotube fractured in brittle behavior, which also can be observed from the stress-strain curve in **Fig.** 6.7. The fracture strength is around 90~100 GPa, agreeing with experimental measurements.

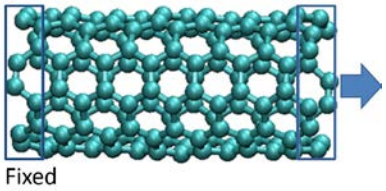

(a) $\varepsilon = 0\%$

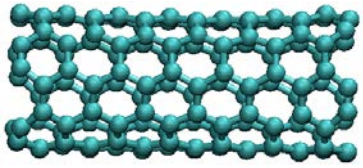

(b) $\varepsilon = 6.29\%$

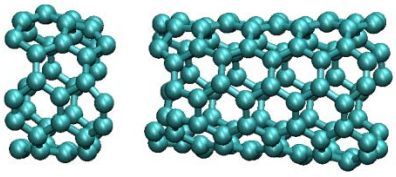

(c) $\varepsilon = 14.2\%$

Fig. 6.8 Atomic configurations of fractured single wall CNT: (a) pristine single wall CNT, (b) CNT elongated during pullout, and (c) CNT fractured.

Single layer graphene tensile test was carried out in a similar way: one edge of graphene was fixed and the other edge moved along the arrow direction in **Fig. 6.9** (a) at a constant speed

of 0.0125 nm/ps. Graphene elongated with increasing strain (**Fig. 6.9** (b)), and the graphene fractured as tensile strain is 13.6% (**Fig. 6.9** (c)). The graphene fractured also in brittle behavior, and stress-strain curve is given in **Fig. 6.10**, which shows that relationship between stress and strain is almost linear. Graphene fractured when its tensile deformation was elastic and the curve does not include a yield point and strain-harden region. The fracture strength obtained from quantum mechanical/molecular dynamic method is about 100 GPa, which is close to the fracture strength of pristine CNT, because both of them are composed with covalent C-C sp^2 bonds with different dimensional arrangements.

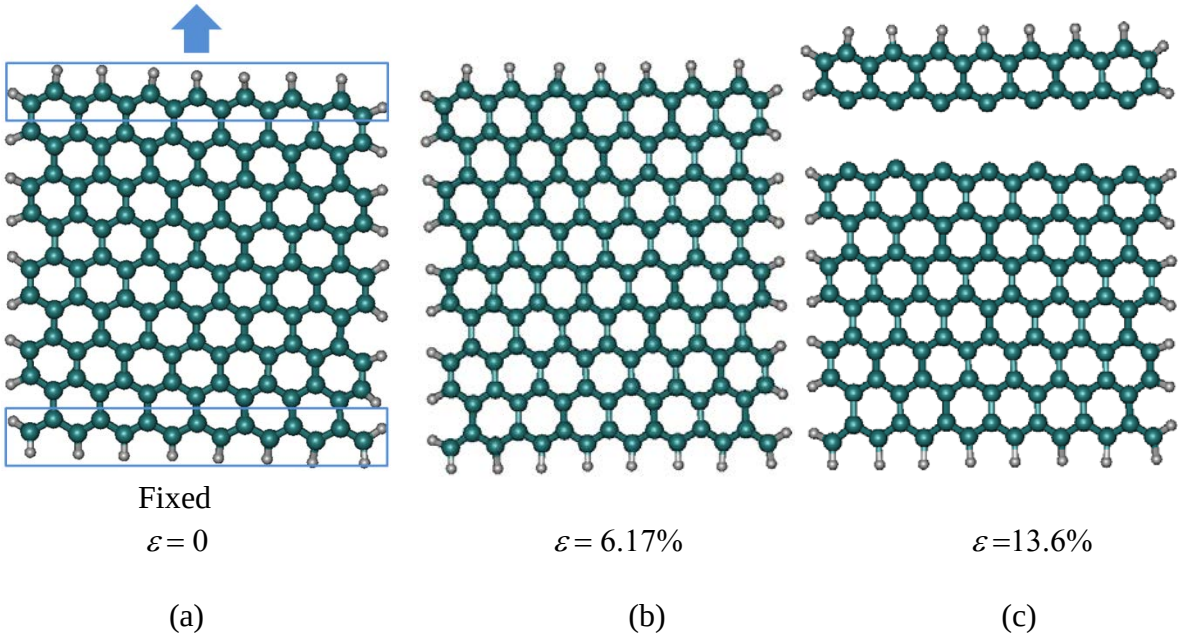

Fig. 6.9 Atomic configurations of fractured single layer graphene: (a) pristine single layer graphene, (b) graphene elongated during pullout, and (c) graphene fractured.

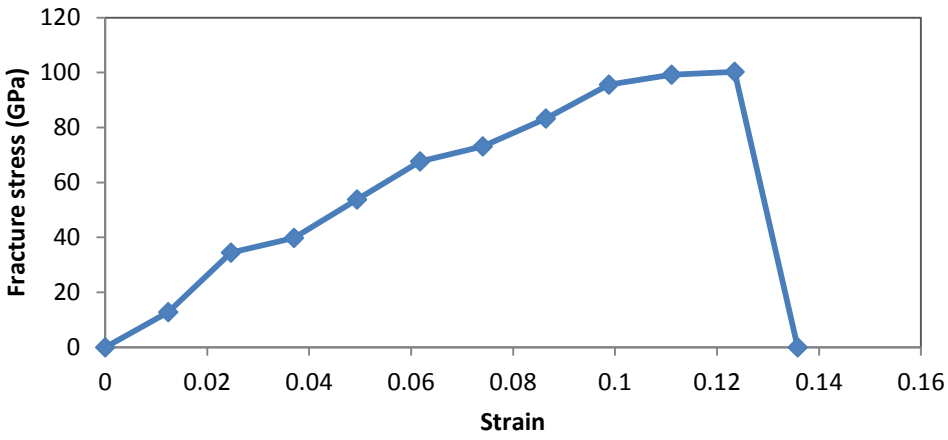

Fig. 6.10 Stress-stain curve of single layer graphene sheet.

Fig. 6.11 gives the atomic configuration of pure C-C bonded junction. Graphene was drilled out a hole of 0.65 nm in the center with plenty of unsaturated carbon atoms left, and then the open end of CNT could bond to graphene through them. As grow pure C-C bond junction is shown in **Fig. 6.11** (a), which is completely relaxed and reaches its equilibrium state. With increasing tensile strain, the junction is elongated and C-C bonds are stretched. In **Fig. 6.11** (b), first C-C bond is broken as highlighted in red circle. Then as all the C-C bonds at the transition region between graphene are broken, the junction fractured **Fig. 6.11** (c). The fracture strength is lower than that of pristine CNT due to the pentagons, heptagons at the transition region, which are typical defects in carbon materials.

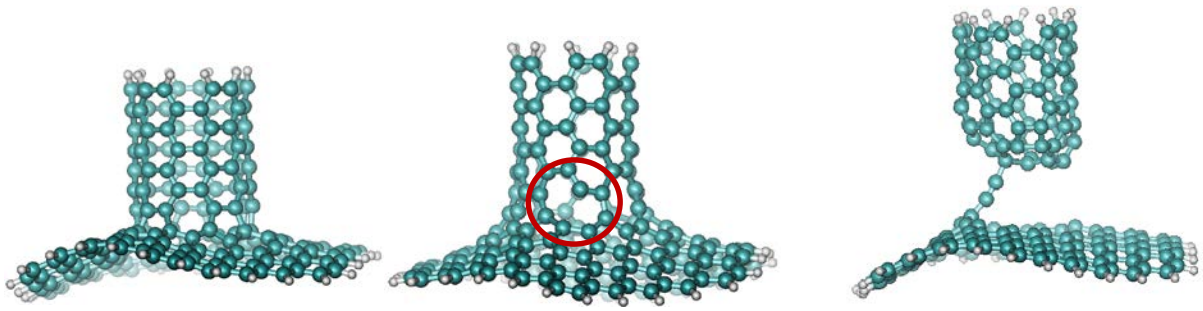

$\varepsilon = 0$ $\varepsilon = 23.5\%$ ε =47.2%

(a) (b) (c)

Fig. 6.11 Atomic configurations of pure C-C bonded junction: (a) pure C-C bonded junction, (b) junction elongation, and (c) fractured junction. (Green represents C atoms, white is referred to H atoms; and blue represents Ni atoms)

6.3.2.2 Tensile Test of Junctions with Metal Particle Embedded between CNT and Graphene

When the metal particles are embedded between the CNT and graphene, the deformation of the junction obviously depends on the particle and metal-C bonds. **Fig. 6.12** gives typical pullout procedure of junction with Ni particle embedded between CNT and graphene. Ni particle bonds to unsaturated CNT end and graphene dangling bonds caused by hole after relaxation (**Fig. 6.12** (a)). Ni-C bonds are relatively stronger than Ni-Ni bonds, since throughout the pullout, Ni-C bonds did not fracture at all, instead the Ni particle was informing. The Ni particle elongated with increasing strain (**Fig. 6.12** (b)), and finally the junction fractured at the position of the Ni necking (**Fig. 6.12** (c)).

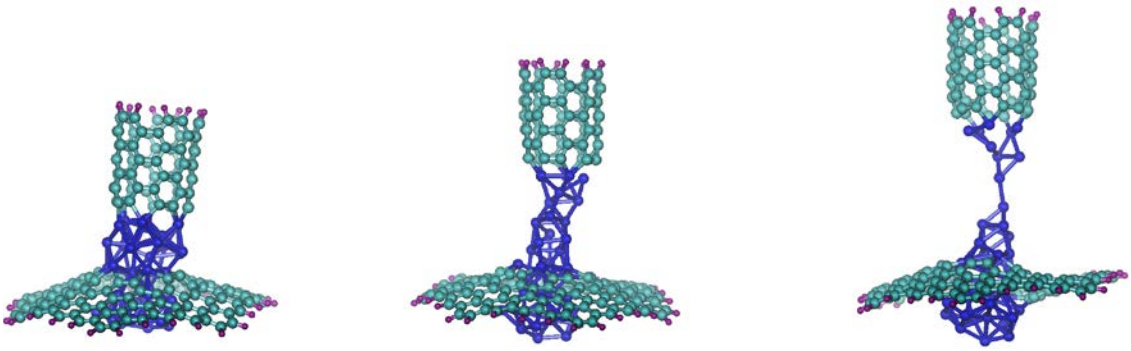

ε = 0% ε =61.9% ε = 73.7%

(a) (b) (c)

Fig. 6.12 Atomic configurations of fractured junctions with Ni particle embedded between CNT and graphene: (a) Ni particle-embedded between CNT and graphene, (b) particle elongation, and (c) fractured junction. (Green represents C atoms, purple is referred to H atoms; and blue represents Ni atoms)

The deformation of the junction with Fe particle embedded between CNT and graphene is similar to that of junction with Ni particle embedded between CNT and graphene. Fe nanoparticle bonded to unsaturated CNT end and graphene dangling bonds after completely relaxation (**Fig. 6.13** (a)). Fe-C bonds are relatively stronger than metal bonds, since Fe-C bonds did not fracture at all, and instead the Fe particle was informing during pullout. The Fe particle elongated with increasing strain (**Fig. 6.13** (b)), and finally the junction fractured at the position of the Fe particle necking (**Fig. 6.13**(c)).

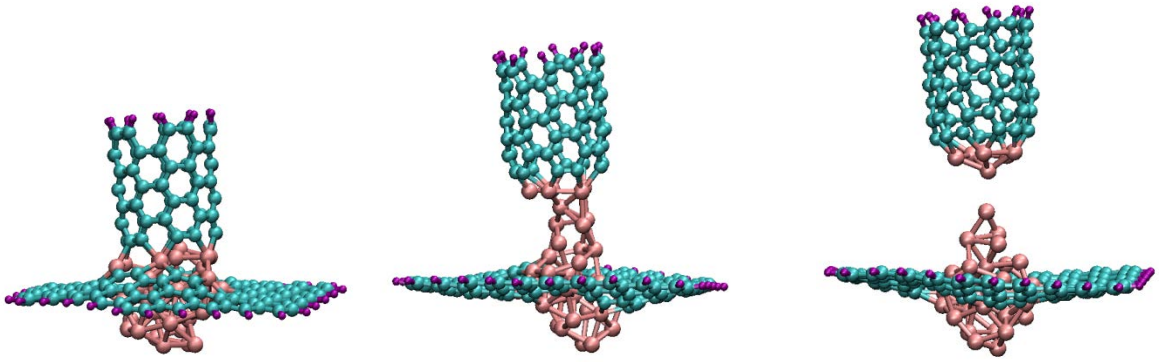

ε = 0% ε = 41.3% ε = 64.9%

Fig. 6.13 Atomic configurations of fractured junctions with Fe particle embedded between CNT and graphene: (a) Fe particle-embedded between CNT and graphene, (b) particle elongation, and (c) fractured junction. (Green represents C atoms, purple is referred to H atoms; and pink represents Fe atoms)

The fracture behaviors indicate that for junctions with metal embedded between CNT and graphene, metal particles are the weakest part, weakening the mechanical properties of the junction.

6.3.2.3 Tensile Test of Junctions with Metal Particle Embedded within C-C Bonded Junctions

For the junctions with metal particle embedded in the junction (**Fig. 6.14**(a)), the C-C bonds of the junction are weakened by the embedded particles. As a result, the C-C bonds prematurely break due to the existence of the nanoparticles, as shown in **Fig. 6.14** (b), which is the junction with Fe nanoparticle embedded within junction. After the C-C bonds at the junction are broken, the fracture mode is very similar to those junctions with metal particles embedded between the CNT and graphene, as shown in **Fig. 6.14** (c)-(d).

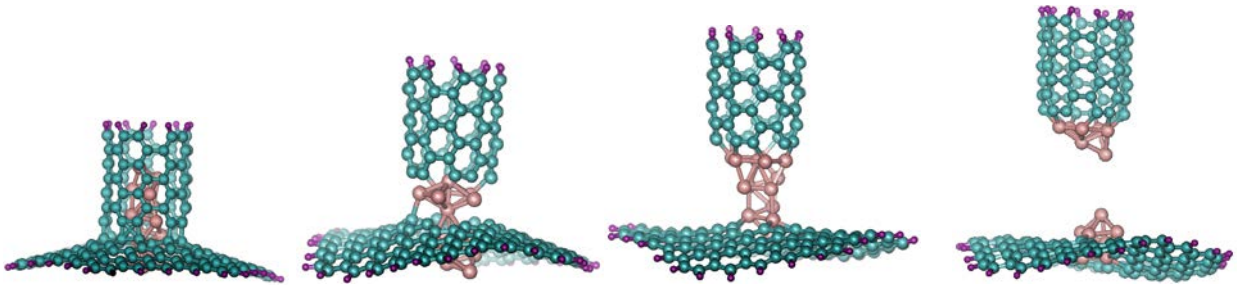

ε = 0% ε = 18.0% ε = 32.4% ε = 57.6%

(a) (b) (c) (d)

Fig. 6.14 Atomic configurations of fractured junctions with Fe particle embedded within the C-C bonded junctions: (a) Fe particle-embedded junctions, (b) junction with broken C-C bonds, (c) particle elongation, and (d) fractured junction.

To find weakening effect of metal-C bond on the junction mechanical properties, we did tensile test on junction with small quantity of Ni-C bonds (**Fig. 6.15** (a)). In this model, the Ni particle embedded within the junction, but the Ni particle is not completely embraced by junction with a part hanging out of junction. Ni-C bonds only exist between graphene and Ni nanoparticle. Obviously, the fracture behavior seems the same with the pure C-C junction. The junction firstly break at the transition region (**Fig. 6.15**(b)) and fractured finally (**Fig. 6.15** (c)). However, the fracture strength is almost 10 GPa smaller than that of C-C junction, which can be read from stress-strain curve (**Fig. 6.7**). Therefore, the metal-C bonds significantly reduce mechanical properties of C-C junction, and it is important to control the catalyst sizes and locations in the 3D structure growth process.

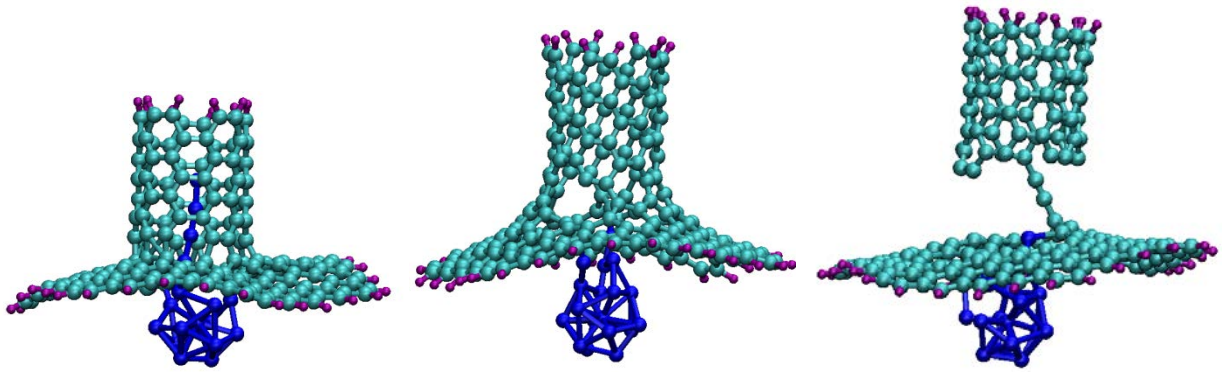

ε = 0% ε = 35.4% ε = 50.1%

(a) (b) (c)

Fig. 6.15 Atomic configurations of fractured junctions with small number of Ni-C bonds: (a) Ni particle hanging out junctions, (b) junction with broken C-C bonds, (c) fractured junction. (Green represents C atoms, purple is referred to H atoms; and blue represents Ni atoms)

6.3.2.4 Fracture Energies of 3D Junctions

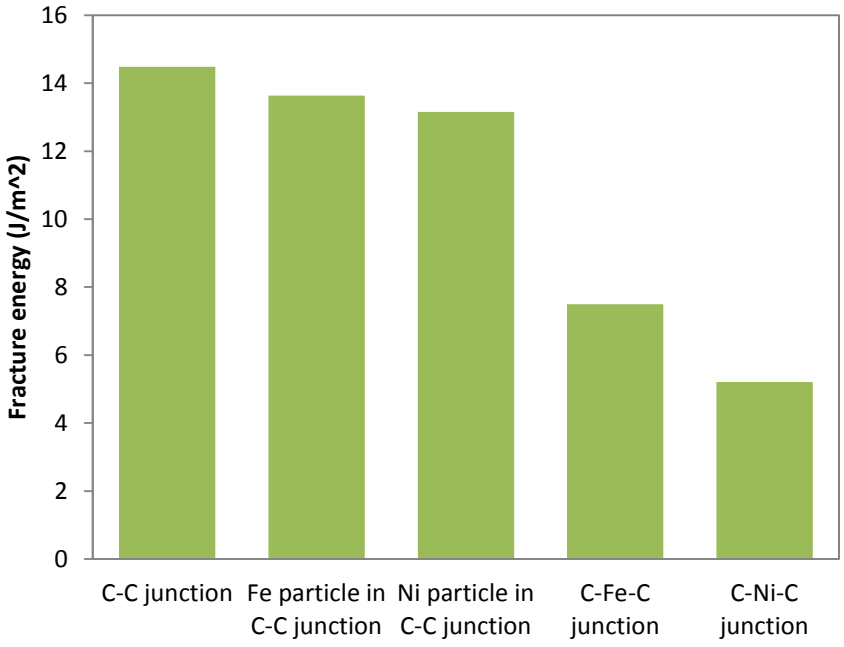

Fig. 6.16 Fracture energy of pure C-C junction and the junctions with embedded metal particles.

The fracture energy was also calculated from the area under the stress-strain (σ-ε) curves, shown in **Fig. 6.16**. The pure C-C bonded junctions have the highest fracture energy among the junctions. Metal particles can noticeably reduce fracture energy of the 3D junctions, depending on the particle embedding configurations. Fracture energy reduces by more than 50% as metal particles are embedded between the CNT and graphene, while it decreases slightly as metal particle is inside of junction for Fe and Ni particles. Obviously, the junction without metal particle has the highest tensile strength and ductility due to pure C-C covalent bonds. Thus, mechanical properties and deformation behavior of 3D nanostructure are strongly affected by remaining catalysts after junction growth, and it is necessary to remove the catalysts after the synthesis of the new 3D nanostructure or grow pure C-C bonded junctions without catalysts. As shown in Section 3.1, the high-quality single-layer CNT-graphene junctions could be grown on Cu template without catalysts, providing an effective route to create 3D CNT-graphene nanostructures with seamlessly C-C bonded junctions.

6.4 Mechanical Property Investigations on Filleted Junctions via Molecular Dynamic Methods.

Filleted junctions with different fillet angles have grown in chapter 5. MD results have proven 135° fillet junctions are naturally formed because of the minimum energy required to form the junctions. Generally in mechanical engineering, fillets are popular when two individual components are welded together. For the junction of 3D nano structures, the vertical CNT and parallel graphene form a right angle, which can cause stress concentrations and lower durable of mechanical loading. In this situation, a fillet is necessary at the exterior corner whose extensive area can share stress concentrations. Tensile strengths of different filleted junctions were calculated with MD methods.

6.4.1 Computational Methodology

The molecular dynamics (MD) method was used to simulate interactions of 3D junctions. The interactions between atoms were calculated using an AIREBO potential [42], with a modified cutoff scheme [46]. With a rescale thermostat to control the temperature, the equations of motions were integrated with a time step of 0.25 fs. The outline of bottom layer of the junction is held fixed in the z-direction (pullout direction). Simulations were performed by holding the several carbon rings of the CNT right-end as a rigid body, moving along CNT axial direction at a constant speed of ~4 m/s, achieving near equilibrium. Pullout model is shown in **Fig. 6.17**.

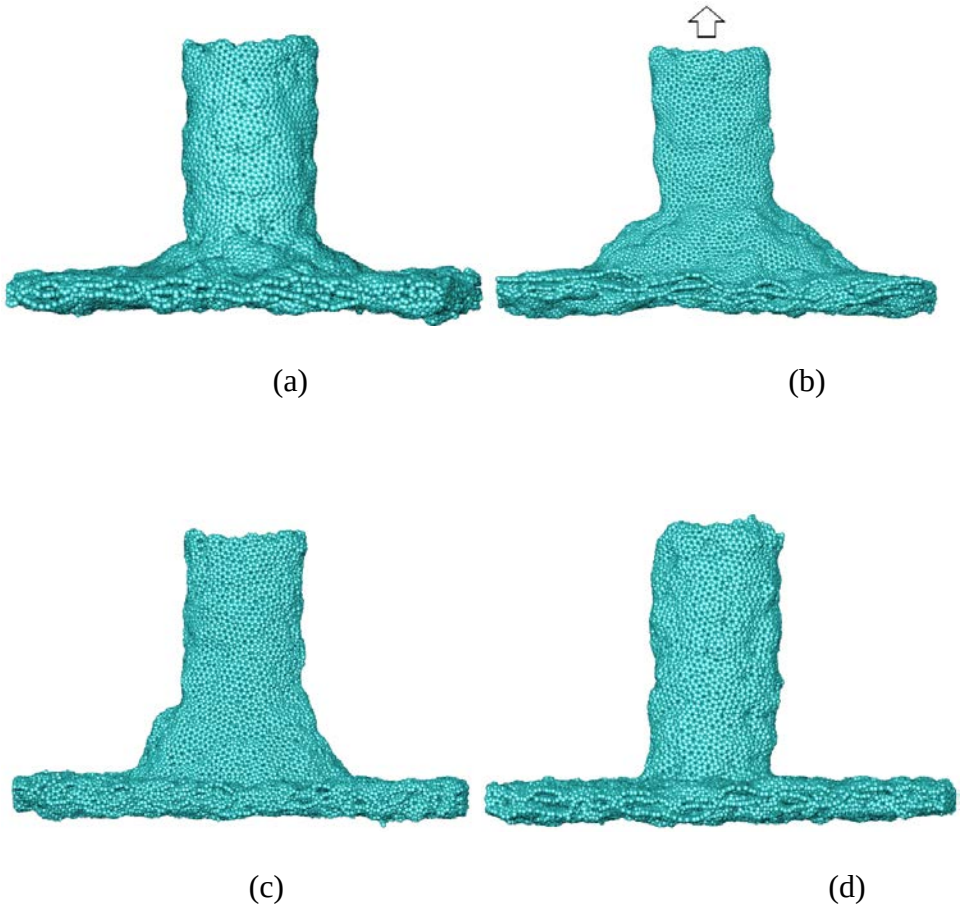

Fig. 6.17 Side view of atomistic models of 3D CNT-graphene filleted junctions. (a) A 120° filleted junction, (b) a 135° filleted junction, (c) a 150° filleted junction and (d) a 180° (90°) filleted junction.

6.4.2 Results and Discussion

Fracture strengths for different fillet angle junctions were obtained through pullout tests, and they are consistent with values reported before [47]. **Fig. 6.18** gives the stress-strain curves for filleted junctions. The relationship between stress and strain is almost linear, indicating a brittleness behavior. Junctions with 120°, 135°, 150°, and 90° (180°) fillet angles break in similar behaviors. The junction with 135° fillet angle has the biggest fracture strength compared with other fillet angle junctions, as shown in **Fig. 6.19**, indicating its most stable mechanical behaviors. It also corresponds to the fact that the 135^0 filleted junction has the lowest formation potential energy as discussed in chapter 5. The fracture behavior is shown in **Fig. 6.20**. All filleted junction break at the CNT area, where local defects and stress concentration exit.

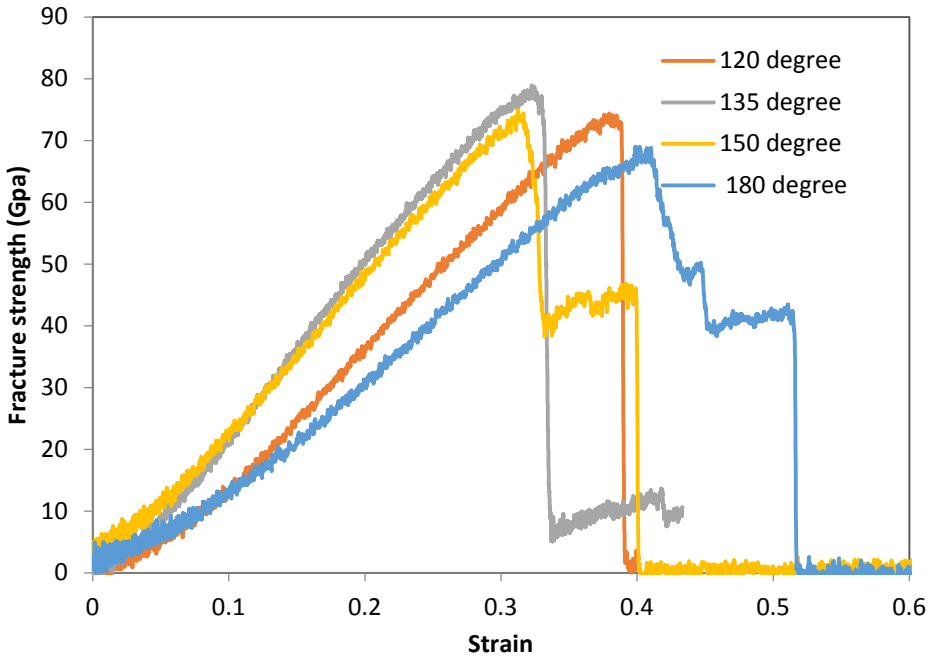

Fig. 6.18 Stress-strain curves for filleted junctions.

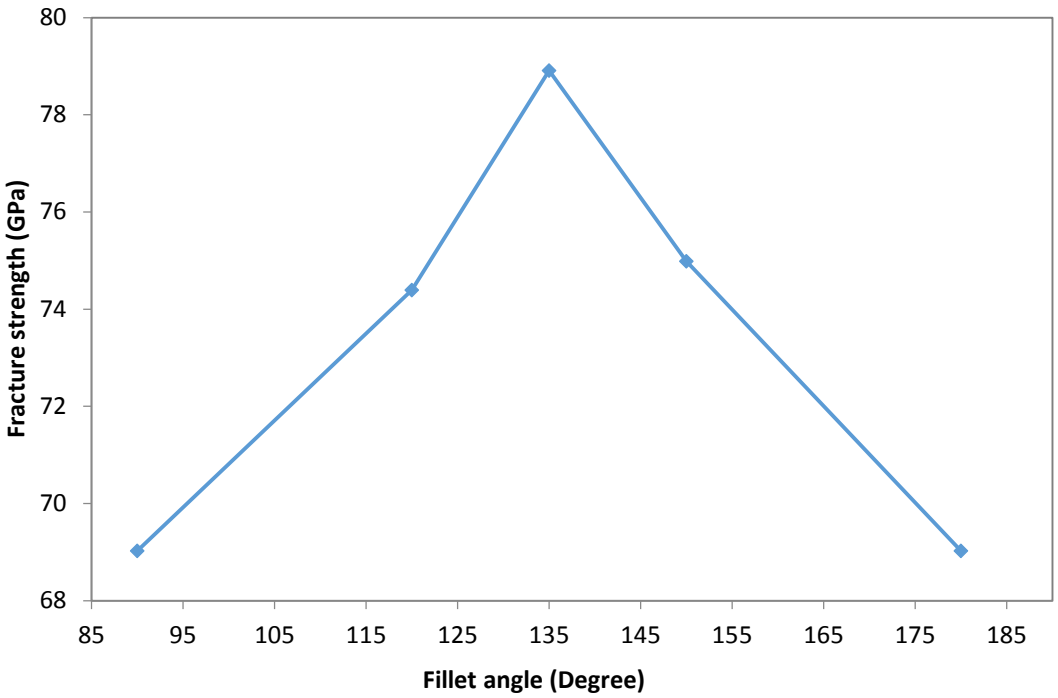

Fig. 6.19 Fracture strengths for various fillet angle junctions.

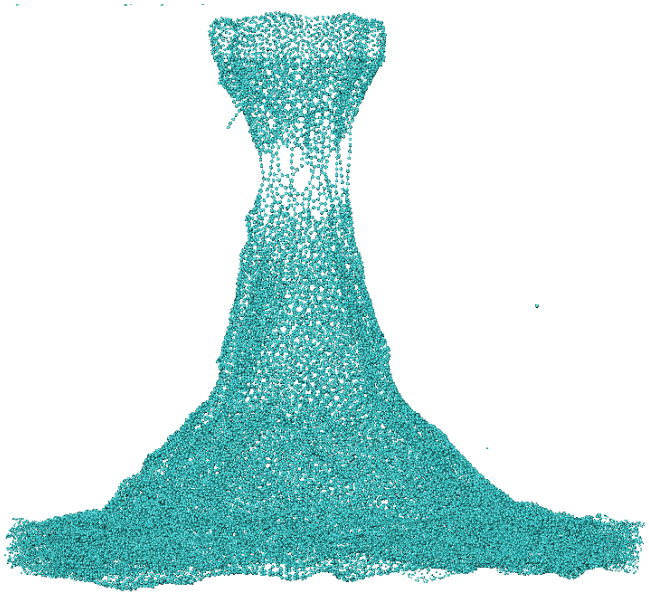

Fig. 6.20 Junction fracture snap shot.

6.5 Conclusions

(1) Molecular dynamics simulations were performed to study the crack deflection/penetration at the interfaces of DWCNT/a-C composites. The density of sp^3 bonds strongly affects the bridging strength and fracture energy. For weak interface and pristine DWCNTs, matrix crack can deflect along the interface between outermost layer and matrix as well as the interfaces between the walls within the DWCNTs. For relatively strong CNT/matrix interface, matrix crack can deflect within the DWCNTs, resulting in toughening. A strong interface and relatively dense sp^3 inter-wall bonds leads to brittle failure of the composites. Engineering these interfaces could increase both strength and fracture toughness of the nanocomposites. Our results suggest that material design direction – the nanocomposites can be toughened by using outermost wall of CNTs as a sacrificial layer and introducing sp^3 bonds in the CNTs.

(2) Tensile tests of pristine CNT and graphene were simulated via quantum mechanical molecular dynamic method. Both of them fractured in brittle behavior, and fracture strengths agree with experimental measures, guaranteeing accurateness of calculations. Tensile tests of different types of junctions in 3D nanotube – graphene nanostructures were simulated via quantum mechanical molecular dynamic method. The simulations show that the covalently C-C bonded junctions possess the highest fracture strength and fracture energy. The metal nanoparticles embedded in the junctions between the CNT and graphene significantly reduce the fracture strength and energy. Even when the metal particles are embedded inside junction, the C-C bonded junctions are weakened by the particles.

(3) Filleted junctions fracture in brittle behaviors, and the 135° filleted junction is the strongest junction among the 90°, 120°, 150°, and 180° filleted junctions. It could be proposed that the 135^0 filleted junction is the preferred formed structure in experiments.

6.6 References

[1] J. Lin, C. Zhang, Z. Yan, Y. Zhu, Z. Peng, R. H. Hauge, D. Natelson, J. M. Tour, Nano Lett. 13 (2013) 72.

[2] M. Zhao, X. Liu, Q. Zhang, G. Tian, J. Huang, W. Zhu, F. Wei, ACS NANO 6 (2012) 10759.

[3] J. Wen, Y. Li, W. Yang, Vacuum 101 (2014) 271.

[4] J. Niu, M. Li, W. Choi, L. Dai, Z. Xia, CARBON 67 (2014) 627.

[5] S. Sihn, V. Varshney, A.K. Roy, B.L. Farmer, CARBON 50 (2012) 603–611.

[6] S. Sihn, V. Varshney and A. K. Roy, 51st AIAA/ASME/ASCE/AHS/ASC Structures, Structural Dynamics, and Materials Conference
18th 12 - 15 April 2010, Orlando, Florida.

[7] F.D. Novaes, R. Rurali, P. Ordejon, ACS NANO 4 (2010) 7596.

[8] http://www.dftb.org/

[9] A.J. Page, Y. Ohta, S. Irle, K. Morokuma, Acc. Chem. Res. 43 (2010) 1375-1385.

[10] Y. Ohta, Y. Okamoto, S. Irle, K. Morokuma, CARBON 47 (2009) 1270.

[11] Y. Ohta, Y. Okamoto, A. J. Page, S. Irle, K. Morokuma, ACS NANO 3 (2009) 3413.

[12] A.J. Page, H. Yamane, Y. Ohta, S. Irle, K. Morokuma, J. Am. Chem. Soc. 132 (2010) 15699.

[13] A.J. Page, S. Minami, Y. Ohta, S. Irle, K. Morokuma, CARBON 48 (2010) 3014.

[14] A.J. Page, S. Irle, K. Morokuma, J. Phys. Chem. C 114 (2010) 8206.

[15] T. Belytschko, S.P. Xiao, G.C. Schatz, R. Ruoff, Phys. Rev. B 65 (2002) 235430.

[16] M.C. Wang, C. Yan, L. Ma, N. Hu, M.W. Chen, Comput. Mater. Sci. 54 (2012) 236.

[17] J. Park, V. Prakash, J. Mater, Res. 28 (2013) 940.

[18] D. Baowan, B. J. Cox, J. M. Hill, CARBON 45 (2007) 2972.

[19] Z. Yan, L. Ma, Y. Zhu, I. Lahiri, Z. Liu, M. G. Hahm, S. Yang, C. Xiang, W. Lu, Z. Peng, Z. Sun, J. Lou, W. Choi, P.M. Ajayan, J.M. Tour, Acs Nano 7 (2013) 58.

[20] Y. Zhu, L. Li, C. Zhang, G. Casillas, Z. Sun, Z. Yan, G. Ruan, Z. Peng, A.R.O. Raji, C. Kittrell, R. H. Hauge, J. M. Tour, Nature commu. 3 (2012) 1225.

[21] M.B. Nardelli, B.I. Yakobson, J. Bernholc, PRL 81 (1998) 4656.

[22] S.L. Mielke, D. Troya, S. Zhang, J. Li, S. Xiao, R. Car, R.S. Ruoff, G.C. Schatz, T. Belytschko, Chem. Phys. Lett. 390 (2004) 413.

[23] O. Wilhelmsson, M. Råsander, M. Carlsson, E. Lewin, B. Sanyal, U. Wiklund, O. Eriksson, U. Jansson, Adv. Funct. Mater. 17 (2007) 1611.

[24] T. Zehnder, J. Matthey, P. Schwaller, A. Klein, P.-A. Steinmann, J. Patscheider, Surf. Coat. Technol. 163 (2003) 238.

[25] Y.T. Pei, D. Galvan, J.Th.M. De. Hosson, A. Cavaleiro, Surf. Coat. Technol. 198 (2005) 44.

[26] H. Schittenhelm, D.B. Geohegan, G.E. Jellison, A.A. Puretzky, M.J. Lance, P.F. Britt, Appl. Phys. Lett. 81 (2002) 2097.

[27] X.T. Zhou, X.M. Meng, F.Y. Meng, Q. Li, I. Bello, W.J. Zhang, C.S. Lee, S.T. Lee, Y. Lifshitz, Diam. Relat. Mater. 12 (2003) 1640.

[28] M. Stüber, H. Leiste, S. Ulrich, H. Holleck, D. Schild. Surf. Coat. Technol. 150 (2002) 218.

[29] M.Y. He, J.W. Hutchinson, Int. J. Solids Structures 25 (1989) 1053.

[30] N.J. Pagano, H.W. Brown III, Composites, 24 (1993) 69.

[31] B.K. Ahn, W.A. Curtin, T.A. Parthasarathy, R.E. Dutton, Compos. Sci. Technol. 58 (1998) 1775.

[32] E. Martin, P.W.M. Peters, D. Leguillon, J.M. Quenisset, Mater. Sci. Eng. A 250 (1998) 291-302.

[33] Z. Xia, L. Riester, W.A. Curtin, H. Li, B.W. Sheldon, J. Liang, B.Chang, J.M. Xu, Acta Mater. 52 (2004) 931.

[34] L. Li, J.B. Niu, Z. Xia, Y. Yang, J.Y. Liang, Scripta Mater. 65 (2011) 1014.

[35] L. Li, Z. Xia, W.A. Curtin, Y. Yang, J. Am. Ceram. Soc. 92 (2009) 2331.

[36] S. Namilae, N. Chandra, Comp. Sci. Tech. 66 (2006) 2030.

[37] G. Kopidakis, I.N. Remediakis, M.G. Fyta, P.C. Kelires, Diam. Relat. Mater. 16 (2007) 1875.

[38] D.S. Grierson, R.W. Carpick, Nano. Today 2 (2007) 12.

[39] B. Peng, M. Locascio, P. Zapol, S.Y. Li, S.L. Mielke, G.C. Schatz, et al., Nat. Nanotech. 3 (2008) 626.

[40] A. Kis, G. Csányi, J-P. Salvetat, T-N. Lee, E. Couteau, A.J. Kulik, et al., Nat. Mat. 3 (2004) 153.

[41] Z.H. Xia, P.R. Guduru, W.A. Curtin, PRL 98 (2007) 245501.

[42] D.W. Brenner, O.A. Shenderova, J.A Harrison, S.J Stuart, B. Ni, S.B. Sinnott, J. Phys.: Condens. Matter. 14 (2002) 783-802.

[43] E.M. Byrne, M.A. McCarthy, Z. Xia, W.A. Curtin, Phys. Rev. Lett. 103 (2009) 045502.

[44] A.K. Kothari, S. Hu, Z. Xia, E. Konca, B.W Sheldon, Acta Mater. 60 (2012) 3333.

[45] A.K. Kothari, K. Jian, J. Rankin, B.W. Sheldon, J. Am. Ceram. Soc. 91 (2008) 2743.

[46] L. Pastewka, P. Pou, R. Pérez, P. Gumbsch, M. Moseler. Phys Rev B 78 (2008) 161402(4).

[47] L. Xu, N. Wei, Y. Zheng, Z. Fan, H. Wang, J. Zheng, J. Mater. Chem. 22 (2012) 1435.

CHAPTER 7

THERMAL TRANSPORT OF JUNCTIONS IN 3D CARBON NANOTUBE-GRAPHENE NANOSTRUCTURE

7.1 Introduction

3D CNT-graphene nanostructures have attracted abundant interest due to their unique architecture designs and excellent properties. Experimental strategies have been developed to fabricate this new structure—vertical CNT growth on parallel graphene plane [1-3], providing possibility of applications in various fields [4-8]. Mechanical, electrical, and thermal properties have been widely studied on the new 3D structure with aid of experimental apparatuses and modeling approaches [9-12]. Thermal transport ability of components could significantly influence their performance and service period on supercapacitors, integrated circuits, fuel cells, and so forth. In 3D nano structures, junctions are the transitional area connecting CNTs and graphene layers, which effect phonon transfers of the whole structure. In chapter 5, junctions with fillet angles of 120°, 135°, 150°, and 180° were grown with MD simulations and their thermal transport will be studied with classical molecular dynamic simulations herein.

The growth mechanism of junctions in 3D CNT–graphene nano structure has been revealed by QM/MD (quantum mechanical molecular dynamics) simulations [13], and growth of single layer junctions on Cu template has been simulated with classical MD simulations [14], providing theoretical support for fabrications of this new materials in experiments. Almost all the thermal studies paid attention on large scales of whole 3D structures without metal catalysts. Herein, we will focus on thermal properties of junctions with metal catalysts, since most 3D nanostructures were fabricated with aid of metal particle catalysts remaining in the junction

structures even after subsequent treatments. We have studied mechanical properties of junctions with metal catalysts [14], and in this chapter we continue to use the same modes.

7.2 Simulation Methodology

Molecular dynamic (MD) methods were utilized to calculate thermal conductivities of junctions. The MD algorithm was used here as implanted in the LAMMPS code to calculate the thermal conductivities of junctions. The forces of the C atoms were computed using the second-generation reactive empirical bond-order potential (AIREBO) [15-18]. With a rescaling thermostat to control the temperature (300K), the equations of motions were integrated with a time step of 0.25 fs.

Thermal conductivities were calculated with the Variant of Muller-Plathe reverse perturbation method. Some kinetic energy was added to one atoms group while the same quality of kinetic energy was subtracted from another group, and then a temperature gradient generates in the system. According to Fourier expressions, the heat flowing can be expressed as $J = -\kappa \nabla T$. In the z direction, $J = \frac{\Delta Q}{A \Delta t}$ is the heat flowing per second through a surface with area A, and the temperature gradient is ∇T=dT/dZ, so that the thermal conductivity can be calculated as $\kappa = \frac{\Delta Q}{A \Delta t} \frac{\Delta Z}{\Delta T}$. Thermal conductivities of different junctions were calculated including grown filleted double-layer junctions (**Fig. 7.1** (a)), pure C-C bonded junctions (**Fig. 7.1** (b)), junctions with a Fe particle between CNT and graphene (**Fig. 7.1** (c)), and junctions with a Fe particle embedded in it (**Fig. 7.1** (d)).

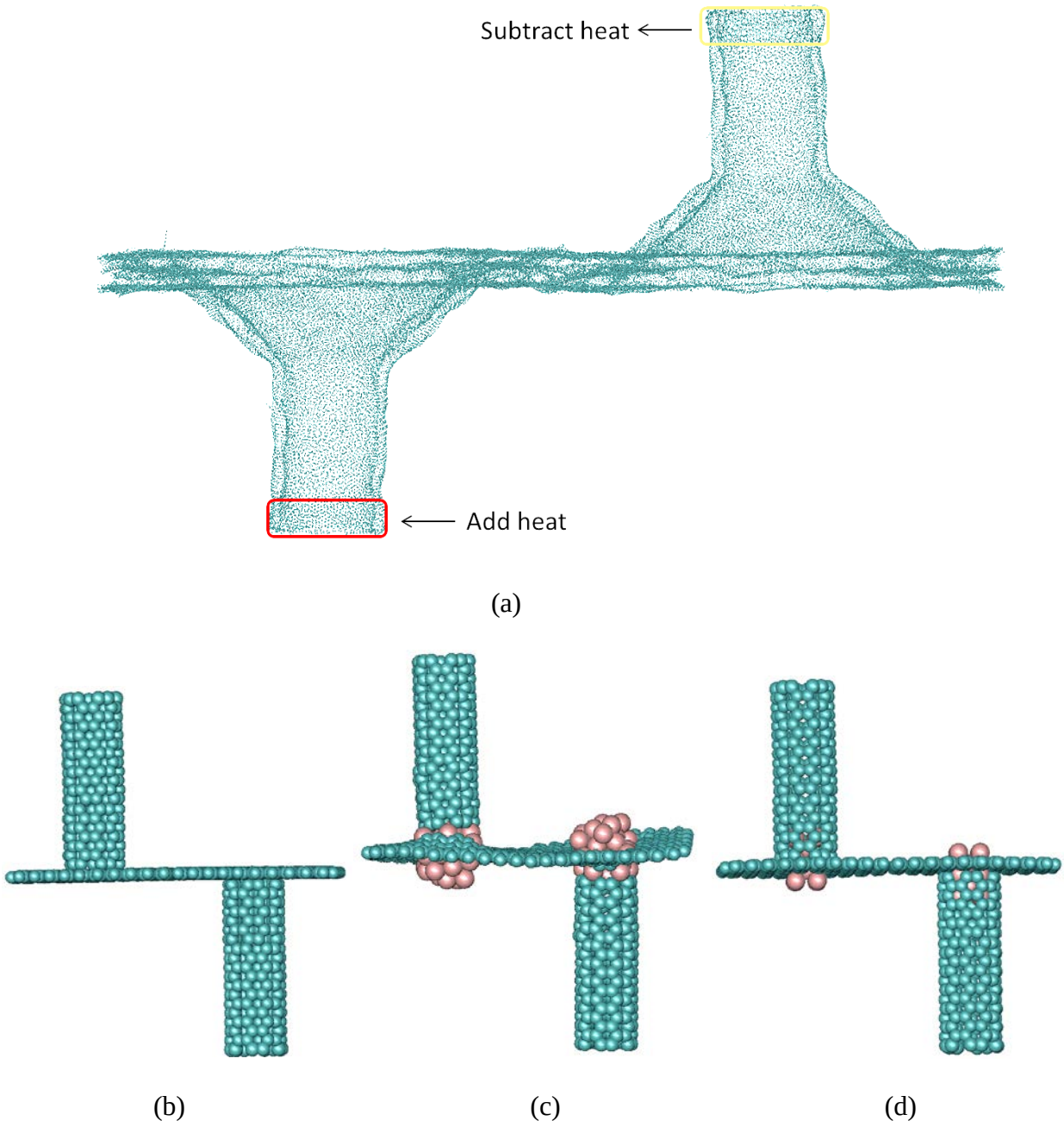

Fig. 7.1 The thermal conductivity calculation models: (a) A grown 135° filledted junction, (b) an as-grown pure C-C bonded junction, (c) an as-grown junction with a Fe particle between CNT and graphene, and (d) an as-grown junction with a Fe particle embedded in it.

7.3 Results and Discussion

Single walled CNT was reported to have thermal conductivity as high as 6600 W/mK at room temperature [19], and graphene has exceptionally high thermal conductivity of 3080 –

5150 W/mK [20]. Junctions of 3D CNT-graphene are expected to possess excellent thermal conductivities inheriting from CNTs and graphene.

7.3.1 Thermal Conductivities of Grown Filleted Junctions

Heat addition and subtraction with rate of 1.0 eV/ps was exerted on two regions of junctions (**Fig. 7.1** (a)). The area with heat addition is at an elevated temperature and is called the hot region, and the area with heat subtraction is at a lowered temperature and is called the cold region, so that kinetic energy will transport from the hot region to the cold region. The thermal conductivity can measure the ability of junctions to dissipate heat.

Thermal conductivities of 90° filleted junctions, 120° filleted junctions, 135° filleted junctions, 150° filleted junctions, and 180° filleted junctions were obtained as shown in **Fig. 7. 2**. The junction with 135° fillet has the highest thermal conductivity compared with other junctions. As we discussed in Chapter 6, the junction with 135° fillet also has the largest fracture strength among the computational models. We also calculated the potential energy with the MD method, which shows that the 135° filleted junction has the minimum potential energy. All of these are coincided with the experimental results that the 135° filleted junctions grow naturally. Compared to pristine CNTs and graphene, the kinetic energy transfer in junctions has to overcome the phonon obstructions of the corner where the atoms arrangements are alternative. Change of fillet angles can lead to variation of local atom arrangements and different obstructions for heat transfers. Our results show that the 135° filleted junction has the lowest heat transfer obstruction and highest thermal conductivity. For the 90° filleted junction and 180° filleted junction, the CNT and graphene connect to each other with a right angle, atom arrangements change dramatically, and obstructions on heat transfer is the most significant. For other filleted

junctions, the grade of phonon obstructions is among the 135° filleted junction and 90° (180°) filleted junction. As shown in **Fig. 7.3**, the red highlighted areas are the main obstruction regions. We propose that there is a critical angle at which the junction can compromise the heat transfer obstructions of these two regions and best thermal conductivity is obtained.

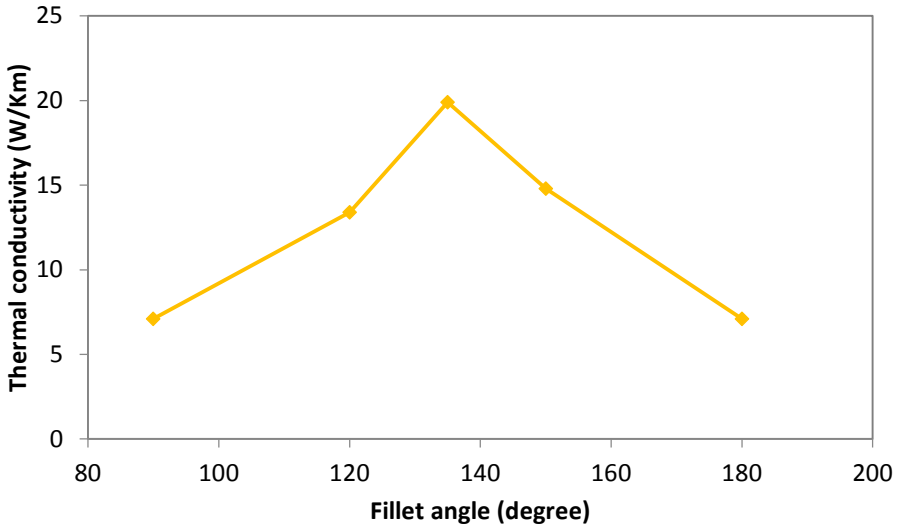

Fig. 7.2 Thermal conductivities of 90°, 120°, 135°, 150°, and 180° filleted junctions.

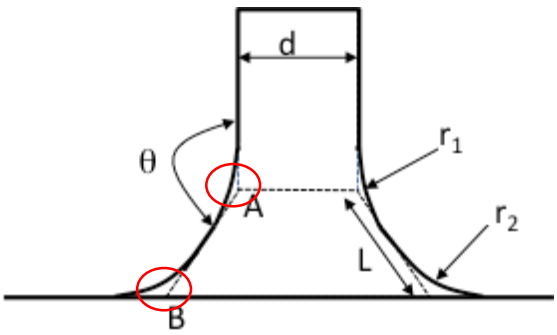

Fig. 7.3 Schematic of a fillet junction. Red highlighted areas are main heat transfer obstruction regions.

7.3.2 Thermal Conductivities of Junctions with Fe Nanoparticle Catalysts

In chapter 6, we have investigated mechanical properties of as-grown junctions with Fe catalysts via the QM/MD method. Herein, thermal conductivities were studied upon pure C-C bonded junctions, junctions with a Fe particle between CNT and graphene, and junctions with a Fe particle embedded in them. The thermal conductivity of iron is about 80 W/Km at room temperature, which is much lower than that of CNT and graphene. Thermal conductivities of 3D junctions significantly decrease due to the existence of Fe particles as shown in **Fig. 7.4,** regardless of positions of metal particles. The extremely high thermal conductivities of CNT and graphene are caused by high speed phonon transfers between carbon atoms through the pure C-C sp^2 covalent bonds. When metal catalysts are involved, some C-C bonds are replaced by metal-C bonds, and then phonon transfers also occur between carbon- iron atoms and iron – iron atoms, which are much slower than that between carbon-carbon atoms. In other words, Fe atoms slow down the heat transfers in the carbon junctions. Thus, metal catalysts left in the junctions will significantly affect thermal properties of 3D nano-architectures. It is necessary to control the quantity of catalysts during the fabrication or remove them by subsequent treatments.

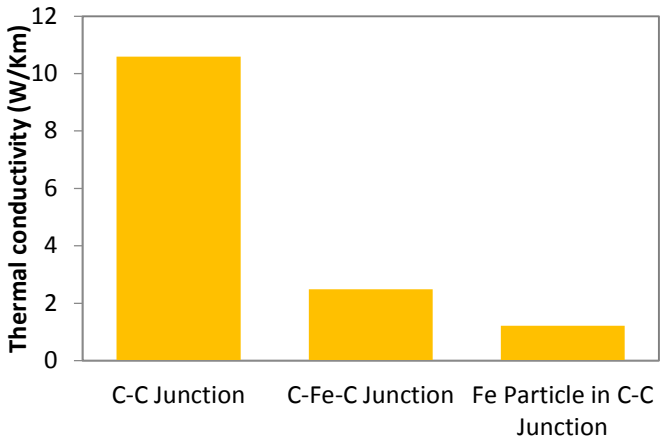

Fig. 7.4 Thermal conductivities of the as-grown pure C-C bonded junction, as-grown junction with Fe particle between CNT and graphene, and as-grown junction with Fe particle embedded in it.

7.4 Conclusions

Thermal conductivities of filleted junctions with fillet angles of 90°, 120°, 135°, 150°, and 180° were calculated with molecular dynamic simulations. Junctions with different angles show different abilities of heat transfers. The junction with 135° fillet has the largest thermal conductivity compared with other junctions. The fillet angle could have effect on the thermal dissipation of junctions. Thermal conductivities of junctions with iron nanoparticles were also calculated with MD methods. Compared to pure C-C junctions, junctions with Fe particles embedded have much lower thermal conductivities, proving that metal catalysts left in junction could considerably affect the junction performance.

7.5 References

[1] J. Lin, C. Zhang, Z. Yan, Y. Zhu, Z. Peng, R. H. Hauge, D. Natelson, J.M. Tour, Nano Lett. 13 (2013) 72.

[2] M. Zhao, X. Liu, Q. Zhang, G. Tian, J. Huang, W. Zhu, F. Wei, ACS Nano 6 (2012) 10759.

[3] J. Wen, Y. Li, W. Yang, Vacuum 101 (2014) 271.

[4] G.K. Dimitrakakis, E. Tylianakis, G.E. Froudakis, Nano Lett. 3 (2008) 3166.

[5] V. Varshney, S.S. Patnaik, A.K. Roy, G. Froudakis, B.L. Farmer, ACS Nano 4 (2010) 1153.

[6] L. Xu, N. Wei, Y. Zheng, Z. Fan, H. Wang, J. Zheng, J. Mater. Chem. 22 (2012) 1435.

[7] F. Du, D. Yu, L. Dai, S. Ganguli, V. Varshney, A.K. Roy, Chem. Mater. 23 (2011) 4810.

[8] Y. Kim, K. Kumar, F.T. Fisher, E. Yang, Nanotechnology 23 (2012) 015301.

[9] F.D. Novaes, R. Rurali, P. Ordejon, ACS NANO 4 (2010) 7596.

[10] S. Sihn, V. Varshney, A.K. Roy, B.L. Farmer, CARBON 50 (2012) 603.

[11] J. Park, V. Prakash, J. Mater. Res. 28 (2013) 940-951.

[12] D. Yu, L. Dai, J. Phys. Chem. Lett. 1 (2010) 467.

[13] J. Niu, M. Li, W. Choi, L. Dai, Z. Xia, CARBON 67 (2014) 627.

[14] J. Niu, M. Li, Z. Xia, RSC Adv. 4 (2014) 33848.

[15] D.W. Brenner, O.A. Shenderova, J.A. Harrison, S.J. Stuart, B. Ni, S.B. Sinnott, J. Phys.: Condens. Matter. 14 (2002) 783.

[16] D.W. Brenner, Phys. Rev. B,42 (1990) 9459.

[17] J.A. Harrison, C.T. White, R.J. Colton, D.W. Brenner, Phys. Rev. B 46 (1992) 9700.

[18] D.W. Brenner, D.H. Robertson, ML. Elert, C.T. White, Phys. Rev. Lett. 70 (1993) 2174.

[19] S. Berber, Y.K. Kwon, D. Tomanek, Phys. Rev. Lett. 84 (2000) 4613.

[20] S. Ghosh, I. Calizo, D. Teweldebrhan, E.P. Pokatilov, D.L. Nika, A.A. Balandin, W. Bao, F. Miao, C.N. Lau, Appl. Phys. Lett. 92 (2008) 151911.

CHAPTER 8

CONCLUSIONS AND FUTURE WORK

8.1 Conclusions

The junction growth of 3D CNT graphene nano architectures have been simulated with quantum mechanical molecular dynamics and classical molecular dynamics methods. Growth mechanisms and mechanical and thermal properties are revealed based on newly growth different junctions.

Vertical CNTs growth on a graphene substrate with iron nanoparticles as catalysts was simulated *via* the QM/MD method. The CNT growth was characterized by several stages: in the early stage, short polyyne chains appeared and brunched on the surface of the catalyst, followed by the polygons (pentagons, hexagons and heptagons) growth, and CNT cage formation and growth in a "base-growth" mode. The junctions between CNT and graphene are formed with a mixture of C-C and Fe-C bonds. The catalyst has a strong tendency to move with the growing CNT cage, which facilitated the C-C bonded junction formation. Seamlessly C-C bonded junctions could be produced by: (i) lifting up the catalysts during CNT growth by transforming the CNT growth from "base-growth mode" to "tip-growth mode" with force, and (ii) etching and annealing after the CNT growth to remove iron nanoparticles, leading to the release of carbon dangling bonds at graphene edge from strong Fe-C bonds to form C-C bonds even at relatively low temperature.

Growth processes of 3D CNT-graphene junctions on Cu templates were simulated via classical MD simulations. There are two growing mechanisms depending on the size of the template holes: i) CNT growth over the small hole, and ii) CNT growth inside the large hole. Line and point defects were found in the grown CNTs, graphene layers, and junctions. Pentagons

and heptagons play an important role in the junction growth especially at the transition region of CNT and graphene. The seamless C-C junction growth mechanisms found in this study provide a theoretic foundation for growth of 3D nanostructures without any catalysts.

Growth processes of 3D CNT-graphene junctions on alumina templates were simulated via classical MD simulations. Multi-layer CNT-graphene junctions with fillets were formed on the alumina template. A simple analytical model is developed to explain why the fillet takes the particular angle (135°). The model predicts that there is a critical fillet angle, at which the system energy reaches its minimum value. The predictions are consistent with the MD simulations and experimental observations. Our simulations show that it possible to synthesize high-quality 3D CNT-graphene nanostructures using template methods without catalysts.

Tensile tests of different types of junctions in 3D carbon nanotube – graphene nanostructures were simulated via quantum mechanical molecular dynamic methods and classical molecular dynamic methods. Covalently C-C bonded junctions possess the highest fracture strength and fracture energy. The metal nanoparticles embedded in the junctions between the CNT and graphene significantly reduce the fracture strength and energy. Even when the metal particles are embedded inside the junction, C-C bonded junctions are weakened by particles. Filleted junctions with different fillet angles were tested. The 135° filled junction has the strongest fracture strength compared with 90°, 120°, 150°, and 180° junctions, proving the preference of 135° junctions in experiments.

Thermal conductivities of filleted junctions with fillet angles of 90°, 120°, 135°, 150°, and 180° were calculated with molecular dynamic simulations. Junctions with different angles show different abilities of heat transfers. The junction with 135° fillet angle has the highest thermal conductivity compared with other filleted junctions. The fillet angle could have effect on

the junction thermal dissipation. Thermal conductivities of junctions with iron nanoparticles were also calculated with MD methods. Compared to pure C-C junctions, junctions with Fe particles have much lower thermal conductivity, proving that metal catalysts left in junction could considerably affect the junction performance.

8.2 Future Work

The simulations on 3D CNT-graphene nano-architectures are designed to provide fundamental theories and guidelines for the experimental work. It is necessary to develop a unique combination of theoretical models including quantum mechanics, molecular dynamics, and continuum numerical methods to predict the mechanical and thermal properties of 3D nanostructures and translate them into enhanced performance (**Fig. 8.1**).

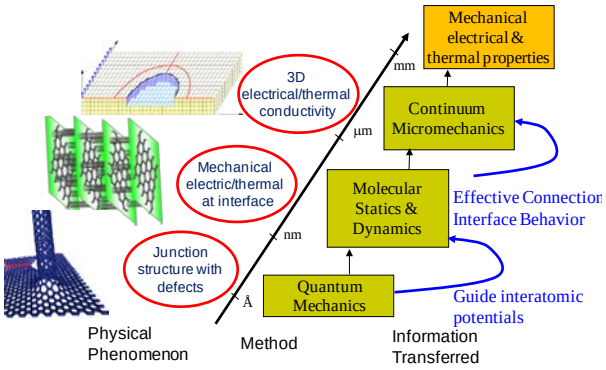

Fig. 8.1 Multi-scale modeling strategy for 3D nanostructures.

We have studied growth mechanisms and mechanical and thermal properties of 3D junction with quantum mechanics and molecular dynamics. Next, continuum numerical method will be employed to study mechanical and thermal properties in micro scale. Finite element analysis (FEA) will be the computation method. The FEA method is extremely powerful when solving sophisticated systems such as irregular shapes and combined configurations. It can deal

with a wide range of materials including metals, polymers, ceramics, composites, biomaterials, and many more. Thus, we can build 3D junction models with exact geometric shapes of that in the experiments or in devices and the computational results can directly provide structure design parameters for the experiments and applications.

APPENDIX

LIST OF PUBLICATIONS

[1] J. Niu, M. Li, W. Choi, L. Dai, Z. Xia, CARBON 67 (2014) 627.

[2] J. Niu, M. Li, Z. Xia, RSC Adv.4 (2014) 33848.

[3] J. Niu, L. Li, Q. Xu, Z. Xia, CMC 38 (2013) 31.

[4] L. Zhang, J. Niu, M. Li, Z. Xia, J. Phys. Chem. C 118 (2014) 3545.

[5] L. Zhang, J. Niu, L. Dai, Z. Xia, Langmuir 28 (2012) 7542.

[6] L. Li, J. Niu, Y. Yang, Z. Xia, Computational Materials Science 83 (2014) 255.

[7] L. Li, J. Niu, Z. Xia, Y. Yang, J.Y. Liang, Scripta Materialia 65 (2011) 1014.

[8] F. Solá, J. Niu, Z. Xia, J. Phys. D: Appl. Phys. 46 (2013) 065309.

[9] Z. Xia, T. Sujidkul, J. Niu, C.E. Smith, G.N. Morscher, Composites: Part A 43 (2012) 1730.

[10] Q. Xu, M. Li, J. Niu, Z. Xia, Langmuir 29 (2013) 13743.

[11] Q. Xu, M. Li, L. Zhang, J. Niu, Z. Xia, Langmuir 30 (2014) 11103.

[12] M. Li, L. Zhang, Q. Xu, J. Niu, Z. Xia, Journal of Catalysis 314 (2014) 66.